Analysis and Mitigation of Key Losses in a Multi-Stage 25–100 K Cryocooler

by

Martin Alan Segado

S.B., Massachusetts Institute of Technology (2007)

Submitted to the Department of Mechanical Engineering
in partial fulfillment of the requirements for the degree of

Master of Science in Mechanical Engineering

at the

MASSACHUSETTS INSTITUTE OF TECHNOLOGY

February 2014

Author .....
Department of Mechanical Engineering
February 10, 2014

Certified by .....
John G. Brisson II
Professor of Mechanical Engineering
Thesis Supervisor

Accepted by .....
David E. Hardt
Ralph E. and Eloise F. Cross Professor of Mechanical Engineering
Chairman, Department Committee on Graduate Students

Analysis and Mitigation of Key Losses in a Multi-Stage 25–100 K Cryocooler

by

Martin Alan Segado

Submitted to the Department of Mechanical Engineering on February 10, 2014,
in partial fulfillment of the requirements for the degree of
Master of Science in Mechanical Engineering

Abstract

A need exists for small, robust, and efficient cryocoolers operating in the 25–100 K range; however, while technological advances have enabled the development of such machines, a greater understanding of the losses affecting their performance is needed to make informed design tradeoffs. This thesis takes steps to provide this understanding by examining several losses in the context of a multi-stage cryocooler being developed by MIT and Advanced Mechanical Technologies, Inc. Based on a modular Collins-type design, this cryocooler will use computer-controlled floating piston expanders to simultaneously provide 20 and 100 Watts of cooling at 25 and 100 K, respectively.

The contributions in this thesis can be divided into two broad categories. The first is concerned with the systems-level efficiency of the cryocooler, and addresses a significant inefficiency caused by an inherent cooler-to-load temperature mismatch. By using an alternative cryocooler configuration with multiple expanders in series, the overall efficiency may be increased by an estimated 24%. A simple memorizable heuristic was also found to estimate the magnitude of the mismatch loss in a given stage of the cryocooler: the fractional increase in operating power is approximately the base-10 logarithm of the pressure ratio divided by twice the number of series expanders, assuming a monatomic working fluid.

The second area of research focused on the design of the cryocooler's unique floating piston expanders. A variety of losses affect the performance of these expanders; these range from the obvious to the obscure (e.g., the enhanced "shuttle" heat transfer that arises from reciprocating piston motion) and often favor conflicting design choices. Eleven such losses are discussed along with both existing literature and a new analysis of fluid flow and heat transfer in the piston-cylinder gap. A numerical model incorporating six of these losses was used to gain considerable insight into the design tradeoffs involved in expander design and provide preliminary support for the multi-expander designs discussed earlier. The simulations also challenged a previous design guideline for the piston's stroke length and, unexpectedly, revealed that imperfect expansion and compression can yield a net increase in expander efficiency due to the importance of shuttle heat transfer.

Thesis Supervisor: John G. Brisson II
Title: Professor of Mechanical Engineering

Acknowledgments

This thesis has been a long time in the making, and it would not have been possible without the support, encouragement, and grace that so many have given me. My sincere thanks go out to my family, for loving me and looking out for me thoughout this time; to my advisor, for his patience and investment in my growth over these years; to all my amazing, loving friends; to Chuck Hannon at AMTI; to Doris Elsemiller and my labmates at the Cryolab (a particular shout-out to Wayne Staats for the many entertaining discussions and endeavors as well as for his proofreading help); to Prof. Hardt and Leslie Regan in the mechanical engineering department; to Wayne Johnson for his kindness throughout the years; to the many faculty and staff who have supported me personally as well as financially through teaching assistanceships; to NASA, for funding the early part of this research; and most of all, to the God and father of my Lord Jesus, for loving me and taking care of me so much more than I deserve or understand.

To everyone, thank you.

—Martin

Contents

List of Figures

List of Tables

"Entropy is like Tribbles; you only ever end up with more of them."

— J. G. Brisson

Chapter 1

Introduction

1.1 Motivation

Over the past decade, various authors have pointed to the need for long-term liquid cryogen storage in space for Mars missions, long-term geosynchronous missions, cryogenic propellant depots, and orbital transfer vehicles [HPSK02, PK03, HMF06]. Although there is little or no potential for heat to leak into cryogen tanks when a spacecraft is far from planets and other warm bodies, the temperature felt by a spacecraft in the low Earth orbit common to many of these applications is around 250 K [PK03]. Even if highly effective multi-layered insulation is used to provide insulation, some heat inevitably leaks into the tanks, and as the cryogen warms the pressure in the tanks rises.

While a pressure rise may be managed by venting cryogens to space, actively subcooling the cryogens holds more promise for long-term applications; this is known as zero boil off (ZBO) cryogen storage. MIT and Advanced Mechanical Technologies, Inc. (AMTI) are developing a high-efficiency cryocooler well suited to ZBO storage of liquid cryogens in space as well as superconducting MRI/NMR magnet cooling, infrared focal plane array cooling, and other applications requiring refrigeration at temperatures below ~30 K [HKG$^+$07]. Based on a modified version of the Collins cryostat, the cryocooler aims to provide simultaneous refrigeration to multiple remote loads by circulating working fluid through external flow loops.

The modified Collins cryocooler (MCC) is intended to be thermodynamically efficient, with nominally-isentropic piston expanders taking the place of inherently dissipative expansion elements such as Joule-Thomson valves. Nevertheless, there remains a significant inherent inefficiency in the cycle: when the MCC is used to cool isothermal loads such as fuel tanks, the inherent temperature mismatch between loads and the circulating working fluid (which warms as it provides cooling) results in an estimated increase of ~50% in the cooler's power consumption. Additionally, the design tradeoffs in the expanders critical to the MCC are not well understood; the various parasitic losses in expanders favor substantially different designs when

examined individually, and a need therefore exists to consider them in aggregate in order to make better-informed design decisions.

1.2 Contributions

This thesis examines several key losses and design tradeoffs in the modified Collins cryocooler. Chapter 2 explores the inherent loss caused by the temperature mismatch between the cryocooler and isothermal loads, presents simple heuristic expressions to estimate the magnitude of the loss, and details an improved cryocooler configuration (complete with numerical simulations) that mitigates the loss by using multiple expanders per stage. Chapter 3 investigates the various losses affecting the design and performance of piston expanders, presents models to explore their effects on expander efficiency (including a new analysis of the important losses in the clearance space between the piston and cylinder), and discusses the various tradeoffs involved. Before engaging these areas, however, the remainder of this chapter will provide some context and technical background helpful to understanding the rest of the thesis.

1.3 Background: The Modified Collins Cryocooler

While some of the conclusions in this work are applicable to a variety of cryogenic equipment, they are presented in the context of a modified Collins cryocooler (specifically, one suitable for a ZBO fuel storage application requiring 100 W of cooling at 100 K and 20 W of cooling at 25 K[1]). This section will therefore introduce the key features and operation of the MCC, beginning with some discussion of its predecessor, the Collins cryostat.

1.3.1 History & Operation

The modified Collins cryocooler is largely based on the Collins helium cryostat, a seminal device designed in 1946 that improved low-temperature research by making liquid helium commercially available [Smi02]. Figure 1-1 shows a simplified schematic of the original Collins cryostat alongside a conceptual T-S diagram of the cycle it executes; a more thorough description of the cryostat is available in the literature [Col47]. During steady-state operation, 1.0–1.5 MPa helium from a compressor (not shown) enters a counterflow recuperative heat exchanger or *recuperator*, where it is cooled isobarically by heat transfer to the low-pressure stream. At two points along the recuperator, some of the high-pressure helium is extracted, expanded isentropically to 0.1 MPa, and re-inserted into the return stream at a lower temperature. The original Collins cryostat used flexible-rod piston expanders for these intermediate stages.

[1] These values are based on the cryogenic propellant storage requirements outlined in NASA's 2007 Small Business Technology Transfer solicitations [NASA07].

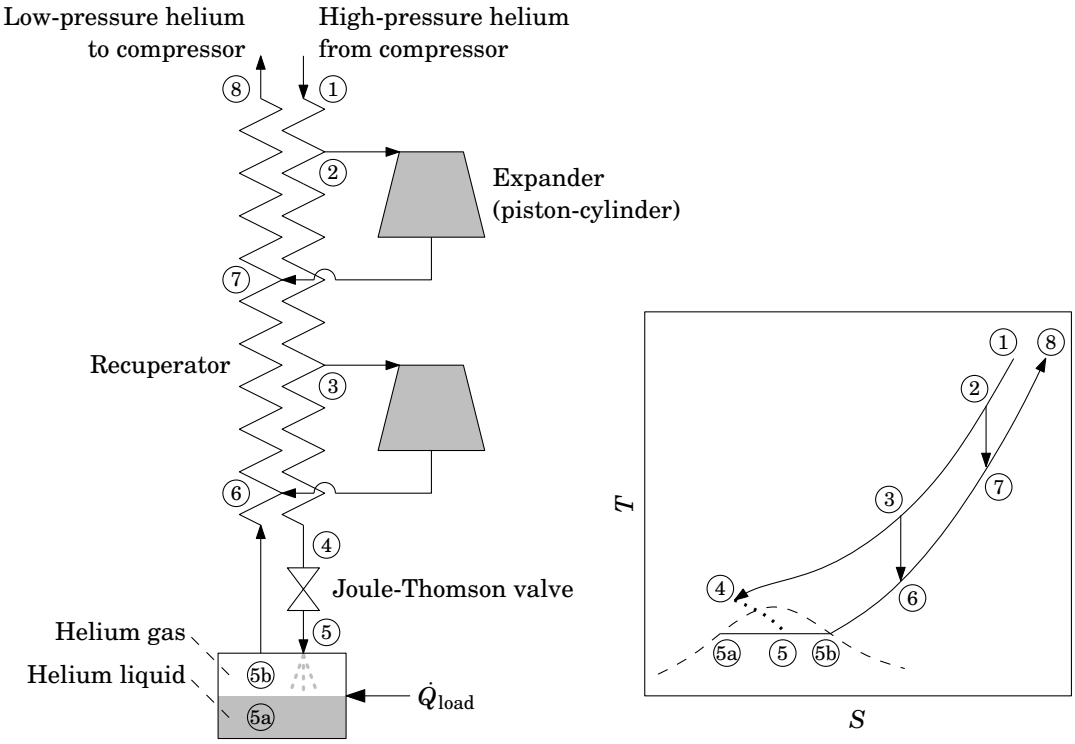

Figure 1-1: A simplified schematic and T-S diagram of the early Collins cryostat. High-pressure helium is cooled in a recuperator and expanded isenthalpically in a Joule-Thomson valve to cool and partially liquefy it. Two isentropic expanders are used to cause flow imbalances along the recuperator; this has the effect of decreasing the stream-to-stream temperature difference in the low-temperature part of the recuperator, which in turn reduces the total entropy generation rate [Col47, Min84].

The remaining high-pressure helium exits the recuperator at a low temperature and expands isenthalpically through a Joule-Thomson valve where it cools further and partially liquefies. The liquid helium provides cooling to the load at the saturation temperature determined by the low pressure in the cycle; any unliquefied helium (and the helium evaporating from the liquid due to heat transfer from the load and environment) returns through the recuperator where it precools the high-pressure flow before returning to the compressor.

The need for flow imbalance

The Collins cryostat owes much of its high efficiency to the deliberate mass flow imbalances between the recuperator streams. The need for these flow imbalances arises from both heat leaks into the recuperator and variations in the specific heat of helium at low temperatures.

Heat leaks typically take the form of radiation to the recuperator's exterior and axial conduction from the warm end. A greater flow rate in the low-pressure stream allows these heat transfers to be captured closer to their points of entry instead

of being carried to the cold end where they are more harmful to the cryocooler's performance.

Specific heat variations result from real gas effects and are most prominent at low temperatures (Figure 1-2). Without the mass flow rate imbalance introduced by the piston expanders, the heat capacity flow rates $C \equiv \dot{m} c_P$ of the recuperator streams would not be balanced and the stream temperatures would diverge near the recuperator's cold end (Figure 1-3a). The helium would then enter the Joule-Thomson valve at a higher temperature, yielding less liquid after expansion and thus reducing the cryostat's efficiency.

Even without heat leaks or real gas effects, however, a recuperator with balanced mass flow rates is not optimal. This problem was studied in detail by Minta, who used variational calculus to show that the total entropy generation rate is minimized for a fixed total heat transfer area when $\Delta T/T = \text{constant}$;[2] remarkably, this conclusion holds even when c_P is a function of temperature and pressure [Min84]. Such a temperature distribution (Figure 1-3b) devotes a higher fraction of the recuperator's heat transfer area to low-temperature heat exchange, where the resulting small ΔT is most beneficial in reducing entropy generation.

[2]Minta considered a continuum model of a recuperator in which the two streams may exchange mass continuously along their length via an infinite number of reversible expansion or compression processes. This recuperator model further assumed a constant heat transfer coefficient U, negligible pressure drops, fixed stream pressures, and no axial conduction or radiation heat transfers.

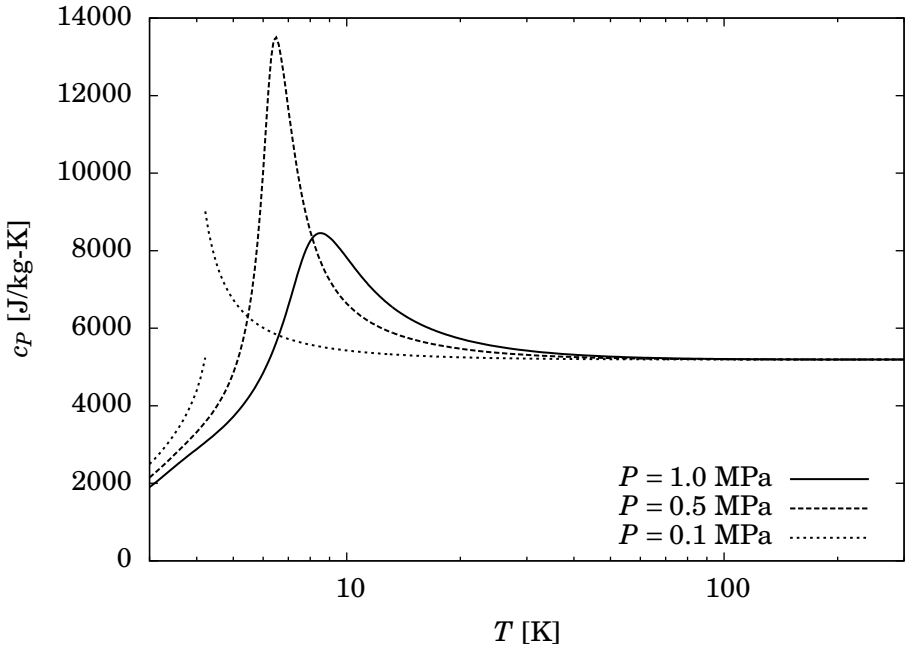

Figure 1-2: The specific heat at constant pressure of helium (c_P) as a function of temperature and pressure. At low temperatures, considerable variation exists over the typical pressures in a Collins cryostat or modified Collins cryocooler. (The discontinuity at 4.2 K and 0.1 MPa is due to a liquid/vapor phase transition.)

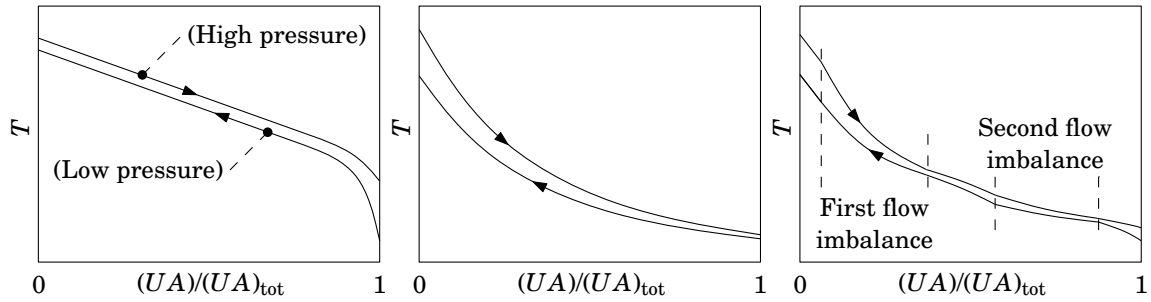

(a) Balanced mass flow rates **(b)** Constant $\Delta T/T$ **(c)** Collins cryostat

Figure 1-3: Conceptual fluid temperature profiles for high- and low-pressure streams in a recuperator. (a) Balanced mass flow rates can give a diverging temperature difference between streams due to the variable specific heat of helium. (b) Using an infinite number of expanders to give a constant $\Delta T/T$ minimizes entropy generation for a given heat transfer coefficient and area. (c) The Collins cryostat approximates a constant $\Delta T/T$ by using only two piston expanders to create flow imbalances.

A constant $\Delta T/T$ can be achieved in theory by using an infinite number of reversible expanders to transfer mass between the recuperator streams; as this is somewhat impractical, a finite number of expanders may be used to approximate this as in the Collins configuration, yielding the temperature distribution in Figure 1-3c.

An alternative to the Collins approach

While the Collins configuration successfully approximates a constant $\Delta T/T$, a similar effect can be achieved by the configuration shown in Figure 1-4, but with a more modular design; this is now known as a modified Collins cryocooler. Instead of using a single shared recuperator, each expander is surrounded by its own recuperator to form a discrete and compact stage, with "precooling" flows linking the stages to effect the required flow imbalances. These stages can then be assembled into two-stage (~30 K), three-stage (~10 K), and four-stage (~4 K) cryocoolers depending on the desired application. Additionally, cooling may be provided at multiple temperatures simultaneously [HGT$^+$03, HKG$^+$07]. No Joule-Thomson valves are used.

Operation of the modified Collins cryocooler is similar to that of the Collins cryostat. High-pressure helium is cooled in each stage's recuperator and expanded in a piston expander. In all but the coldest stage the flow is then split; some of the fluid may be used to provide cooling to a load before returning through the recuperator, while the remainder provides precooling to effect a flow imbalance in the next stage's recuperator.

1.3.2 Distinguishing Characteristics & Shortcomings

In addition to the deliberate flow imbalance introduced above, the modified Collins cryocooler borrows many other features from the original Collins cryostat (albeit

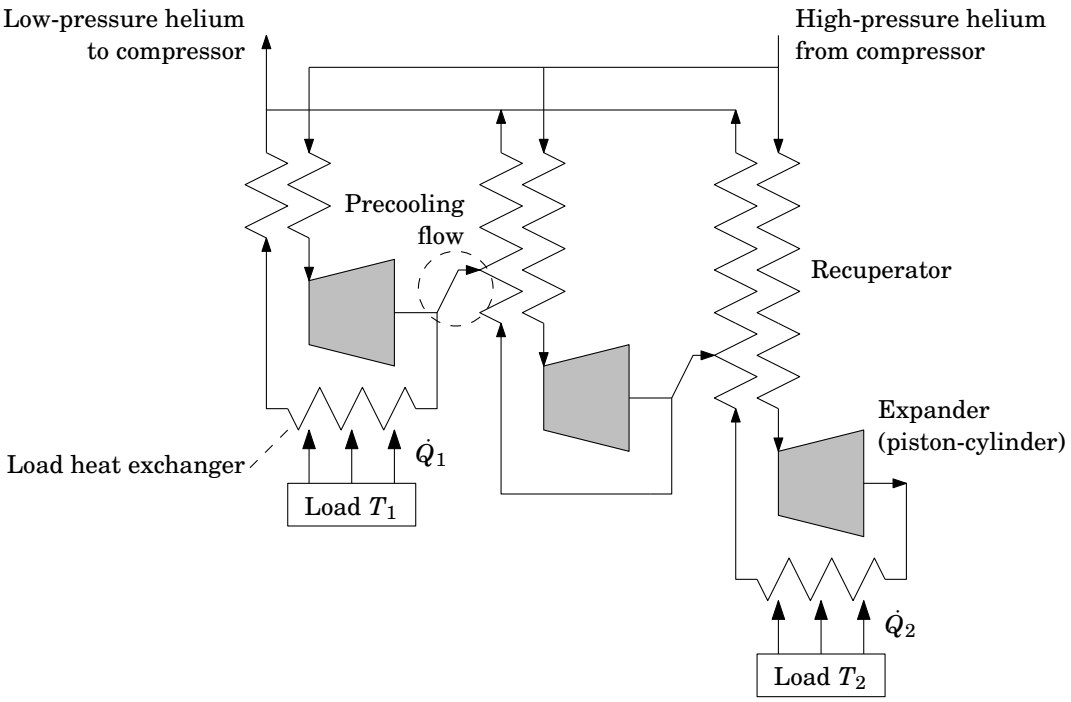

Figure 1-4: One possible configuration of a two-load modified Collins cryocooler. The design shares many features with the Collins cryostat but focuses more on modularity; discrete stages are therefore used, with only precooling flows linking them to create the desired flow imbalances.

with some modifications). Several of these are described below, along with other key characteristics of the MCC and some of their benefits and detriments.

Precooling flows

While the fundamental idea of using flow imbalances was borrowed from the Collins cryostat, the flow imbalances in an MCC create only one "pinch point" in each recuperator's temperature profile instead of several. This makes little difference when the specific heat capacities of the recuperator streams are relatively well-matched (as is the case for the 25–100 K cryocoolers in this thesis) though additional pinch points and some clever routing of precooling flows may prove necessary for lower-temperature applications where the heat capacity of helium varies more.

The precooling approach in an MCC is overall beneficial to the cryocooler's efficiency, but does have the characteristic of causing a detrimental flow imbalance in the first-stage recuperator[3]: since some of the first-stage mass flow is devoted to precooling, the high-pressure stream has a *higher* mass flow rate than the low-pressure stream, causing the stream temperatures to diverge at low temperatures (in contrast,

[3]Of course, it is always possible to use an additional expander fed directly from the compressor to precool the first stage recuperator if it becomes important to eliminate this loss.

the original Collins design shown in Figure 1-1 has at worst equal mass flow rates when operating as a refrigerator).

High pressure ratio

Another characteristic of both the original Collins cryostat and the modified Collins cryocooler is a high pressure ratio. Neither reversible nor Joule-Thomson expansion can occur without a pressure difference between the entering and exiting fluid, and the larger the ratio between the pressures, the greater the amount of cooling for a given mass flow rate. A high pressure ratio therefore leads to lower mass flow rates, and so smaller recuperators may be used [HGT$^+$03]. Minta similarly suggests that the pressure ratio should be made as high as possible for a fixed recuperator area and heat transfer coefficient, though his analysis was for cryocoolers with a different cold-end configuration.

The effect of a high pressure ratio can also be understood from an entropy perspective: the higher the pressure ratio, the greater the difference in specific entropy between the recuperator streams at any location, and consequently the greater the net entropy transport from the cold end to the warm end for a given mass flow rate.

Compact helical recuperators

The recuperator design used in the Collins cryostat and MCC is well suited to a high pressure ratio. By using a larger flow area and shorter flow distance for the low-pressure, low-density fluid than for the high-pressure, high-density fluid, a similar fractional pressure drop $\Delta P/P$ can be achieved in both streams of the recuperator.

A partial cross section of an MCC recuperator is shown in Figure 1-5. Much like

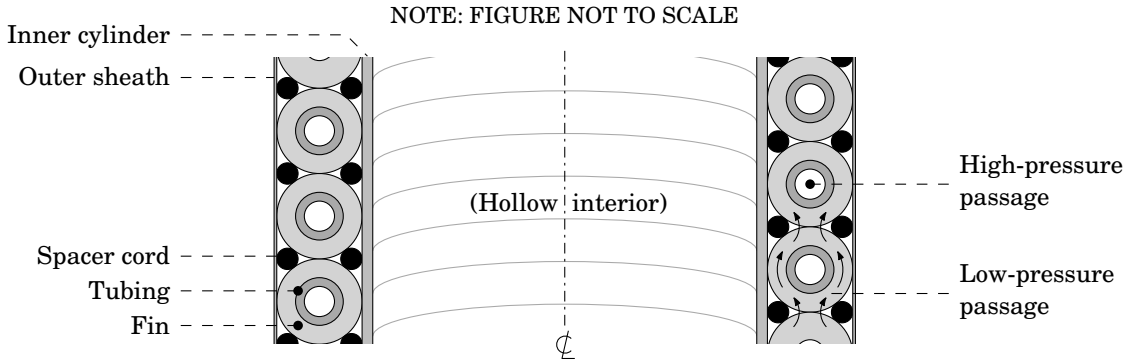

Figure 1-5: Partial cross section of a coiled finned-tube heat exchanger for use as a recuperator. The inner cylinder provides space for cryocooler components, and the cross-counterflow design yields a low-pressure passage with a larger flow area and shorter length than the high-pressure passage, well suited to the large density differences arising from a high pressure ratio. Curved arrows illustrate low-pressure fluid flow past the fins.

a Hampson heat exchanger, the recuperator uses finned metal tubing as its high-pressure passage, which is coiled into a helix around a hollow cylinder and surrounded by a tight-fitting sheath. The hollow cylinder provides space for each stage's expander while the annular space between the cylinder and sheath forms the low-pressure passage, making for a space-efficient design. Spacer cords are used between the finned tubes to keep the fins from nesting; these also fill some of the space between the coils and force more of the flow into thermal contact with the fins.

The difference in flow passage length is made possible by the cross-counterflow configuration of the recuperator. Low-pressure fluid flows essentially perpendicular to the high-pressure passage, traversing a much smaller distance than would be possible in pure counterflow (where the flow passages would be essentially the same length). Each coil of the recuperator therefore behaves like a crossflow heat exchanger, with the added benefit that crossflow usually allows for higher heat transfer coefficients than longitudinal flow [Mar92, p. 46]. When many coils are used, the temperature difference across each coil becomes small and the recuperator's overall behavior approaches that of a counterflow heat exchanger.

Various heat transfer correlations exists to aid in the design of coiled finned-tube heat exchangers. Gupta et al. summarized many of these and compared them to experimental data for a heat exchanger configuration similar to that used by Collins [GKT09]. Gupta et al. also presented experimental data for the pressure drops in such heat exchangers, along with a new shell-side correlation for low Reynolds numbers [GKT10].

Floating piston expanders

The piston expanders used in the modified Collins design (shown schematically in Figure 1-6) differ from those in the Collins cryostat. No piston rod is used; instead, a long, close-fitting piston with no mechanical connections "floats" between warm and cold working volumes. The piston is driven by pressure differentials caused by opening and closing valves at both ends of the expander. As long as the piston does not accelerate quickly or experience significant frictional, gravitational, or contact forces, the pressure on either side of the piston remains essentially the same, and consequently there is little driving force for leakage past the piston. The feasibility of such floating piston expanders was experimentally demonstrated by Jones [Jon99], and Chaudhry later presented static and dynamic expander models as well as more experimental results for a laboratory prototype [Cha05].

Computer-controlled electromagnetic valves at the cold end enable the expander to intake and exhaust fluid, and do away with the need for valve rods extending from the warm end. The valve design was developed by Traum and also described by Hannon et al. [TSB$^+$04, HGK$^+$04]. When closed, a flat metal disk rests on several small Kel-F valve seats; multiple small ports are used to reduce the required lift of the valve. The disk is oriented on the higher-pressure side of the valve such that normal pressure differences across the valve work to keep it closed, and permanent magnets hold the

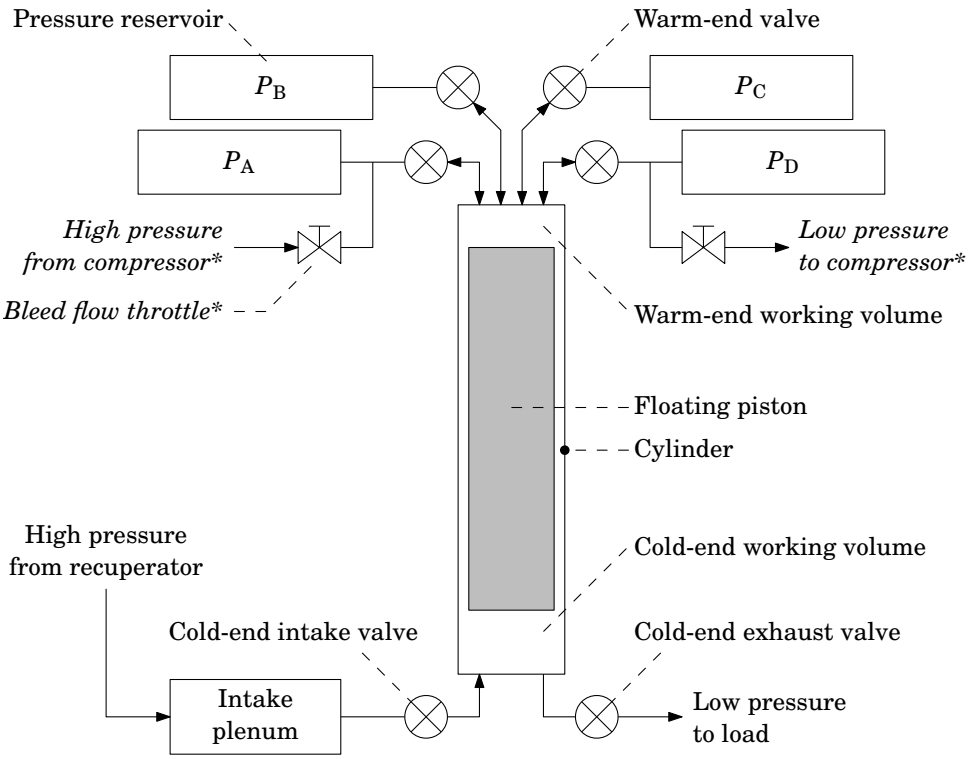

Figure 1-6: Schematic diagram of a floating piston expander. By actuating computer-controlled valves leading to pressure reservoirs at the warm end in concert with valves at the cold end, the motion of the piston can be controlled to provide expansion without mechanical linkages. *(*Bleed flow throttles are shown for completeness but may not prove necessary in all expander designs.)*

valve closed in the absence of pressure differences. To open the valve, a control circuit applies a large current pulse to a toroidal electromagnet immediately above the disk, pulling the disk off the valve seats. With the valve open there is much less force from the pressure difference and permanent magnets, and the disk is closer to the electromagnet; the control circuit therefore decreases the current to a much lower holding value. This "smart" control approach limits ohmic losses to a negligibly small fraction of the cryocooler's total heat load.

The warm end is equipped with conventional flow control valves, also computer-controlled. These valves are used to connect the warm volume to one of four reservoirs containing helium at a range of pressures (such that $P_{\text{high}} > P_A > P_B > P_C > P_D > P_{\text{low}}$). The reservoirs naturally assume stable pressures during expander operation, albeit not always desirable ones; while Chaudhry addressed this issue by connecting small bleed flows between the warm end and the compressor (see Figure 1-6), recent work by Hogan suggests that suitable pressures may be attained without such bleeds by using a control algorithm that deliberately forces mass through the clearance gap between the floating piston and the expander cylinder [Hog12].

Operation of the FPE proceeds as follows, beginning with all valves closed and the piston at the cold end of the expander:

1. **Blow-in:** The cold-end intake valve opens, causing high-pressure working fluid to rush into the expander until the pressure reaches a set fraction of P_{high}. The piston moves upwards somewhat during this process due to compression of gas in the warm-end working volume.

2. **Intake:** The valve to reservoir A opens; as fluid flows from the warm-end working volume into the reservoir, the piston moves toward the warm end and more high-pressure working fluid enters the cold end.

3. **Expansion:** The cold intake valve closes, but the valve to reservoir A remains open. As fluid flows into the reservoir, the piston continues to move toward the warm end and the pressure in the expander decreases. On reaching a set fraction of P_{A}, the valve to reservoir A closes and the valve to reservoir B opens, continuing the expansion. This is repeated for the remaining reservoirs, nominally ending with the piston at the warm end of the expander, the pressure at a set fraction of P_{D}, and all valves closed.

4. **Blow-out:** The cold-end exhaust valve opens, causing fluid to rush out of the expander until the pressure reaches a set fraction of P_{low}. This is also referred to as "blow-down" in some of the literature.

5. **Exhaust:** The valve to reservoir D reopens; as fluid flows into the warm-end working volume, the piston moves toward the cold end and more cold-end working fluid exits the FPE via the exhaust valve. This process continues until the piston reaches a set cutoff position, leaving a controlled volume of working fluid in the cold end.

6. **Recompression:** The cold exhaust valve closes, but the valve to reservoir D remains open. As fluid flows out of the reservoir, the piston continues to move toward the cold end, compressing the remaining cold-end working fluid. On reaching a set fraction of P_{D}, the valve to reservoir D closes and the valve to reservoir C opens, continuing the recompression. This is repeated for the remaining reservoirs, nominally ending with the piston at the cold end of the expander, the pressure at a set fraction of P_{A}, and all valves closed. The cycle then repeats.

The timing of these processes needs not be fixed; by adjusting the points at which the valves open and close, a smart control algorithm could in principle tailor the cycle to different operating conditions (e.g., favoring total power over efficiency during cool-down [Cha05] or even changing the processes altogether to safely shut down the expander for maintenance [Hog12]).

While the current warm-end configuration has the advantages of mechanical simplicity and adaptability, it also has a notable drawback: the net work extracted from the cold end is entirely dissipated by a combination of the warm-end reservoir valves, irreversible mixing, and other warm-end irreversibilities. In cryocoolers with load temperatures well below the temperature of the environment, though, this

dissipation is acceptable since the maximum work available from expansion is small compared to the compressor work (owing primarily to the Second Law).

DC flow & remote-load cooling

Floating piston expanders are intermittent-flow devices; however, the recuperators are designed to operate with a steady flow of working fluid. Consequently, an intake plenum (also known as a surge volume) must be used with each expander to even out the flow. At a more general level, the modified Collins cryocooler is based on a direct current (DC) flow paradigm, as is the original Collins cryostat: working fluid flows unidirectionally in a loopwise fashion through the device instead of oscillating back and forth as in Stirling, pulse-tube, or Gifford-McMahon cryocoolers.

A DC-flow design is naturally well suited to circulating cold working fluid to a load some distance away from the cryocooler (though Ceridon and Smith demonstrated that a Gifford-McMahon cryocooler can also be equipped with cold-end valves to provide remote cooling [CS01]). Such remote-cooling capability affords some flexibility in the placement of the cryocooler, and can be used to cool a stored cryogen by circulating working fluid through a heat exchanger immersed directly in the cryogen instead of requiring a heat pipe or other additional heat transfer element.

Remote-load cooling is not without its disadvantages, though. To provide cooling at constant pressure, a circulating single-phase working fluid must warm up as it receives a heat transfer from the load. This flow-wise temperature change makes it impossible for the fluid to match the temperature of an isothermal load; such temperature mismatches are a considerable source of inefficiency in the MCC (and potentially in other devices with similar single-phase coolant loops) and will be examined in detail in the next chapter.

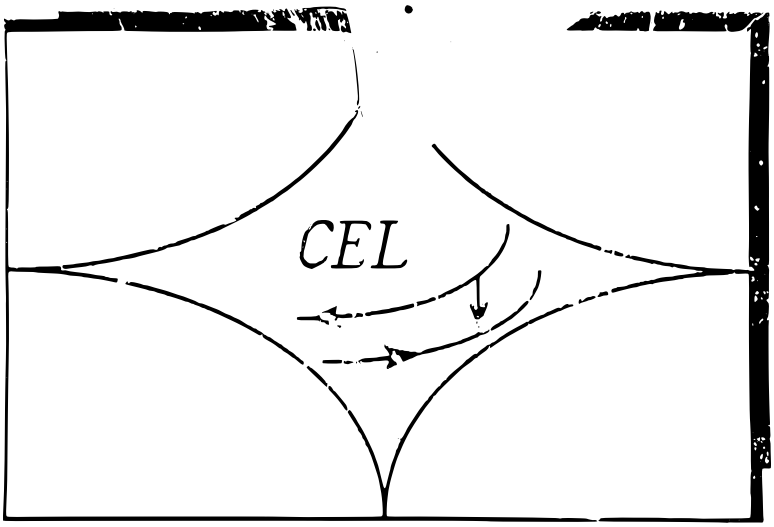

The old Cryolab logo from room 41-203.

Chapter 2

Inherent Cooler-to-Load ΔT Losses

2.1 Overview

The temperature mismatch between the working fluid and an isothermal load is a significant source of inefficiency in the modified Collins cryocooler, increasing its power requirements by an estimated ~50%. It is therefore desirable to find an alternate configuration of recuperators, load heat exchangers, and expanders (that is, an alternate cryocooler *topology*) that mitigates the temperature mismatch losses. This chapter describes how the problem may be addressed by expanding the working fluid in multiple steps, the equivalent of intercooling in compressors. After demonstrating the potential of this approach using a first-order analysis, models of seven modified-Collins-like cryocoolers with different topologies are presented and optimized; the best of these (Figure 2-1) achieves a simulated efficiency 24% higher than that of the modified Collins cryocooler in a ZBO storage application.

2.2 Analytical ΔT Loss Estimates

There are several benefits to beginning with a first-order analysis before progressing to more sophisticated modeling. First, while a simplified analysis omits some potentially-important phenomena, it can still retain enough of the fundamentals for the solution to provide insight into the physics of the system. Second, manipulating the governing equations analytically can make some trends clearer than they would be in "black box" simulations of more complex models, especially if the equations are simple enough; for example, some parameters may cancel out algebraically, both demonstrating that the solution doesn't depend on those parameters and (when the algebra is examined) demonstrating *why* this is the case. With this in mind, a much-simplified analysis of the temperature mismatch loss is presented below.

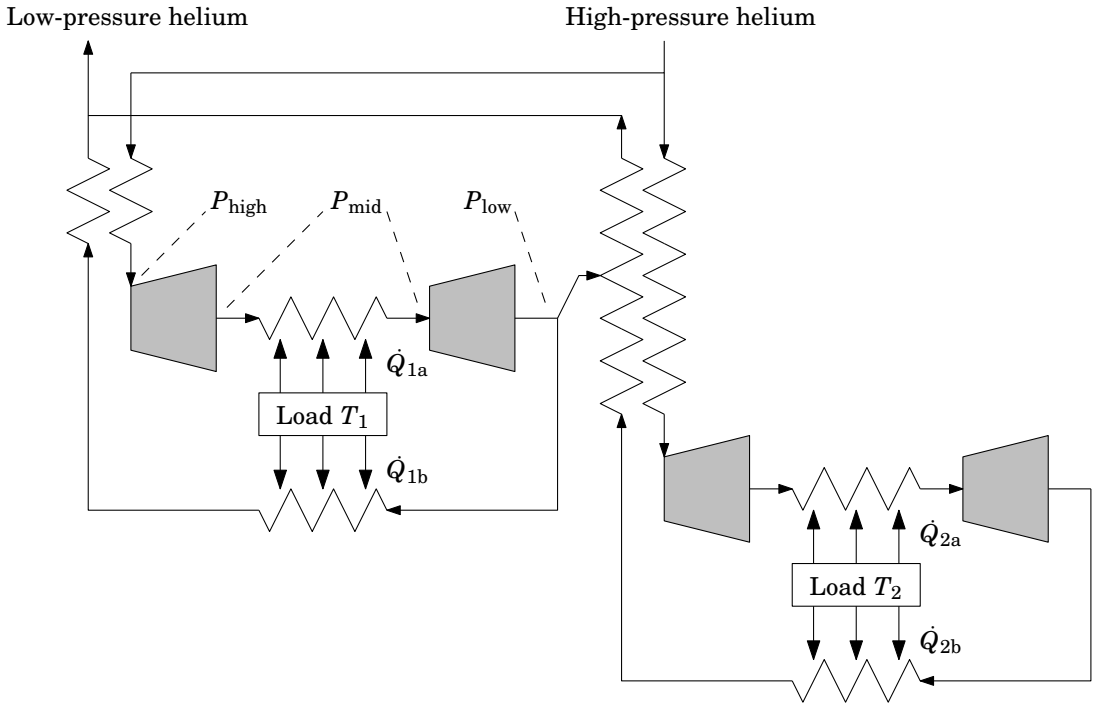

Figure 2-1: Proposed cryocooler topology using double expanders in each stage. This cryocooler benefits from a high pressure ratio in its recuperators while allowing for improved temperature matching between the isothermal loads and working fluid in the load heat exchangers. Consequently, the cryocooler has a simulated efficiency 24% higher than that of the modified Collins cryocooler pictured in Figure 1-4.

2.2.1 Simplified Cryocooler Model

The benefits of using multiple expanders can be estimated using a simplified model (Figure 2-2) in which n expanders and load heat exchangers are connected in series. All but the first expander are fed fluid (an ideal gas with constants R and c_P) from idealized load heat exchangers at a temperature of T_{load}. The first expander is fed fluid from a recuperator as in the modified Collins cryocooler. Since such cryocoolers are typically designed to have highly effective recuperators with very little temperature defect near the cold end, the temperature of the fluid entering the first expander is also approximated as T_{load} (the same temperature as fluid returning to the recuperator from the last load).

The overall cryocooler pressure ratio, Π, is defined as $P_{\text{high}}/P_{\text{low}}$. The pressure ratios of all expanders are assumed to be identical and therefore equal to $\Pi^{1/n}$. Since the inlet temperatures are fixed at T_{load}, the outlet temperature T_{out} is the same for all expanders (again, under the assumption of an ideal-gas working fluid). The heat transfer is therefore the same for each load heat exchanger and is equal to $\dot{Q}_{\text{load}}/n$. In the limit as the number of expanders and heat exchangers approaches infinity, the system behavior approaches that of a continuous isothermal expander.

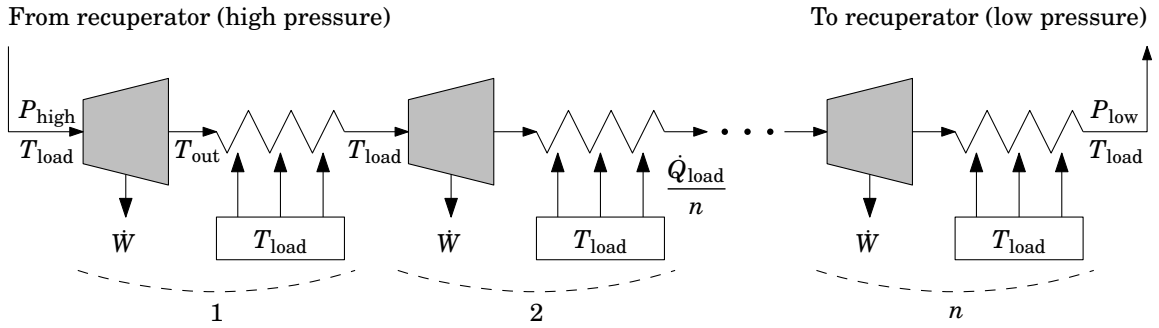

Figure 2-2: First-order model used to estimate the benefit of multiple expanders, consisting of n identical expanders and load heat exchangers in series. Note that fluid is assumed to enter from the recuperator (not shown) at a temperature of T_{load}; this is a reasonable approximation since cryocooler recuperators are generally highly effective.

2.2.2 Solution Procedure

The analysis of the n-expander system can be further simplified by assuming (for now) that all the expanders are reversible and adiabatic. The temperature T_{out} of an ideal gas exiting a single expander is found by applying the Second Law to the expander. Using a pressure ratio of $\Pi^{1/n}$,

$$T_{\text{out}} = T_{\text{load}} \Pi^{-R/(nc_P)}. \tag{2.1}$$

The total heat transfer rate $\dot{Q}_{\text{load}}$ is set by the operating requirements of the cryocooler. To find the mass flow rate $\dot{m}$ required to achieve this heat transfer rate, the First Law is applied to the load heat exchangers:

$$\dot{m} = \frac{\dot{Q}_{\text{load}}}{n c_P T_{\text{load}} \left(1 - \Pi^{-R/(nc_P)}\right)}. \tag{2.2}$$

Nondimensionalizing,

$$\frac{\dot{m} c_P T_{\text{load}}}{\dot{Q}_{\text{load}}} = \frac{1}{n \left(1 - \Pi^{-R/(nc_P)}\right)}. \tag{2.3}$$

The total entropy generation rate is found by applying the Second Law to the entire system of n expanders and heat exchangers,

$$\begin{aligned} \dot{S}_{\text{gen}} &= -\frac{\dot{Q}_{\text{load}}}{T_{\text{load}}} - \dot{m}\left(c_P \ln\left(\frac{T_{\text{load}}}{T_{\text{load}}}\right)^{=0} - R\ln(\Pi)\right) \\ &= \dot{m} R \ln(\Pi) - \frac{\dot{Q}_{\text{load}}}{T_{\text{load}}}; \end{aligned} \tag{2.4}$$

substituting $\dot{m}$ from (2.2) and nondimensionalizing,

$$\frac{\dot{S}_{\text{gen}} T_{\text{load}}}{\dot{Q}_{\text{load}}} = \frac{R}{nc_P}\left(\frac{\ln(\Pi)}{1 - \Pi^{-R/(nc_P)}}\right) - 1. \tag{2.5}$$

This dimensionless entropy generation rate is equal to the entropy generated due to the temperature mismatch ($\dot{S}_{\text{gen}}$) divided by the total entropy transferred from the load ($\dot{Q}_{\text{load}}/T_{\text{load}}$). The dimensionless entropy generation therefore compares the amount of temperature mismatch loss to the total cooling provided by the cryocooler.

The relations for the limiting isothermal expander case are found by taking the limit of (2.3) and (2.5) as $n \to \infty$:

$$\frac{\dot{m} c_P T_{\text{load}}}{\dot{Q}_{\text{load}}} = \frac{c_P/R}{\ln(\Pi)}, \tag{2.6}$$

$$\frac{\dot{S}_{\text{gen}} T_{\text{load}}}{\dot{Q}_{\text{load}}} = 0. \tag{2.7}$$

Of course, assuming an isothermal expander initially and redoing the analysis would give the same results as in (2.6) and (2.7).

The analysis thus far has been somewhat abstract; however, the results may be extended to estimate the effect on cryocooler operating power by considering the behavior of a warm-end compressor. This compressor takes in the ideal-gas working fluid from the warm end of the recuperator, compresses it in one or more stages (rejecting heat to the environment T_{env}), and returns it to the recuperator. The compressor is modeled using a fixed isothermal efficiency of η_{comp}, defined as

$$\eta_{\text{comp}} \equiv \frac{\dot{W}_{\text{comp}}}{\dot{W}_{\text{comp,iso}}} \tag{2.8}$$

where $\dot{W}_{\text{comp}}$ is the actual power required to operate the compressor and $\dot{W}_{\text{comp,iso}}$ is the power required by a reversible, isothermal compressor with the same inlet conditions and pressure ratio. As in the expander analysis, the compressor's inlet and outlet mass flows are approximated as having the same temperature (now T_{env}) due to the high-effectiveness recuperator.

The performance of an isothermal compressor is computed first; applying the Second Law and ideal gas constitutive relations to such a compressor yields

$$\frac{\dot{Q}_{\text{env,iso}}}{T_{\text{env}}} = -\dot{m} R \ln(\Pi), \tag{2.9}$$

where $\dot{Q}_{\text{env,iso}}$ is the rate at which heat is rejected to the environment. The First Law applied to the isothermal compressor simply reduces to $\dot{W}_{\text{comp,iso}} = \dot{Q}_{\text{env,iso}}$ since fluid enters and exits the compressor at the same temperature. Combining this with the Second Law result above and using (2.4) to replace $\dot{m} R \ln(\Pi)$,

$$\dot{W}_{\text{comp,iso}} = -T_{\text{env}} \left(\frac{\dot{Q}_{\text{load}}}{T_{\text{load}}} + \dot{S}_{\text{gen}} \right). \tag{2.10}$$

Finally, the actual compressor power is found by dividing the ideal power requirement

by η_{comp}. Doing so and rearranging somewhat yields

$$\dot{W}_{\text{comp}} = -\frac{\dot{Q}_{\text{load}}}{\eta_{\text{comp}}}\left(\frac{T_{\text{env}}}{T_{\text{load}}}\right)\left(1+\frac{\dot{S}_{\text{gen}}T_{\text{load}}}{\dot{Q}_{\text{load}}}\right). \tag{2.11}$$

The last term in equation (2.11) provides an important insight: *the fractional increase in compressor power due to the temperature mismatch loss is equal to the dimensionless entropy generation rate*. For example, a dimensionless entropy generation rate of 0.5 results in a compressor power requirement 50% higher than would be required with an isothermal expander.

Effect of expander irreversibility

Of course, actual expanders are not reversible; this leads to greater entropy generation, higher mass flow rates, and increased compressor power.

In an adiabatic expander, the Second Law requires the enthalpy decrease of fluid undergoing expansion to be smaller when entropy is generated than when the expander is reversible. An *adiabatic efficiency* can be defined to describe the ratio of the actual enthalpy decrease during expansion ($h_{\text{in}} - h_{\text{out}}$) to the enthalpy decrease of a reversible, adiabatic expander ($h_{\text{in}} - h_{\text{out,rev}}$):

$$\eta_{\text{exp}} \equiv \frac{h_{\text{in}} - h_{\text{out}}}{h_{\text{in}} - h_{\text{out,rev}}}. \tag{2.12}$$

A similar solution approach to that used for reversible expanders yields the following expressions for dimensionless mass flow rate and entropy generation rate when the expanders are irreversible:

$$\left[\frac{\dot{m}c_P T_{\text{load}}}{\dot{Q}_{\text{load}}}\right]_{\text{irrev}} = \frac{1}{\eta_{\text{exp}} n\left(1-\Pi^{-R/(nc_P)}\right)} \tag{2.13}$$

$$\left[\frac{\dot{S}_{\text{gen}}T_{\text{load}}}{\dot{Q}_{\text{load}}}\right]_{\text{irrev}} = \frac{R}{\eta_{\text{exp}} n c_P}\left(\frac{\ln(\Pi)}{1-\Pi^{-R/(nc_P)}}\right) - 1. \tag{2.14}$$

The limiting isothermal cases of these expressions are:

$$\left[\frac{\dot{m}c_P T_{\text{load}}}{\dot{Q}_{\text{load}}}\right]_{\text{irrev}} = \frac{c_P/R}{\eta_{\text{exp}}\ln(\Pi)} \tag{2.15}$$

$$\left[\frac{\dot{S}_{\text{gen}}T_{\text{load}}}{\dot{Q}_{\text{load}}}\right]_{\text{irrev}} = 1/\eta_{\text{exp}} - 1. \tag{2.16}$$

As expected, the entropy generation rates are higher when the adiabatic expander efficiency is lower, as entropy is now generated by both the temperature mismatch and the expander irreversibility. The limiting isothermal case is no longer reversible.

Note also that the dimensionless mass flow rate expressions (2.13) and (2.15) are essentially unchanged from their reversible-expander counterparts (2.3) and (2.6) except for being divided by the adiabatic efficiency. A lower adiabatic efficiency results in a proportionally higher mass flow rate, which in turn requires more compressor power.

Importantly, the inclusion of η_{exp} does not change how the mass flow rate scales with the number of expanders; this directly affects the resulting compressor power:

$$\left[\dot{W}_{\text{comp}}\right]_{\text{irrev}} = -\frac{\dot{Q}_{\text{load}}}{\eta_{\text{comp}}\,\eta_{\text{exp}}}\left(\frac{T_{\text{env}}}{T_{\text{load}}}\right)\left(1+\underbrace{\frac{\dot{S}_{\text{gen}}T_{\text{load}}}{\dot{Q}_{\text{load}}}}_{\text{from (2.5)}}\right). \tag{2.17}$$

Even with irreversible expanders, therefore, the dimensionless entropy generation from the *reversible* expander analysis (equation (2.5)) still predicts the fractional increase in compressor power from temperature mismatch losses in this simplified model.

2.2.3 Results & Discussion

The cryocooler in this work is expected to operate at a pressure ratio of $\Pi \approx 10$; this is typical of other DC-flow cryocoolers [HKG+06] and is approaching the upper range of what is achievable with practical compressors. For a single-expander cryocooler ($n = 1$) operating at this pressure ratio, equation (2.5) gives a dimensionless entropy generation rate of 0.53. It follows that the temperature mismatch loss adds an estimated 53% to the cryocooler's operating power, or conversely, that eliminating the loss entirely would increase the cryocooler's efficiency by about 53% (as well as reduce the heat rejection to the environment $\dot{Q}_{\text{env}}$ and the physical size of the compressor). This result verily confirms the importance of the temperature mismatch loss.

The dimensionless mass flow rate (2.3) and dimensionless entropy generation rate (2.5) are plotted on semi-log axes in Figure 2-3 for $n = 1$, 2, and 4, along with the limiting isothermal case ($n \to \infty$). For both plots, a ratio of $R/c_P = 0.4$ is used, corresponding to a monatomic gas such as helium. The plots demonstrate the expected trends: higher pressure ratios allow for lower mass flow rates at the expense of increased temperature mismatch losses, and using multiple expanders reduces the temperature mismatch losses (and consequently the required mass flow rate at a given pressure ratio).

The dimensionless entropy generation plot (Figure 2-3b) reveals that the temperature mismatch loss increases almost logarithmically with pressure ratio; each ten-fold increase in pressure ratio increases the loss by a fixed amount of ~0.5. Additionally, the temperature mismatch loss is approximately proportional to the inverse of the number of expanders. This suggests the following approximate heuristic, valid for ideal monatomic working fluids and accurate to within 16% of equation (2.5) for

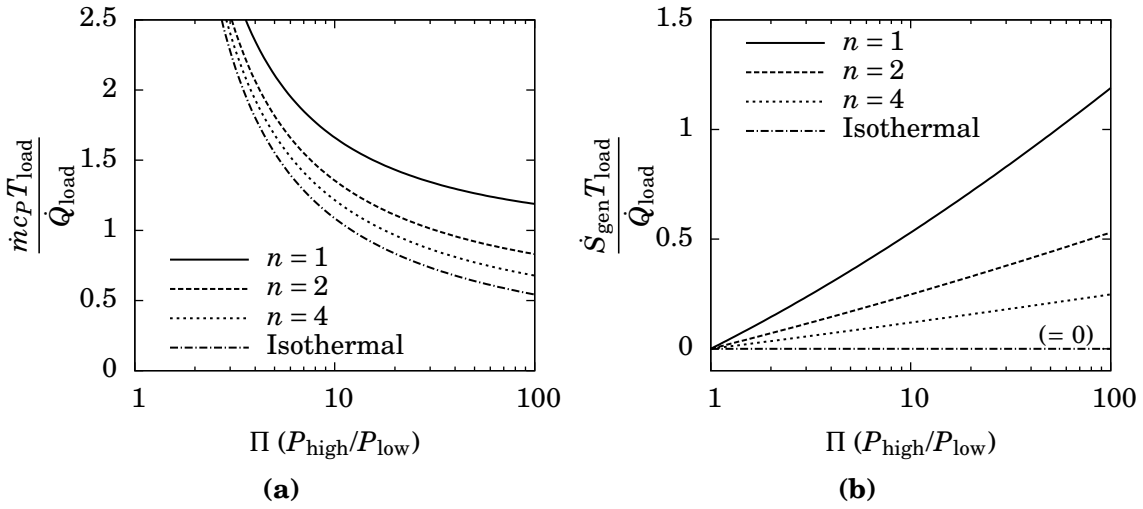

Figure 2-3: (a) Dimensionless mass flow rate and (b) dimensionless entropy generation rate for various values of n. Higher pressure ratios decrease the mass flow rate at the expense of increased temperature mismatch losses, while using multiple expanders mitigates these losses (and also reduces the mass flow rate).

pressure ratios below 100:

$$\frac{\dot{S}_{\text{gen}} T_{\text{load}}}{\dot{Q}_{\text{load}}} \approx \frac{1}{2} \frac{\log_{10}(\Pi)}{n}. \tag{2.18}$$

This heuristic can be justified mathematically by using a series expansion of (2.5) in semi-log space; the details are given in Appendix A.1. Equation (2.18) can also be extended to allow arbitrary ideal gases by replacing the factor of 1/2 with $\frac{5}{4}R/c_P$:

$$\frac{\dot{S}_{\text{gen}} T_{\text{load}}}{\dot{Q}_{\text{load}}} \approx \left(\frac{5R}{4c_P}\right) \frac{\log_{10}(\Pi)}{n}. \tag{2.19}$$

For a diatomic gas such as nitrogen the leading coefficient would then become 1/2.8. Again, justification is provided in Appendix A.1.

The entropy generation and mass flow rate plots in Figure 2-3 also show diminishing returns from adding additional expanders. This trend may be presented in terms of the cryocooler's Second-Law efficiency efficiency η, defined as the ratio between the power consumption of a reversible Carnot refrigerator with the same loads and operating temperatures ($\dot{W}_{\text{rev}}$) and the actual power consumption of the irreversible cryocooler ($\dot{W}_{\text{actual}}$):

$$\eta \equiv \frac{\dot{W}_{\text{rev}}}{\dot{W}_{\text{actual}}} = \frac{\dot{W}_{\text{rev}}}{\dot{W}_{\text{comp}}}. \tag{2.20}$$

Note that $\dot{W}_{\text{actual}}$ may be replaced with the compressor power $\dot{W}_{\text{comp}}$ since the expanders contribute no usable work in the current design. Using this definition, the

efficiency gained by using n expanders instead of one expander is

$$\begin{aligned}\frac{\eta_n - \eta_1}{\eta_1} &= \left(\frac{\dot{W}_{\text{rev}}}{\dot{W}_{\text{comp},n}} - \frac{\dot{W}_{\text{rev}}}{\dot{W}_{\text{comp},1}}\right) \Bigg/ \frac{\dot{W}_{\text{rev}}}{\dot{W}_{\text{comp},1}} \\ &= \frac{\dot{W}_{\text{comp},1}}{\dot{W}_{\text{comp},n}} - 1 \\ &= \frac{n\left(1 - \Pi^{-R/(nc_P)}\right)}{1 - \Pi^{-R/c_P}} - 1, \end{aligned} \tag{2.21}$$

where η_n and $\dot{W}_{\text{comp},n}$ are the efficiency and compressor power of an n-expander cryocooler and η_1 and $\dot{W}_{\text{comp},1}$ are those of a one-expander cryocooler. Equation (2.21) is plotted in Figure 2-4a for various pressure ratios.

It may also prove useful to know the incremental benefit of each additional expander (for example, the efficiency gained by using three expanders instead of two); this is found in much the same way,

$$\frac{\eta_n - \eta_{n-1}}{\eta_{n-1}} = \frac{n\left(1 - \Pi^{-R/(nc_P)}\right)}{(n-1)\left(1 - \Pi^{-R/([n-1]c_P)}\right)} - 1, \tag{2.22}$$

and is plotted in Figure 2-4b.

The efficiency gains decrease quickly as the number of expanders increases. The gain from using two expanders instead of one is 22.6% at a pressure ratio of 10. A third expander increases the efficiency by another 7.5%, and a fourth expander by an additional 3.7%. Of course, the optimum trade-off between efficiency and number of

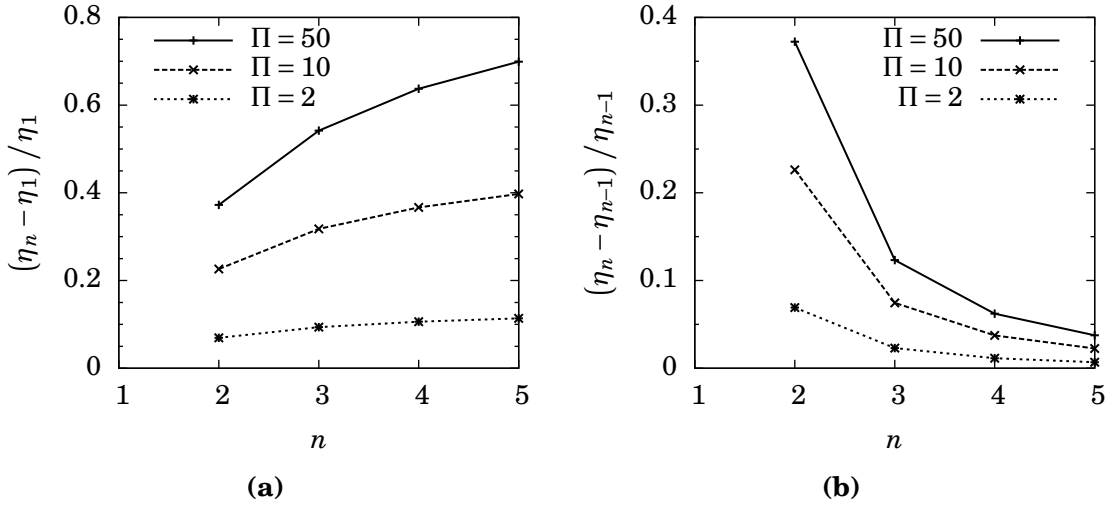

Figure 2-4: (a) Total and (b) incremental gains in cryocooler efficiency from using n expanders and load heat exchangers. The benefit of additional expanders diminishes considerably as more expanders are used.

expanders will depend on the cost, weight, complexity, and reliability of the added expanders.

2.3 Numerical ΔT Loss Simulations

The analysis above is useful as a first-order estimate, but lacks the detail needed to understand the effects of double expansion in a practical cryocooler or optimize the distribution of recuperator sizes and precooling mass flow rates. To this effect, models were developed for seven modified-Collins-like cryocoolers (illustrated in Figure 2-5):

1. **Single-Pre-Single:** a three-stage cryocooler which provides cooling to loads with the first and third stages and devotes the second stage exclusively to providing a precooling flow.
2. **Pre-Single-Single:** a three-stage cryocooler similar to *Single-Pre-Single*, but with first stage devoted to precooling and the second and third stages providing cooling to the loads.
3. **Single-Single:** a two-stage cryocooler (the baseline that all other configurations were compared to).
4. **No Precool:** a two-stage cryocooler *without* a precooling flow between its stages, intended to give insight into the importance of precooling.
5. **Double-Single:** a two-stage cryocooler with double expanders in the first stage and a single expander in the second stage.
6. **Single-Double:** a two-stage cryocooler with a single expander in the first stage and double expanders in the second stage.
7. **Double-Double:** a two-stage cryocooler with double expanders in both stages.

2.3.1 Cryocooler Models

For each of the seven configurations, two models were created: one using a pure substance model of the working fluid, the other using an ideal gas model. All of the models were optimized numerically to find the mass flow rates and recuperator sizes that minimized the compressor power requirement while simultaneously providing 100 W of cooling at 100 K and 20 W of cooling at 25 K. These loads are tailored to long-term storage of cryogenic propellants, and are based on NASA's 2007 Small Business Technology Transfer solicitations [NASA07].

Each of the cryocooler models were constructed from "building block" models of the compressor, recuperator, expander, and load heat exchanger, described below. Pressure drops were neglected in all flow passages connecting the components. In the

following analyses, $h()$ and $s()$ are the specific enthalpy and entropy of the working fluid, expressed as functions of other state properties of the fluid. For an ideal gas, they are given by the following enthalpy and entropy constitutive relations:

$$h(T,P) = c_P(T - T_0), \tag{2.23}$$

$$s(T,P) = c_P \ln(T/T_0) - R \ln(P/P_0), \tag{2.24}$$

where T_0 and P_0 define an arbitrary reference state for the ideal gas.

Compressor

As in section 2.2.1, the compressor raises the pressure of the helium working fluid from 0.1 MPa to 1.0 MPa and rejects heat and entropy to the environment at temperature T_{env}. A similar analysis approach was also used: the input power was first found for a reversible compressor and then divided by an isothermal efficiency (assumed constant) to find the actual compressor power. While this is not strictly consistent with the definition of isothermal efficiency (which is based on a reversible isothermal compressor rejecting heat at the *suction* temperature), the two definitions differ by at most ~0.2% for the cryocoolers simulated.

Applying the Second Law to a reversible compressor rejecting heat at T_{env} and isolating the rate of heat rejection $\dot{Q}_{\text{env,iso}}$,

$$\dot{Q}_{\text{env,iso}} = \dot{m} T_{\text{env}} \left[s(T_{\text{in}}, P_{\text{in}}) - s(T_{\text{env}}, P_{\text{out}}) \right], \tag{2.25}$$

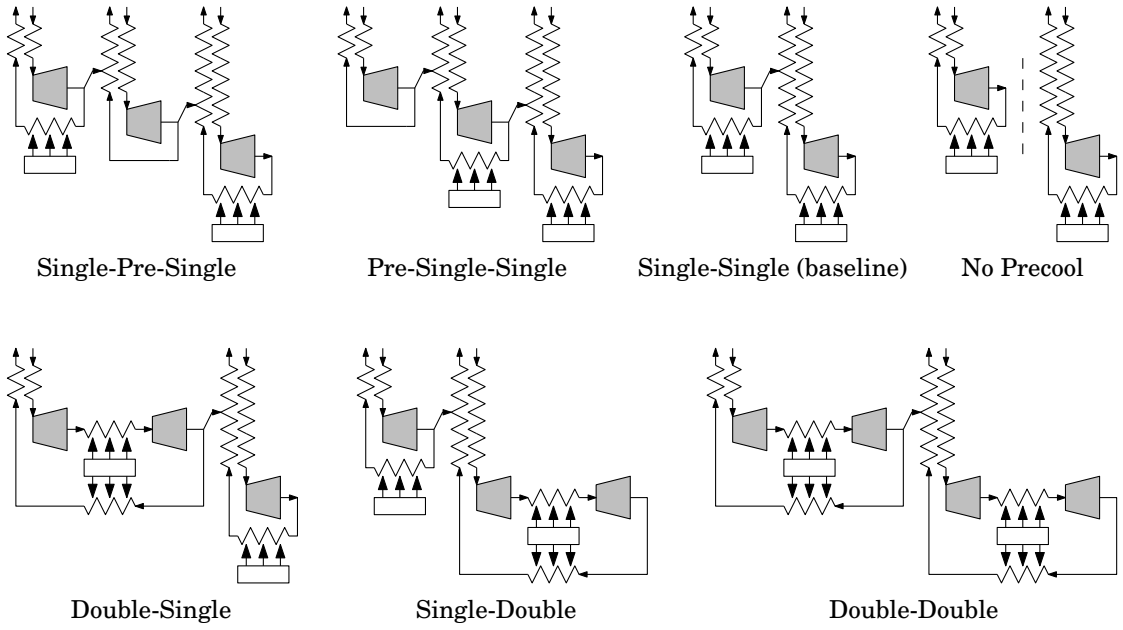

Figure 2-5: Seven cryocoolers designs with different topologies (drawn in the style of Figures 1-4 and 2-1). Models of these cryocoolers were used to gain insight into the effect of double expansion in practical multi-stage cryocoolers and to assess the importance of precooling flows.

where T_{in} and P_{in} are the temperature and pressure of fluid entering the compressor and T_{env} and P_{out} are the temperature and pressure of fluid exiting the compressor. Substituting $\dot{Q}_{\text{env,iso}}$ into the First Law and isolating the ideal compressor power $\dot{W}_{\text{comp,iso}}$,

$$\dot{W}_{\text{comp,iso}} = \dot{m}\left[h(T_{\text{in}},P_{\text{in}}) - h(T_{\text{env}},P_{\text{out}})\right] + \overbrace{\dot{m}T_{\text{env}}\left[s(T_{\text{in}},P_{\text{in}}) - s(T_{\text{env}},P_{\text{out}})\right]}^{\dot{Q}_{\text{env,iso}}}. \quad (2.26)$$

The actual compressor power is therefore given by

$$\dot{W}_{\text{comp}} = \frac{\dot{m}}{\eta_{\text{comp}}}\left[h(T_{\text{in}},P_{\text{in}}) - h(T_{\text{env}},P_{\text{out}})\right] + \frac{\dot{m}T_{\text{env}}}{\eta_{\text{comp}}}\left[s(T_{\text{in}},P_{\text{in}}) - s(T_{\text{env}},P_{\text{out}})\right]. \quad (2.27)$$

To find the compressor power assuming an ideal gas model of the working fluid, $h(T,P)$ and $s(T,P)$ are simply replaced with the corresponding enthalpy and entropy constitutive relations:

$$\dot{W}_{\text{comp}} = \frac{\dot{m}c_P}{\eta_{\text{comp}}}(T_{\text{in}} - T_{\text{env}}) + \frac{\dot{m}T_{\text{env}}}{\eta_{\text{comp}}}\left[c_P \ln\left(\frac{T_{\text{env}}}{T_{\text{in}}}\right) - R\ln\left(\frac{P_{\text{out}}}{P_{\text{in}}}\right)\right]. \quad (2.28)$$

In early simulations of the modified Collins cryocooler, Hannon et al. assumed the compressor had an isothermal efficiency of 50%; this was described as "consistent with the state-of-the-art of a two-stage intercooled terrestrial compressor" [HGT+03]. This earlier version of the MCC assumed a pressure ratio of 15:1 and a compressor power of ~500 W. For a much larger system with a ~300 kW helium compressor operating at a pressure ratio of 6:1, Staats suggested that an isothermal efficiency of 65% was appropriate [Sta08, pp. 46–47]. As the compressor in the present work is intermediate to these in both pressure ratio (10:1) and power consumption (~3 kW), an efficiency of $\eta_{\text{comp}} = 60\%$ seems reasonable.

Recuperators

The recuperator models in this work were greatly simplified. While the specific heat variations and precooling streams mentioned in Chapter 1 were included, radiation heat transfers and axial conduction were not. Preliminary estimates based on the work of Nellis [Nel03] suggest that these effects are not the dominant source of recuperator ineffectiveness but are nevertheless significant; as a result, the recuperator models probably underpredict the benefit of precooling flows. Pressure drops were also neglected in the models, and the heat transfer coefficient U was assumed to be independent of flow conditions and uniform throughout the recuperator.

In the absence of axial conduction a precooled recuperator can be treated as two separate recuperators with no precooling, one on either side of the precooling stream insertion point (Figure 2-6). The low-pressure stream exiting the cold section of the recuperator is assumed to mix completely and adiabatically with the precooling stream before entering the warm section at a temperature of T_{mix}.

Pure substance model: The governing differential equation for a recuperator may be obtained by applying the First Law to differential control volumes in each of the two fluid streams and combining these with Newton's law of heat transfer for a differential area dA. A complete derivation is given by Cravalho and Smith [CS81], and results in the following equation (reproduced here slightly altered and with different notation):

$$\frac{d(T_1 - T_2)}{T_1 - T_2} = \left(\frac{1}{\dot{m}_1 c_P(T_1, P_1)} + \frac{1}{\dot{m}_2 c_P(T_2, P_2)} \right) U \, dA. \tag{2.29}$$

Subscript "1" refers to the stream that flows from the warm end to the cold end (the high-pressure stream in a modified-Collins cryocooler), and subscript "2" refers to the stream that flows from the cold end to the warm end (the low-pressure stream). In the general case, the specific heat capacity at constant pressure $c_P(T,P)$ is a function of temperature and pressure.

Since the specific heat capacity of the working fluid may vary substantially over the range of temperatures present in a recuperator, equation (2.29) must be integrated numerically. To this effect, each section of the recuperator is divided into 50 small segments which each span a small enough temperature difference that c_P can be assumed constant. Solutions from integrating (2.29) with a constant c_P are given by Cravalho and Smith; applying them to a segment with heat transfer area ΔA yields

$$T_1|_{A+\Delta A} = T_1 + \frac{T_1 - T_2}{\dot{m}_1 c_{P1} / \dot{m}_2 c_{P2} - 1} \left[1 - \exp\left(\frac{U \Delta A}{\dot{m}_1 c_{P1}} - \frac{U \Delta A}{\dot{m}_2 c_{P2}} \right) \right], \tag{2.30a}$$

$$T_2|_{A+\Delta A} = T_2 + \frac{T_1 - T_2}{1 - \dot{m}_2 c_{P2} / \dot{m}_1 c_{P1}} \left[1 - \exp\left(\frac{U \Delta A}{\dot{m}_1 c_{P1}} - \frac{U \Delta A}{\dot{m}_2 c_{P2}} \right) \right], \tag{2.30b}$$

where c_{P1} and c_{P2} are the specific heat capacity of streams 1 and 2, computed using the known stream temperatures at the cold end of the segment (T_1 and T_2).

Equation (2.30) can be applied iteratively starting at the cold end of a non-precooled recuperator to find its temperature profile, assuming both stream temperatures at the cold end are known. The following solution approach is used:

1. Start with both cold-end temperatures ($T_{1,\text{out}}$ and $T_{2,\text{in}}$).
2. For each segment, starting at the cold end:
   (a) Compute the specific heat capacity of both streams using a suitable equation of state.
   (b) Use equation (2.30) with the specific heat capacities computed in step 2a to find the temperatures at the cold end of the next segment.
3. Continue until the temperatures at the warm end of the recuperator ($T_{1,\text{in}}$ and $T_{2,\text{out}}$) are known.

If the recuperator is precooled, the solution approach is applied separately to the cold and warm sections of the recuperator (both subdivided into 50 segments each) with

the following mixing equation used in between:

$$T_{\text{mix}} = T(h_{\text{mix}}, P_{\text{low}}), \quad \text{where} \quad h_{\text{mix}} = \frac{\dot{m}_2^* h(T_2^*, P_{\text{low}}) + \dot{m}_{\text{pre}} h(T_{\text{pre}}, P_{\text{low}})}{\dot{m}_2^* + \dot{m}_{\text{pre}}}. \tag{2.31}$$

T_2^* and $\dot{m}_2^*$ are the temperature and mass flow rate of the low-pressure recuperator stream immediately prior to mixing; since the mass flow rate is uniform throughout the cold section of the recuperator, $\dot{m}_2^* = \dot{m}_{2,\text{in}}$, the mass flow rate entering stream 2 at the cold end. T_{pre} and $\dot{m}_{\text{pre}}$ are the temperature and mass flow rate of the precooling stream.

The solution approach above is not perfect since it bases the specific heat capacities of the fluid in each segment only on the temperatures at its cold end, but if the segments are kept small enough the errors should be smaller than those introduced by other assumptions (e.g., from neglecting axial conduction).

Ideal gas model: There is no need to use an approximate method under an ideal gas assumption because c_P is constant for an ideal gas; equation (2.30) can therefore be simplified with the ideal gas enthalpy constitutive relation and used to relate the warm-end and cold-end temperatures of an entire non-precooled recuperator:

$$\overbrace{T_{1,\text{in}}}^{\text{warm end}} = \overbrace{T_{1,\text{out}} + \frac{T_{1,\text{out}} - T_{2,\text{in}}}{\dot{m}_1/\dot{m}_2 - 1}\left[1 - \exp\left(\frac{UA}{\dot{m}_1 c_P} - \frac{UA}{\dot{m}_2 c_P}\right)\right]}^{\text{cold end}}, \tag{2.32a}$$

$$T_{2,\text{out}} = T_{2,\text{in}} + \frac{T_{1,\text{out}} - T_{2,\text{in}}}{1 - \dot{m}_2/\dot{m}_1}\left[1 - \exp\left(\frac{UA}{\dot{m}_1 c_P} - \frac{UA}{\dot{m}_2 c_P}\right)\right], \tag{2.32b}$$

where A is now the total heat transfer area of the recuperator. If the recuperator is precooled, equation (2.32) must be applied to each section of the recuperator separately, with the area and mass flow rates of each section being used in turn. The pure-substance mixing equation (2.31) can also be simplified, yielding

$$T_{\text{mix}} = \frac{\dot{m}_2^* T_2^* + \dot{m}_{\text{pre}} T_{\text{pre}}}{\dot{m}_2^* + \dot{m}_{\text{pre}}}. \tag{2.33}$$

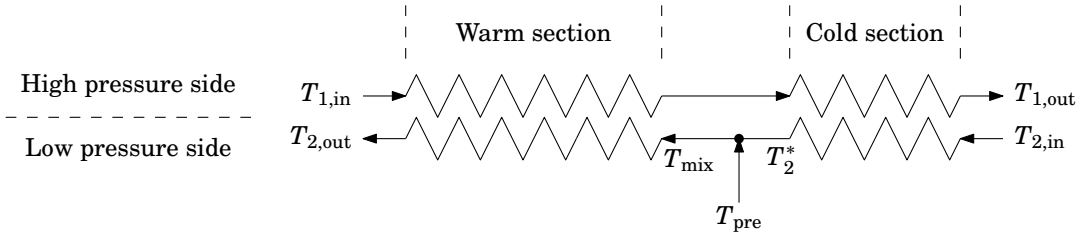

Figure 2-6: Schematic of a precooled recuperator. In the absence of axial conduction, the recuperator may be treated as two separate heat exchangers with an adiabatic mixing section in between.

To make the cryocooler models easier to optimize (discussed further in section 2.3.2), it is desirable to model the recuperator in a way that matches is physical behavior: given the mass flow rates and temperatures at the inputs, find the corresponding outputs. Equation (2.32) is therefore applied to each section of a precooled recuperator, combined with the First Law for the entire recuperator and the mixing equation (2.33), and algebraically manipulated to yield the output temperatures of both streams in terms of the input temperatures and mass flow rates:

$$\textbf{Output at cold end:} \quad T_{1,\text{out}} = T_{2,\text{in}}(1 - 1/F_5) + T_{2,\text{mid}}/F_5, \tag{2.34a}$$

$$\textbf{Output at warm end:} \quad T_{2,\text{out}} = \frac{T_{2,\text{in}}\dot{m}_{2,\text{in}} + (T_{1,\text{in}} - T_{1,\text{out}})\dot{m}_{1,\text{in}} + T_{\text{pre}}\dot{m}_{\text{pre}}}{\dot{m}_{2,\text{in}} + \dot{m}_{\text{pre}}}, \tag{2.34b}$$

where $T_{2,\text{mid}}$ is given by

$$T_{2,\text{mid}} = \frac{T_{2,\text{in}}(F_3 + 1) + T_{1,\text{in}}F_4 + T_{\text{pre}}(F_2F_3F_4)}{(F_3 + 1)(F_4 + 1) - F_1F_3F_4} \tag{2.35}$$

and the dimensionless factors F_1–F_5 are defined in terms of the areas A_{warm} and A_{cold} of the two sections of the recuperator (and other known variables):

$$F_1 \equiv \frac{\dot{m}_{2,\text{in}}}{\dot{m}_{2,\text{out}}} \quad (\text{where } \dot{m}_{2,\text{out}} = \dot{m}_{2,\text{in}} + \dot{m}_{\text{pre}}) \tag{2.36a}$$

$$F_2 \equiv \frac{\dot{m}_{\text{pre}}}{\dot{m}_{2,\text{out}}} \tag{2.36b}$$

$$F_3 \equiv \frac{1}{\dot{m}_{1,\text{in}}/\dot{m}_{2,\text{out}} - 1}\left[1 - \exp\left(\frac{UA_{\text{warm}}}{\dot{m}_{1,\text{in}}c_P} - \frac{UA_{\text{warm}}}{\dot{m}_{2,\text{out}}c_P}\right)\right] \tag{2.36c}$$

$$F_4 \equiv \frac{1}{\dot{m}_{2,\text{in}}/\dot{m}_{1,\text{in}} - 1}\left[1 - \exp\left(\frac{UA_{\text{cold}}}{\dot{m}_{2,\text{in}}c_P} - \frac{UA_{\text{cold}}}{\dot{m}_{1,\text{in}}c_P}\right)\right] \tag{2.36d}$$

$$F_5 \equiv \frac{1}{1 - \dot{m}_{2,\text{in}}/\dot{m}_{1,\text{in}}}\left[1 - \exp\left(\frac{UA_{\text{cold}}}{\dot{m}_{1,\text{in}}c_P} - \frac{UA_{\text{cold}}}{\dot{m}_{2,\text{in}}c_P}\right)\right] \tag{2.36e}$$

Load heat exchangers

As described in Chapter 1, the heat exchangers used in a ZBO application of modified Collins cryocoolers may extend directly into cryogen tanks to provide good working-fluid-to-cryogen heat transfer. For this and other applications, a tradeoff must eventually be made between heat exchanger effectiveness, size, and pressure drop. Pending these details, however, a simplified model of the heat exchanger is used: working fluid is assumed to exit the heat exchanger with an absolute temperature equal to 95% of the load temperature. For example, if the load temperature is 100 K, the fluid is assumed to exit at 95 K regardless of the input temperature and flow rate, leaving a temperature difference of 5 K between the load and the fluid. The pressure drop in the heat exchanger is neglected.

The governing equation is found by applying the First Law to the load heat exchanger:

$$T_{\text{out}} = T(h_{\text{out}}, P), \quad \text{where} \quad h_{\text{out}} = h(T_{\text{in}}, P) + \dot{Q}_{\text{load}}/\dot{m}. \tag{2.37}$$

T_{in} and T_{out} are the temperatures of the working fluid entering and exiting the heat exchanger, P is the fluid's pressure, $\dot{m}$ is the fluid's mass flow rate, and $\dot{Q}_{\text{load}}$ is the total heat transfer rate from the load to the fluid. For an ideal gas working fluid,

$$T_{\text{out}} = T_{\text{in}} + \dot{Q}_{\text{load}}/(\dot{m} c_P). \tag{2.38}$$

Expanders

The expanders were modeled as irreversible, adiabatic devices with a constant adiabatic efficiency (defined in equation (2.12)). An efficiency of $\eta_{\text{exp}} = 75\%$ was chosen to match the expander efficiency used by Hannon et al. [HGT+03]. As described in Chapter 1, the warm end of the expander was assumed to dissipate any work extracted from the cold-end working fluid.

While an expander model with constant adiabatic efficiency was considered sufficient for comparing various cryocooler topologies, the actual efficiency of a floating piston expander depends on its geometry and operating conditions. A more detailed expander analysis including these effects is presented in Chapter 3.

The entropy of a fluid undergoing *reversible* adiabatic expansion remains constant according to the Second Law since no entropy is generated or transferred into the fluid. The entropy of fluid exiting the expander may therefore be written in terms of the state of fluid entering the expander:

$$s_{\text{out,rev}} = s_{\text{in}} = s(T_{\text{in}}, P_{\text{in}}). \tag{2.39}$$

With the entropy known, the reversible outlet enthalpy is easily computed using the fluid's equation of state:

$$h_{\text{out,rev}} = h(s_{\text{out,rev}}, P_{\text{out}}). \tag{2.40}$$

The actual output enthalpy of an irreversible expander may be found in terms of $h_{\text{out,rev}}$ by using the definition of adiabatic efficiency from (2.12),

$$h_{\text{out}} = h_{\text{in}}(T_{\text{in}}, P_{\text{in}}) + \eta_{\text{exp}} \left[h_{\text{in}}(T_{\text{in}}, P_{\text{in}}) - h_{\text{out,rev}} \right], \tag{2.41}$$

followed by the actual output temperature:

$$T_{\text{out}} = T(h_{\text{out}}, P_{\text{out}}). \tag{2.42}$$

A similar analysis for an ideal gas yields

$$T_{\text{out}} = T_{\text{in}} - \eta_{\text{exp}} \left[1 - \left(\frac{P_{\text{out}}}{P_{\text{in}}} \right)^{R/c_P} \right] T_{\text{in}}. \tag{2.43}$$

2.3.2 Solution Procedure

Having developed the governing equations needed to model a cryocooler, the next step is to solve the system of equations to find the best performance of each of the seven models presented at the beginning of section 2.3. All of these models were implemented in Microsoft Excel 2003, chosen for its visual interface which greatly simplified the debugging process. For the pure-substance-based models the McCarty and Arp helium equation of state was used as implemented in REFPROP 8.0 [MA90, LHM07], with some slight modification to REFPROP's Excel interface to correct a bug in the software. In all of the models, the following quantities were left as inputs:

1. The mass flow rate into each stage.

2. The fraction of each stage's mass flow rate devoted to precooling, when needed.

3. The intermediate pressure between the double expanders, when needed.

4. The distribution of recuperator UA between stages (and between the warm and cold sections of precooled recuperators when needed).

Note that only the distribution of recuperator UA was varied; the total UA was fixed at 300 W/K for all models. This value was selected by computing the UA in Chaudhry's cryocooler [Cha05] and using it as a guideline. Since Chaudhry's cryocooler had smaller cooling requirements (1 W at 10 K) than the cryocooler in this work, Chaudhry's UA was scaled proportionally to the size of the cryocooler in this work, using the total entropy transfer $\dot{Q}_{\text{load}}/T_{\text{load}}$ of each cryocooler as a measure of "size".

In hindsight, this was not the best way to size the recuperators. While the approach should yield a recuperator effectiveness similar to Chaudhry's under a particular set of assumptions (most importantly, that the cryocoolers have the same pressure ratio), constant effectiveness does not imply constant performance in cryogenic applications. On the contrary: constant effectiveness gives a larger stream-to-stream temperature difference in the coldest stages of a cryocooler (where the recuperator must span a bigger temperature range between the warm and cold ends), while cryogenic applications favor smaller temperature differences at lower temperatures. As a result, higher-effectiveness recuperators are required to achieve a given performance for lower temperature applications. Chaudhry's 10 K recuperator effectiveness may therefore be too high for the 25–100 K cryocooler in this work.

Excel's packaged Solver add-in [FLWW98] was used to solve and optimize the variables in each model to minimize compressor power. Scaling constants were used to narrow the disparity in magnitude between the input variables, the constraints, and the computed compressor power, though no attention was given to the scaling or condition number of the Hessian.

2.3.3 Results & Discussion

The optimized Second Law efficiencies of all the cryocooler models are plotted and compared to the baseline *Single-Single* configuration in Figure 2-7, and numerical results are listed in Tables 2.1 and 2.2. In all cases the optimizer found a solution, though considerable manual intervention was needed to obtain the solution shown for the pure-substance-based model of the *Single-Pre-Single* cryocooler.

Results agree with first-order estimates

As Table 2.1 shows, the efficiency gained by using double expanders in both stages was calculated as 24.1% using a pure substance model and 25.4% using an ideal gas model. These results agree well with the estimated gain of 22.6% obtained from equation (2.21) earlier in this chapter.

The gains found using the detailed models are greater than those predicted by the first-order model, which doesn't simulate changes in recuperator performance for the different configurations. This is easily explained. When double expanders are added, the total mass flow rate through the cryocooler decreases (recall Figure 2-3a). Since the recuperator area shared between the stages is constant and the heat transfer coefficient U is independent of mass flow rate in these models, a lower $\dot{m}$ results in a higher recuperator effectiveness. This improves the efficiency of the double expander configurations as observed.

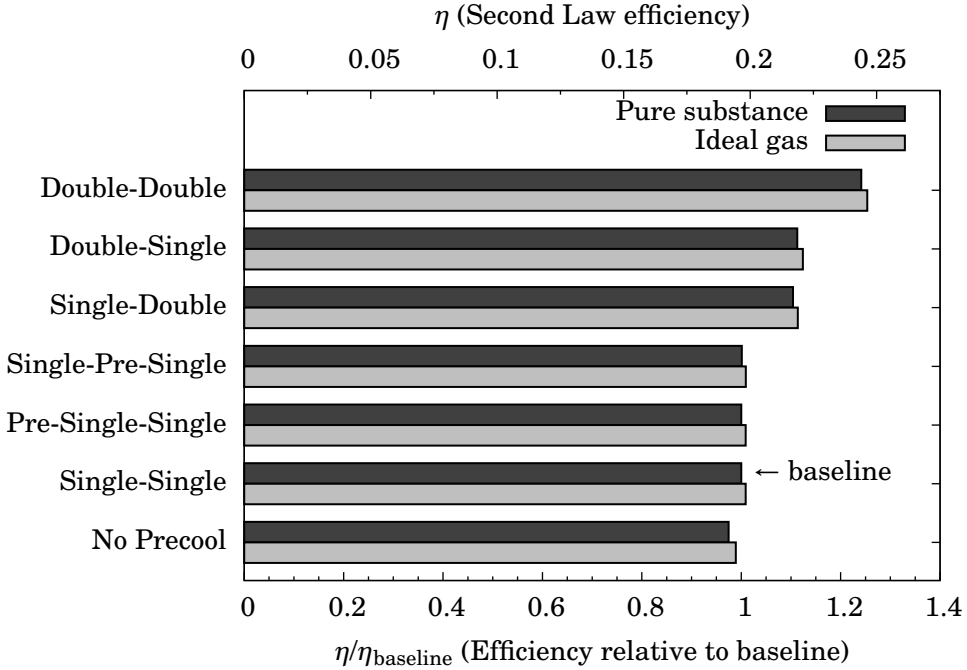

Figure 2-7: Optimized Second Law efficiencies (top axis) and relative efficiencies (bottom axis) of all simulated cryocooler topologies. The pure-substance-based *Single-Single* model is used as the baseline to which all results are compared.

Table 2.1: Compressor power inputs and efficiencies of all cryocooler configurations.

	Pure substance			Ideal gas
Configuration	Compressor power input [W]	Second Law efficiency [%]	Efficiency rel. to baseline [%]	Efficiency rel. to baseline [%]
Double-Double	1722	24.4	124.1	125.4
Double-Single	1921	21.9	111.3	112.4
Single-Double	1936	21.7	110.4	111.4
Single-Pre-Single	2135	19.7	100.1	100.9
Pre-Single-Single	2138	19.6	100.0	100.9
Single-Single	2138	19.6	(baseline)	100.9
No Precool	2193	19.1	97.5	98.9

Table 2.2: Recuperator sizes, mass flow rates, and precooling temperatures for precooled two-stage configurations. The mass flow rates listed for the 100 K and 25 K stages are those entering each stage's recuperator from the compressor (due to the precooling flows, these are slightly different from those exiting the recuperators). Pure substance results are used for all values.

	Recuperator UA [W/K]		Mass flow rate [mg/s]			
Configuration	100 K	25 K	100 K	25 K	Precool	Precool Temp. [K]
Double-Double	105.1	194.9	401.7	317.1	6.2	69.7
Double-Single	92.0	208.0	410.0	392.1	8.3	69.9
Single-Double	119.8	180.2	493.4	314.9	6.8	55.5
Single-Single	106.1	193.9	503.1	389.3	8.9	56.1

To confirm that changes in recuperator performance are responsible for these additional gains, the total UA of the *Single-Single* and *Double-Double* ideal-gas-based models was increased from 300 W/K to 30,000 W/K. This larger value mimics the ideal-recuperator assumption in the first-order n-expander model, and indeed yields a gain of 22.640% (effectively identical to the first-order estimated gain of 22.627% found in section 2.2.1).

Per-stage gains are mutually independent in the current model

In addition to agreeing with first-order estimates, the multi-stage simulation results also have an interesting property: the power saved by doubling the 100 K stage is always ~215 W regardless of the configuration of the 25 K stage, and the power saved by doubling the 25 K stage is always ~200 W regardless of the configuration of the 100 K stage (Table 2.3). Stated another way, the gains from double expansion are roughly cumulative: the power saved by the *Double-Double* configuration is almost exactly the sum of that saved by the *Double-Single* and *Single-Double* configurations. This was true despite the stages being coupled via both precooling flows and interdependent recuperator sizes (recall that the total UA is fixed, so changes in one stage's UA affect that of the other), though it is important to bear in mind that both forms of coupling

may be underestimated by the present model due to the lack of axial conduction and radiation in the recuperators and also to the fairly high value of total UA used.

It is unsurprising that the change in compressor power is greater from doubling the 100 K (100 W) expander than from doubling the 25 K (20 W) expander, since the first-order cryocooler model in section 2.2.1 suggests that compressor power scales proportionally with $\dot{Q}_{\text{load}}/T_{\text{load}}$ (see equation (2.11)). At the given operating conditions, this would make the gain from doubling the 100 K expander 1.25 times greater than the gain from doubling the 25 K expander.

Doubling is more inherently beneficial in cold stages

In reality, the gain from doubling the 100 K expander was only 1.075 times greater than the gain from doubling the 25 K expander, considerably less than the factor of 1.25 predicted above. Since compressor power is closely related to mass flow rate, changes in mass flow rate in each stage can provide the hints necessary to understand this discrepancy; these changes are given in Table 2.4.

As the table shows, doubling only the 25 K expander decreases the mass flow rate of *both* stages. Doubling the 100 K expander on the other hand decreases the mass flow rate of the 100 K stage as expected, but increases the mass flow rate of the 25 K stage. These secondary effects seem to be responsible for the discrepancy, since the primary effects of doubling each expander are consistent with the expected ratio of 1.25:

$$\frac{-93.1 \text{ mg/s}}{-74.4 \text{ mg/s}} = 1.251. \tag{2.44}$$

The secondary effects are partly explained by the recuperator UA values shown in Table 2.2. Since a double-expander stage requires less mass flow, the optimizer shifts recuperator UA to the single-expander stage where it is needed more. As a result, doubling the 25 K expander increases the size of the 100 K recuperator, thus improving the performance of the 100 K stage. Doubling the 100 K expander similarly shifts UA to the 25 K recuperator, though it makes sense that the benefit would be smaller since the shift represents a smaller fraction of the 25 K recuperator (which is about twice as large as the 100 K recuperator).

Table 2.3: Changes in compressor power from using double expansion. All values are based on pure substance results and shown relative to the baseline configuration (for which $\dot{W}_{\text{comp}} = 2138$ W).

Configuration	Compressor power minus baseline [W]	Percent Change [%]
Double-Double	−415.6	−19.4
Double-Single	−216.4	−10.1
Single-Double	−201.4	−9.4
Single-Single	0.0	0.0

Table 2.4: Changes in mass flow rates into 100 K and 25 K stages from using double expansion. All values are based on pure substance results and shown relative to the baseline configuration.

	Mass flow rate minus baseline [mg/s]			
Configuration	100 K	25 K	Total	Percent Change [%]
Double-Double	−101.4	−72.1	−173.5	−19.4
Double-Single	−93.1	2.8	−90.3	−10.1
Single-Double	−9.7	−74.4	−84.1	−9.4
Single-Single	0.0	0.0	0.0	0.0

The shift in recuperator UA, however, cannot explain why doubling the 100 K expander *decreases* the performance of the 25 K stage. One possible explanation is visible from the precooling temperature in Table 2.2; since double expansion in the 100 K stage does not cool the fluid to as low a temperature as does a single high-pressure-ratio expansion, the precooling flow is provided to the 25 K recuperator at a warmer temperature (~70 K instead of ~56 K), which in turn leaves a higher fraction of that recuperator without a mass flow rate imbalance. While this hypothesis was not tested, the reasoning suggests that the benefits of double expansion are not fully realized in stages providing a precooling flow.

The mass flow rate of the precooling flow (Table 2.2) may also contribute to the secondary effects shown in Table 2.4. When double expansion is used in the 25 K stage, less precooling flow is needed to achieve the same amount of imbalance since the stage's mass flow rate is lower. Less precooling in turn reduces the detrimental flow imbalance in the 100 K stage, improving its performance.

Of course, even if double expansion has some drawbacks in the warmer stages of a cryocooler, it is important to consider its net effect on cryocooler efficiency when making design decisions. Despite the secondary effects, there was a larger net gain from double expansion in the 100 K stage of this cryocooler due to its larger $\dot{Q}_{\text{load}}/T_{\text{load}}$.

Precooling flows offer little benefit with no radiation/conduction

While precooling may be responsible for some of the behavior discussed above, it appears to be fairly unimportant in the present models. This is particularly clear from the results of the *No Precool* configuration, which performs only 2.5% worse than its counterpart with a precooling flow. Several factors contributed to this result, but the most important is probably the omission of radiation and axial conduction in the recuperator model. Addressing such heat leaks is an important role of precooling flows, and it stands to reason that neglecting them reduces precooling's apparent impact.

The unimportance of precooling also stems from the lack of variation in the specific heat capacity of helium at the temperatures and pressures used (visible from Figure 1-2 in Chapter 1). At the cold end of the 25 K recuperator in the *Single-Single* model,

the difference in specific heat capacity of the streams is only ~5%, and this drops to less than 1% by the precooling insertion point (~55 K).

Precooling did give most of the 25 K recuperator a constant $\Delta T/T$ as recommended by Minta (Figure 2-8), though again, its net effect on the cryocooler's efficiency was small.

Third stages offer little benefit with no radiation/conduction

The unimportance of precooling in the present model also explains the results of the three-stage simulations. In the *Pre-Single-Single* configuration, the optimizer set the precooling stage's mass flow rate and recuperator UA to their lower bounds, in effect removing the stage from the cryocooler and investing the UA in the 25 K and 100 K stages instead. Therefore, the efficiency was essentially the same as for the *Single-Single* configuration.

In the *Single-Pre-Single* configuration, the optimizer used a small but non-zero mass flow rate in the precooling stage, along with a recuperator UA of ~3 W/K. However, all of this mass flow[1] was directed to the 25 K stage as a precooling flow,

[1]A trivially small fraction (0.1%) was actually forced to return through the precooling stage's recuperator in order to maintain numerical stability, but this should not appreciably change the results.

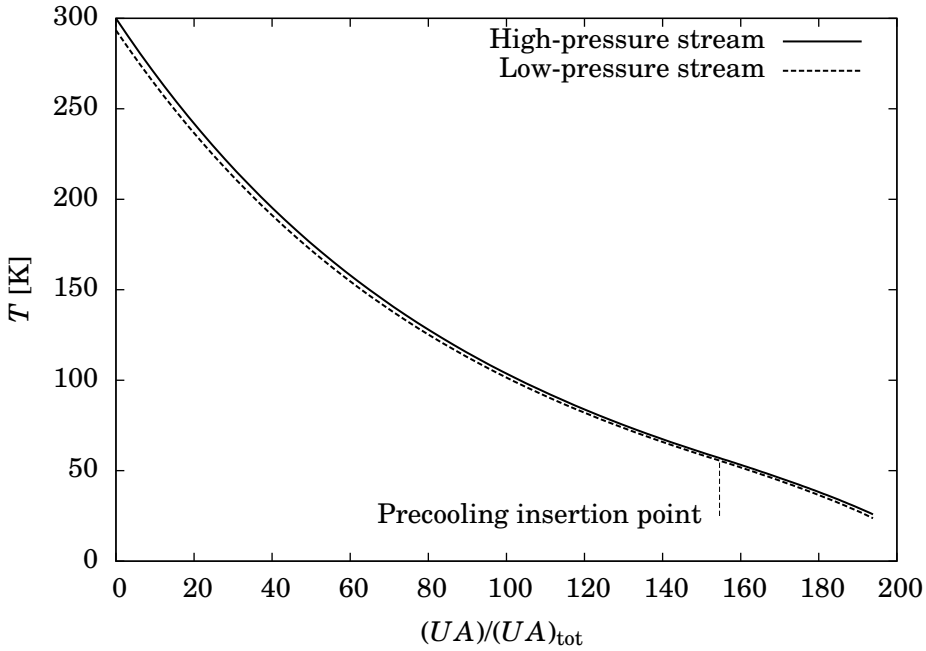

Figure 2-8: Computed fluid temperature profiles in the 25 K recuperator of the *Single-Single* cryocooler (pure substance model). The constant $\Delta T/T$ of about 2% is visible in the precooled section of the recuperator to the left of the insertion point, while the widening temperature difference due to the specific heat mismatch at low temperatures is visible toward the right.

effectively producing the configuration shown in Figure 2-9. This configuration had one slight advantage over the baseline *Single-Single* configuration: the precooling stage cooled fluid to a lower temperature, allowing it to be inserted closer to the cold end of the 25 K recuperator. The net result, however, was only a 0.1% increase in efficiency.

Again, the results above are skewed by the omission of radiation and axial conduction in the recuperator models. While they do suggest that a third stage is mostly superfluous when it comes to addressing variations in heat capacity at these temperatures, recuperator heat leaks must be addressed before concluding that the third stage is dispensable.

Non-ideal gas behavior has little overall effect

Finally, the simulated efficiencies of the ideal-gas-based models agreed well with those of the pure-substance-based models (within 1.5% in all cases). This is understandable since helium did not exhibit much non-ideal behavior in the cryocoolers studied.

2.4 Summary & Limitations

As demonstrated in this chapter, temperature mismatch is a significant source of inefficiency and should be considered in the design of any cryocooler with an external

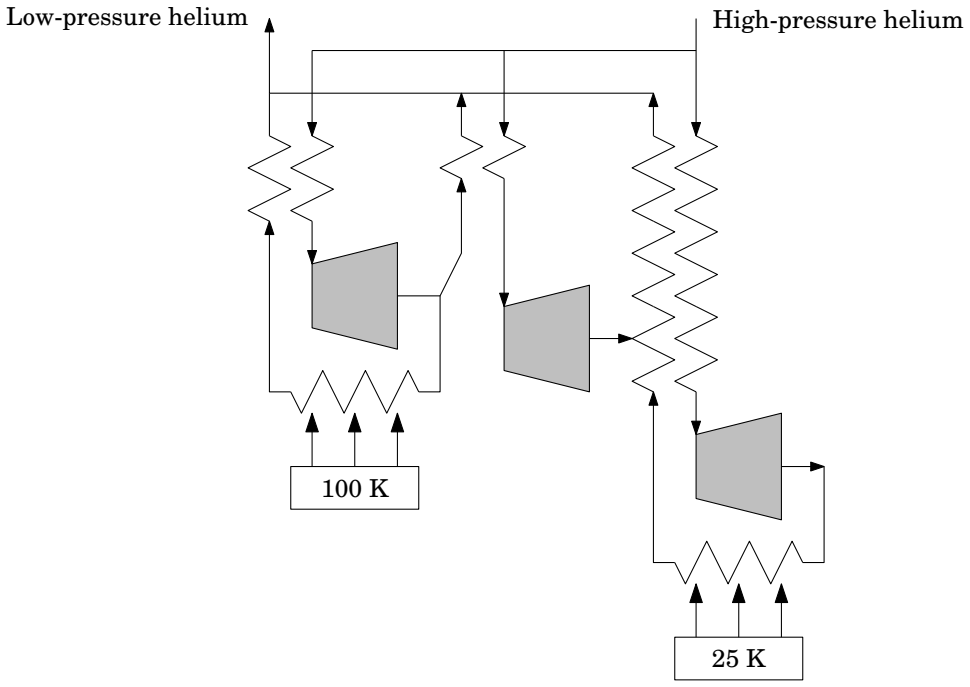

Figure 2-9: Configuration resulting from optimizing the *Single-Pre-Single* topology. The mass flow entering the precooling stage is used exclusively to precool the 25 K stage instead of returning through the precooling stage's recuperator.

flow loop. The magnitude of this loss (specifically, the fractional increase in compressor power compared to a system with infinite expanders) can be estimated using the simple heuristics introduced in section 2.2:

$$\textbf{Monatomic ideal gas:} \quad \frac{\dot{S}_{\text{gen}} T_{\text{load}}}{\dot{Q}_{\text{load}}} = \frac{1}{2} \frac{\log_{10}(\Pi)}{n},$$

$$\textbf{Arbitrary ideal gas:} \quad \frac{\dot{S}_{\text{gen}} T_{\text{load}}}{\dot{Q}_{\text{load}}} = \left(\frac{5R}{4c_P} \right) \frac{\log_{10}(\Pi)}{n}.$$

These heuristics are independent of the compressor efficiency and, if η_{exp} is identical for all expanders, of the expander efficiency as well.

Simulations show that the temperature mismatch loss is well mitigated by using double expansion in one or both stages. In a two-stage cryocooler, these benefits appear to be cumulative despite interactions between the stages; that is, if doubling the expander in the 100 K stage reduces the operating power by ~215 W and doing the same in the 25 K stage reduces the power by ~200 W, doubling the expanders in both stages reduces the power by ~415 W. Additionally, while double expansion is more *inherently* beneficial in the cold stage, the warm stage benefits more from double expansion in the NASA ZBO application since it must remove more entropy from the load. Regardless of the temperature, there are strongly-diminishing returns on efficiency for each additional expander, and it is likely unjustified to use more than two or three expanders per stage.

The simulations also shed some light on the effects of the precooling flows. These appeared to matter little in the present model: the predicted efficiency gain from precooling in a two-stage cryocooler was only 2.5%, and adding a third stage devoted exclusively to precooling only gained an additional 0.1%. If precooling were to have any actual benefit in these cryocoolers, therefore, it would not be from better heat capacity rate matching or a constant $\Delta T/T$ so much as from an improved handling of radiation and conduction heat leaks in the recuperators. The scope of this conclusion is quite narrow, though: in designs with either smaller recuperators (recall that UA was quite large in these models) or lower operating temperatures, optimizing the stream temperatures via precooling will become more important regardless of heat leaks.

The most complicated losses in the cryocooler, however, were hardly addressed in this chapter: abstracted away behind the simple expander model of section 2.3.1 is a complex expander system replete with thermal and mechanical design tradeoffs. Modeling the losses that drive these tradeoffs and examining how they affect the expander design is the focus of the next chapter.

"Invest your entropy in us. We'll make it grow!"

(Slogan on the Cryolab T-shirt)

Chapter 3

Parasitic Piston Expander Losses

3.1 Overview

Floating piston expanders (FPEs) have the potential to be efficient, robust, and flexible during operation, making them a good choice for modified Collins cryocooler designs; however, such expanders are not ideal, and a variety of parasitic loss mechanisms reduce their performance. Furthermore, individual losses tend to favor dissimilar expander designs, and existing literature on FPEs and similar piston-cylinder machines appears to contain limited information on their aggregate effects. This chapter therefore aims to provide an improved understanding of how key losses combine and interact to affect FPE performance, as well as to provide a basis for making well-informed expander design decisions.

Following some discussion of a simplified loss-less expander model, the various losses present in real FPEs are examined along with the relevant literature (which is bolstered by a newly-developed analysis of the losses associated with the appendix gap between the piston and its cylinder). Many of these losses were incorporated into a numerical expander model, which was then used to examine the influence of geometry and operating conditions on the efficiency of several expanders suitable for a ZBO cryocooler design. The results provide information about the design tradeoffs involved and demonstrate several interesting conclusions; among these, the realization that a design heuristic[1] previously used for FPEs can be improved upon and the notion that increased blow-in and blow-out can be *beneficial* to expander performance.

3.2 Reversible Expander Behavior

As in Chapter 2, examining a simplified version of a system can provide physical insights that may be obscured in a more complicated model. In the case of a floating

[1]This heuristic stated that the piston stroke length should be about the same as the expander diameter ($S \approx D$) and was based on minimizing cyclic heat transfer losses in the cold-end working volume; further details may be found on pages 71–75.

piston expander, it is also a good starting point for estimating the expander's cooling power as a function of geometry and operating conditions. A simple reversible expander model is therefore analyzed and discussed below before a more realistic model is presented in section 3.3.

3.2.1 Simplified Analysis

Ideally, a floating piston expander would have a perfectly adiabatic cold volume, execute perfectly reversible processes, and have no "dead volume" (that is, 100% of the cold-end working fluid would be exhausted each cycle). Such an idealized expander, illustrated in Figure 3-1 alongside the cycle it executes, forms the basis for this simplified analysis. This analysis will further assume that the working fluid can be modeled as an ideal gas.

There are only three processes in the simplified cycle: reversible isobaric mass intake at pressure P_{in} and temperature T_{in}, isentropic expansion from P_{in} to P_{out}, and reversible isobaric mass exhaust at P_{out} and T_{out}. The exhaust temperature may be found by rearranging the ideal gas entropy constitutive relation for the isentropic expansion process, to yield

$$T_{\text{out}} = T_{\text{in}} \left(\frac{P_{\text{out}}}{P_{\text{in}}} \right)^{R/c_P} . \tag{3.1}$$

The mass exhausted per stroke may in turn be found from the exhaust temperature and pressure along with the volume swept by the piston during the exhaust stroke (i.e., $V_{\text{swept}} = \frac{\pi}{4} D^2 S$). Using the ideal gas law,

$$m_{\text{out}} = \frac{P_{\text{out}} V_{\text{swept}}}{R T_{\text{out}}}. \tag{3.2}$$

Assuming the expander operates at a frequency of f cycles per second, the mass flow

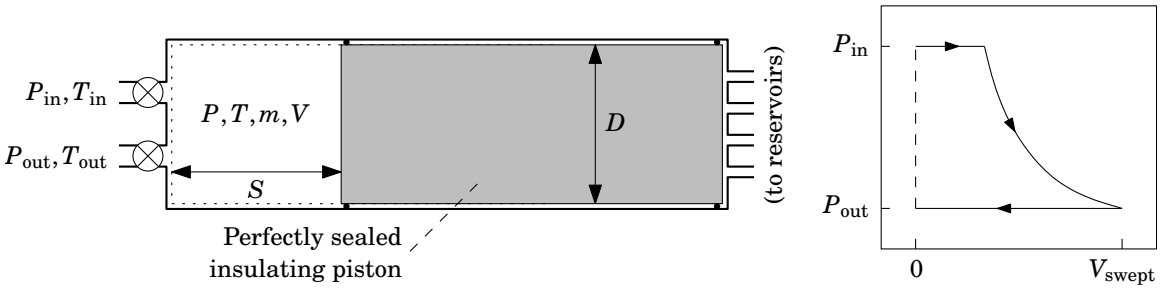

Figure 3-1: A simplified FPE model and its P-V diagram. This idealized expander has a perfectly adiabatic cold volume, contains no dead volume, and executes a cycle consisting of three reversible processes: an isobaric intake, an isentropic expansion, and an isobaric exhaust (which ends with zero mass in the working volume).

rate through the expander is therefore given by

$$\dot{m} = \frac{f P_{\text{out}} V_{\text{swept}}}{R T_{\text{out}}}. \tag{3.3}$$

The cooling power of the expander ($\dot{Q}_{\text{cool}}$) is defined as the rate at which energy is extracted from the working fluid. This may be found by multiplying the difference in specific enthalpy of the entering and exiting fluid streams by the expander's mass flow rate:

$$\dot{Q}_{\text{cool}} \equiv \dot{m} c_P (T_{\text{in}} - T_{\text{out}}). \tag{3.4}$$

Substituting $\dot{m}$ and T_{out} from equations (3.1) and (3.3) and simplifying,

$$\dot{Q}_{\text{cool}} = f P_{\text{out}} V_{\text{swept}} \left[\left(\frac{P_{\text{in}}}{P_{\text{out}}} \right)^{R/c_P} - 1 \right] \frac{c_P}{R}. \tag{3.5}$$

Most of equation (3.5) requires little explanation; the cooling power increases proportionally with the operating frequency, the swept volume of the expander, and the input pressure. Interestingly, the cooling power is independent of operating temperature. This makes sense for an ideal gas working fluid: while the temperature drop during expansion is smaller at lower temperatures, the fluid's density (and consequently the expander's mass flow rate) is proportionally higher. These two effects cancel out to yield the same cooling power for a given expander size.

The dependence of the expander's cooling power on output pressure and working fluid properties (c_P and R) is less clear from equation (3.5). In order to examine this dependence it is helpful to rearrange (3.5) as follows:

$$\frac{\dot{Q}_{\text{cool}} / V_{\text{swept}}}{f P_{\text{in}}} = \left(\frac{P_{\text{out}}}{P_{\text{in}}} \right) \left[\left(\frac{P_{\text{out}}}{P_{\text{in}}} \right)^{-R/c_P} - 1 \right] \frac{c_P}{R}. \tag{3.6}$$

Note that this is now a dimensionless cooling power per unit swept volume, expressed as a function of only a dimensionless output pressure ($P_{\text{out}}/P_{\text{in}}$) and a dimensionless fluid property ratio (R/c_P).

3.2.2 Results & Discussion

Equation (3.6) is plotted in Figure 3-2 for both monatomic and diatomic ideal-gas working fluids. For any given input pressure there is an optimum output pressure $P_{\text{out}} \approx 0.3 P_{\text{in}}$ which maximizes the cooling power per unit volume. Output pressures lower than $\sim 0.3 P_{\text{in}}$ further reduce the output temperature of the fluid, but also reduce its density enough to yield a net reduction in mass flow and cooling power. Output pressures higher than $\sim 0.3 P_{\text{in}}$ yield higher mass flow rates, but not enough so to compensate for the higher output temperatures.

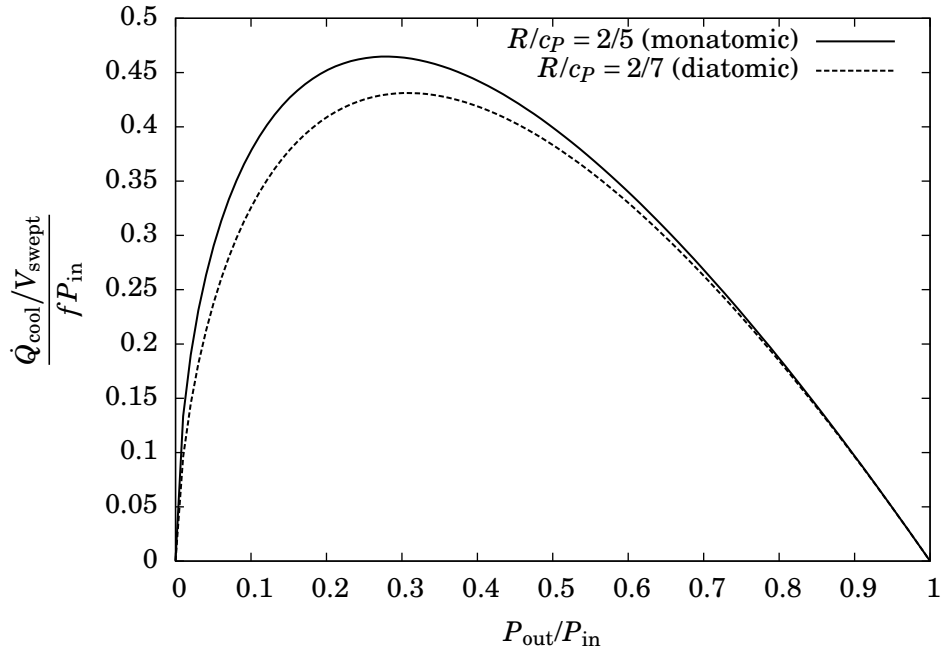

Figure 3-2: Dimensionless cooling power per unit volume as a function of dimensionless output pressure for a reversible FPE. Regardless of P_{in}, an output pressure of $P_{\text{out}} \approx 0.3P_{\text{in}}$ maximizes the cooling power ratio. Dimensionless output pressures higher than this decrease the total cooling by reducing the temperature drop of the fluid during expansion, while lower pressures decrease the cooling by reducing the mass flow rate of the expander.

Figure 3-2 also demonstrates that the optimum output pressure depends on working fluid properties, albeit only slightly. The dependence can be found analytically from (3.6):

$$\left.\frac{P_{\text{out}}}{P_{\text{in}}}\right|_{\text{opt}} = \left(1 - \frac{R}{c_P}\right)^{c_P/R}, \tag{3.7}$$

and, correspondingly,

$$\left.\frac{\dot{Q}_{\text{cool}}/V_{\text{swept}}}{fP_{\text{in}}}\right|_{\text{opt}} = \left(1 - \frac{R}{c_P}\right)^{c_P/R-1}. \tag{3.8}$$

For monatomic ideal gases (a suitable model for helium even at temperatures around 25 K) the optimum occurs at $P_{\text{out}}/P_{\text{in}} = 0.279$, which corresponds to an expander pressure ratio of 3.59.

Equations (3.7) and (3.8) are plotted in Figure 3-3. A second independent axis showing the heat capacity ratio c_P/c_V, equal to $(1-R/c_P)^{-1}$, is included in the plots for convenience. Figure 3-3a demonstrates that $P_{\text{out}} \approx 0.3P_{\text{in}}$ remains a useful heuristic across a range of working fluid properties. It should be emphasized, however, that the existence of an optimum pressure ratio does *not* imply that there is an optimum input pressure; a higher P_{in} always improves $\dot{Q}_{\text{cool}}$ in this analysis (see (3.5)), even if the output pressure remains fixed.

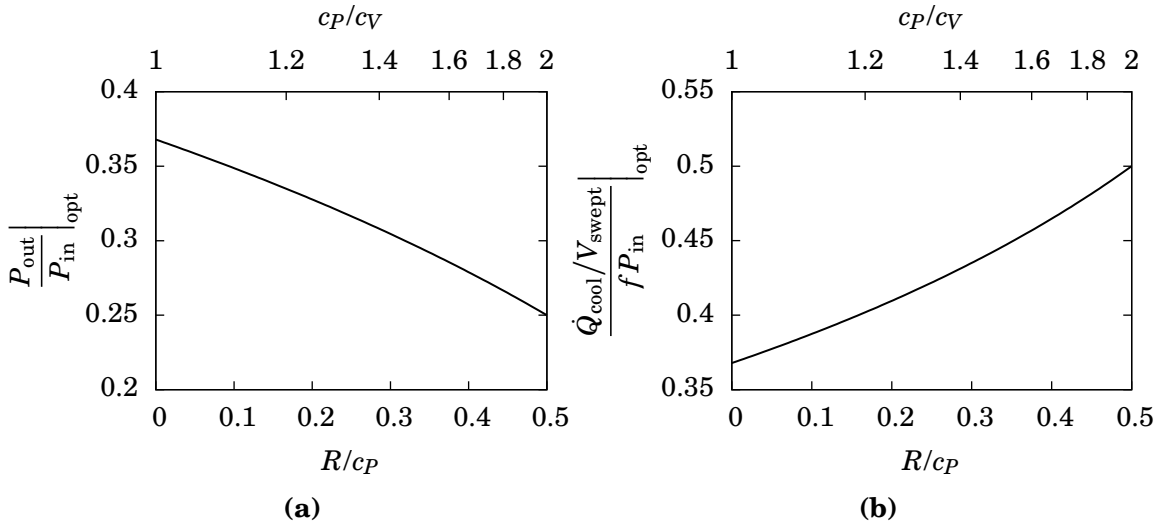

Figure 3-3: Variations of (a) optimum dimensionless low pressure and (b) optimum cooling power ratio as functions of working fluid properties. The optimum around $P_{\text{out}} \approx 0.3 P_{\text{in}}$ applies to a wide range of ideal-gas working fluids.

In addition to affecting the size of FPEs or other piston expanders, the results above also have implications for the losses in non-ideal expanders as many of those losses depend on the swept volume (via either D, S, or a combination of both). This introduces yet another factor in the selection of the cryocooler's pressure ratio and topology, in addition to recuperator design considerations which favor high pressure ratios (Chapter 1) and cooler-to-load temperature matching considerations which favor lower pressure ratios (Chapter 2).

3.3 Irreversible Expander Simulations

Actual expanders, of course, do not satisfy the assumptions of the simplified analysis above. The ideal model was adiabatic; actual expanders have heat transfers into the cold end that decrease the net cooling the expanders can provide. The ideal model was reversible; actual expanders have irreversibilities that reduce their efficiency. The ideal model assumed that all of the working fluid was exhausted from the expander each cycle; actual expanders have a dead volume that makes this impossible, requiring larger expanders with correspondingly greater losses. In order to accurately estimate expander performance, inform design choices, and understand how the losses interact and collectively affect the expander, a more detailed expander model is needed.

One common modeling approach in both the cryogenic and Stirling engine literature involves first computing the performance of a reversible device and then independently subtracting the effects of various losses (generally computed using simple analytical correlations or models). This requires the assumption that losses in the machine do not interact with each other, but has the advantage of yielding a largely

analytical model with a fast computation time. Additionally, such an analytical model is mathematically "smooth", making it easier to use in gradient-based optimization codes. The approach has been used at least as recently as 2011 to predict the effect of operating speed on Stirling engine power output [CY11], and is typically referred to as a "second order" approach in the Stirling literature. Typical second order approaches, however, do not lend themselves to modeling the interactions between fluid-wall heat transfer in the cold end, mixing irreversibilities during the intake process, and heat transfers in the narrow gap between the piston and cylinder (though admittedly, such interactions should matter less in high-efficiency expander designs as the losses themselves are small).

Another approach that is well suited to simulating loss interactions involves applying conservation laws for mass, energy, and sometimes momentum to a series of discrete control volumes, and then numerically integrating or solving the system of equations which results. Computational fluid dynamics (CFD) models fall into this category, as do the predominantly 1-D simulations referred to as "nodal analyses" in the literature; a good review of these approaches was presented by Dyson, Wilson, and Tew [DWT04]. In the present study, however, many control volumes would have been required to model transient heat transfers, especially along the piston length; the computation time was therefore expected to be too large to conduct wide-ranging multi-dimensional design studies with available computing hardware.

This section presents a new model that incorporates (albeit approximately) the interactions between several sources of expander inefficiency while remaining fast enough to explore a large number of designs. The approach is similar to that used by Wang [WS90]; analytical correlations are used to model transient heat transfers and fluid flow, but combined with numerical integration when necessary to solve non-linear differential equations or handle temperature-dependent material properties. A high-level overview of the approach is shown in Figure 3-4. The model is capable of identifying the cyclic steady state of the expander, including the steady-state temperature profile and mass flow rate amplitudes along the appendix gap.

The key physical features of the new expander model (along with their associated nomenclature) are illustrated in Figure 3-5. Of particular importance is the gap between the piston and cylinder, typically called the "appendix gap" in the literature; fluid flow and heat transfers in this gap play a significant role in the performance of the FPE. Also noteworthy are the clearance spaces at either end of the piston's stroke; while modeled as inaccessible regions of the cylinder for simplicity, the clearances in an actual expander would likely come from a combination of dead space in the valve mechanisms and deliberate safety margins in the control algorithm designed to avoid repeated impacts between the piston and cylinder.

The remainder of this section follows the structure outlined in Figure 3-4, beginning with descriptions and analyses of the various losses affecting floating piston expanders.

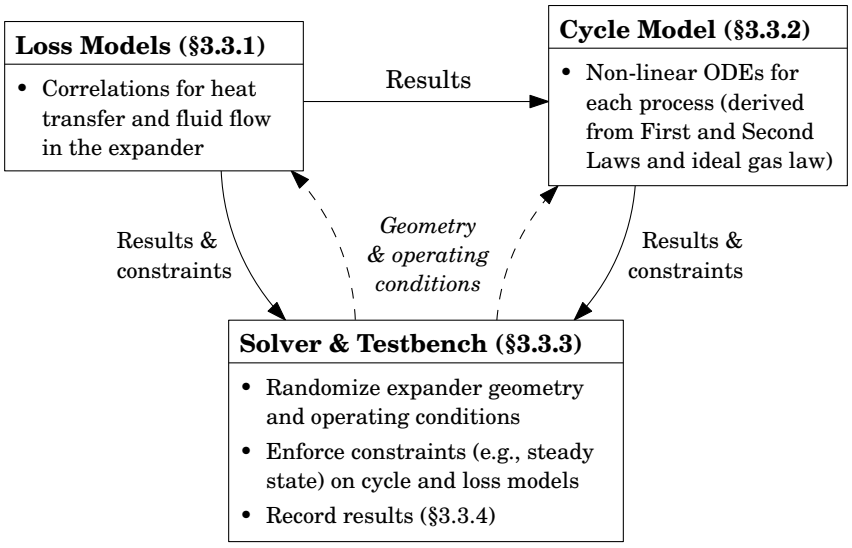

Figure 3-4: High-level overview of FPE modeling and solution approach.

3.3.1 Loss Descriptions & Models

At least eleven different loss mechanisms appear to affect the efficiency of either an FPE or the cryocooler in which it is used. Table 3.1 presents a summary of these losses, which are described individually in more detail below.

Conduction heat transfer

Perhaps the simplest loss affecting floating piston expanders is conduction heat transfer from the warm end to the cold end. This imposes an additional heat load on the cryocooler and reduces the amount of usable refrigeration. Two major conduction paths exist: the floating piston itself (typically a capped tube made of an insulating material like linen-filled phenolic), and the steel cylinder wall.

Conduction is governed by the thermal conductivity of the piston and cylinder, which in general is a function of temperature. Figure 3-6 shows the thermal conductivities of 304 stainless steel and G10, computed from correlations in NIST's online cryogenic material properties database [NIST]. G10 was used in the present model due to the lack of suitable correlations for linen-filled phenolic. For both materials the conductivity is reduced at lower temperatures, and varies by a factor of 3~5 over the range of 25–300 K.

The conduction heat transfer rate in either the piston or the cylinder can be computed from Fourier's law. Assuming 1-D axial heat transfer in a solid with temperature-dependent thermal conductivity $k(T)$, uniform cross-sectional area A_c, and a local axial temperature gradient dT/dx, Fourier's law simplifies to

$$\dot{Q}_{\text{cond}}(x) = k(T) A_c \frac{dT}{dx}, \tag{3.9}$$

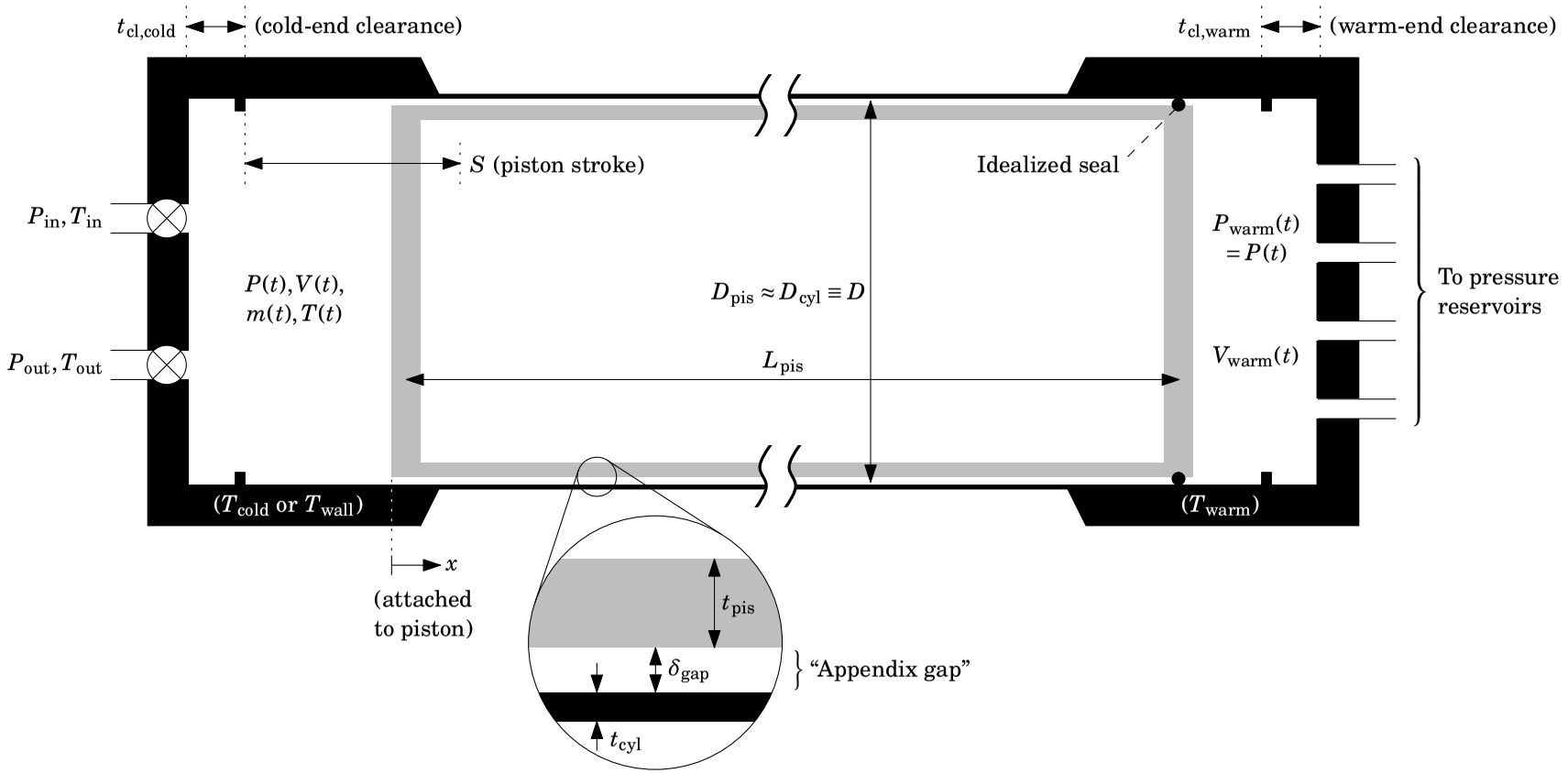

Figure 3-5: A more realistic FPE model showing key physical features and associated nomenclature. Unlike its idealized counterpart in Figure 3-1, this model includes clearance spaces at the warm and cold ends, a fluid-filled gap between the piston and cylinder, and non-negligible heat transfers between the solids and the working fluid as well as within the solids.

Table 3.1: Summary of loss mechanisms identified in floating piston expanders.

Loss mechanism	General area	Description
Conduction heat transfer	Appendix gap	Axial conduction heat transfer through the piston and cylinder from the warm end to the cold end (p. 55).
Shuttle heat transfer	Appendix gap	Thermal energy carried by reciprocating piston from the warm end to the cold end (p. 58).
Gas enthalpy transfer or "pumping loss"	Appendix gap	Enthalpy transport caused by pressure-driven flow into and out of the appendix gap (p. 61).
Cyclic heat transfer	Cold end	Irreversible cyclic heat transfer between working fluid and cold volume walls (p. 71).
Intake mixing	Cold end	Irreversible mixing between recompressed fluid in the cold volume and high-pressure fluid entering expander at T_{in} (p. 76).
Blow-in & blow-out	Cold end	Rapid, irreversible flow through intake/exhaust valves due to incomplete recompression or expansion (p. 76).
Valve losses*	Cold end	Irreversible flow due to pressure drop across cold-end valves during intake and exhaust (p. 77).
Appendix gap hysteresis*	Appendix gap	Net heat transfer from gas to piston and cylinder due to appendix gap irreversibilities (p. 77); conceptually similar to cyclic heat transfer above.
Piston blow-by*	Appendix gap	Mass and enthalpy flow past piston seal due to pressure differences between warm and cold end (p. 78).
Warm-end bleed loss*	Warm end	Increase in compressor power required to supply warm-end bleed flows, if used (p. 79).
Warm-end dissipation*	Warm end	Dissipation of work done by expanding cold fluid; occurs in warm-end valves, reservoirs, and working volume (p. 79).

* Not considered in the present expander model

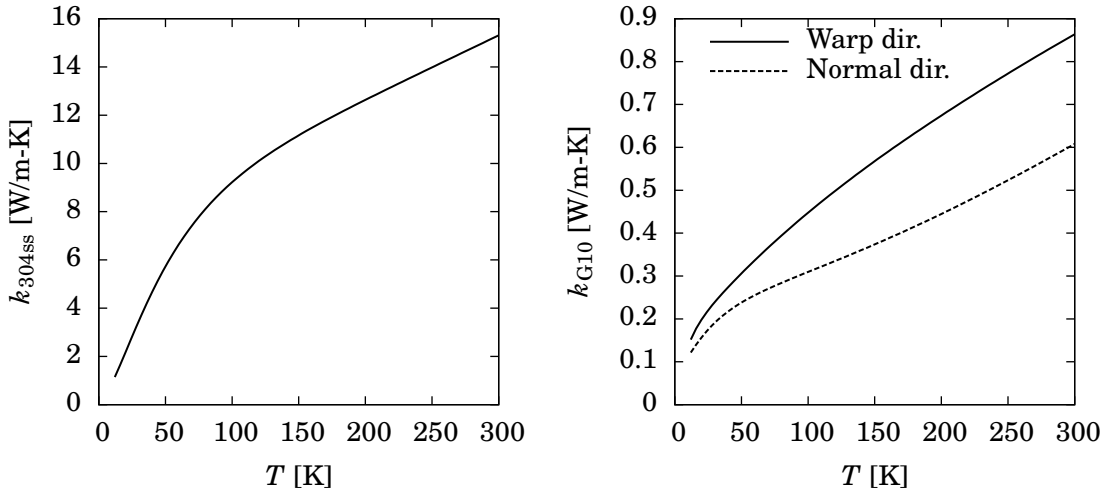

(a) 304 stainless steel **(b)** G10

Figure 3-6: Thermal conductivities of 304 stainless steel and G10 as functions of temperature. For both materials, thermal conductivity varies considerably over the temperature range expected in 25–100 K floating piston expanders.

where the sign convention of the heat transfer rate $\dot{Q}_{\text{cond}}(x)$ has been intentionally flipped so that conduction is positive *toward* the cold end (i.e., opposite the x direction).

Assuming the temperature gradient is approximately the same in the piston and cylinder at a given location, the total conduction heat transfer rate is simply the sum of the heat transfer rate in the piston and that in the cylinder. Approximating the cross-sectional areas of the piston and cylinder as the product of their circumference πD and thicknesses t_{pis} and t_{cyl}, substituting, and simplifying,

$$\dot{Q}_{\text{cond}}(x) = \pi D\Big(t_{\text{pis}} k_{\text{pis},x}(T) + t_{\text{cyl}} k_{\text{cyl},x}(T)\Big)\frac{dT}{dx}, \tag{3.10}$$

where $k_{\text{pis},x}(T)$ and $k_{\text{cyl},x}(T)$ are the axial-direction thermal conductivities of the piston and cylinder material, respectively. Note that $\dot{Q}_{\text{cond}}(x)$ is in general a function of position due to the additional heat transfers present in the appendix gap (discussed below).

Conduction heat transfer may be reduced by using smaller expander diameters and thinner piston and cylinder walls to decrease the heat transfer area, as well as by using materials with lower thermal conductivities. The loss should also decrease with longer expanders and smaller warm-to-cold-end temperature differences as both reduce the temperature gradients driving the heat transfer.

Shuttle heat transfer

In addition to serving as a conduction path, the piston in an FPE physically carries thermal energy from the warm end to the cold end as it reciprocates. When the piston

is near the warm end of its stroke, it receives a heat transfer from the locally-warmer cylinder wall (Figure 3-7a); when the piston has moved to the cold end, the heat picked up earlier is transferred back to the cylinder wall at a lower temperature (Figure 3-7b). In this manner, the piston "shuttles" heat down the expander, and so this mechanism is typically referred to as shuttle heat transfer in the literature.

The shuttle heat transfer mechanism has been know at least as far back as 1959, when McMahon and Gifford referred to "motional heat transfer" in their description of what is now the Gifford-McMahon refrigerator [MG60]. The loss appears to have been analyzed approximately by Gifford in 1966 [Gif66] and by Magee and Doering in 1968 [MD68]; both are Air Force Flight Dynamics Laboratory technical reports and could not be located at the time of this writing, though the final expression from Gifford's analysis was reproduced (without derivation) in the open literature a few years later [AG71]. Ríos also presented a shuttle heat transfer derivation in a 1969 MIT doctoral thesis, using what have come to be standard assumptions in the literature: a linear temperature profile along the expander with negligible end effects, transient radial conduction in the piston, sinusoidal piston motion, and a constant heat transfer coefficient from radial conduction through the fluid in the appendix gap [Río69].

The first analysis of shuttle heat transfer in the open literature was presented by Zimmerman and Longsworth in 1971 and included both an analytical expression based on mean property values and a finite-difference computer simulation which accounted for temperature-dependent properties. This analysis assumed that the thermal capacities of the piston and cylinder were infinite instead of considering

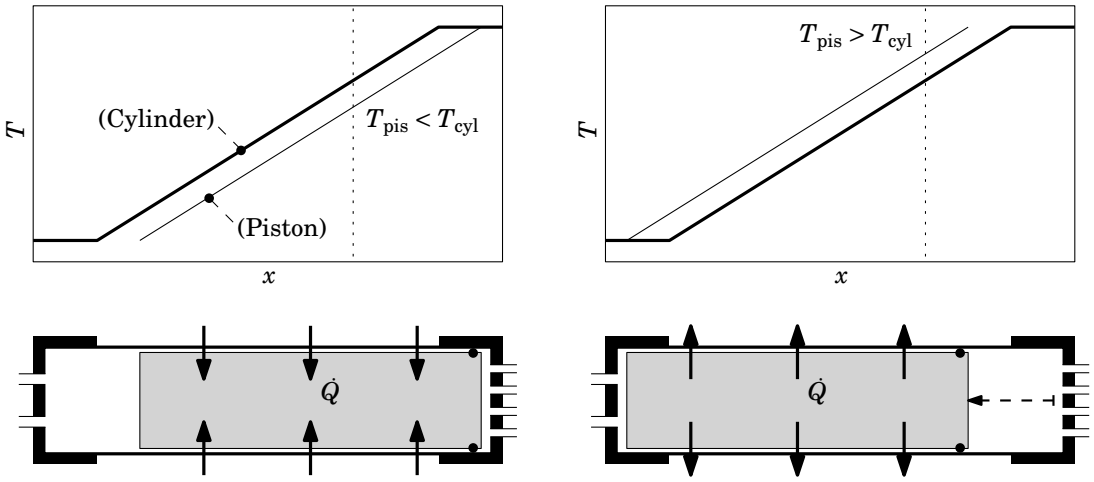

(a) Heat transferred from piston to cylinder **(b)** Heat redeposited nearer to cold end

Figure 3-7: Simplified illustration of shuttle (motional) heat transfer. (a) When the piston is near the warm end, it's temperature is everywhere colder than the cylinder; heat is therefore transferred through the thin gap into the piston. (b) The piston moves nearer to the cold end before the heat is transferred back into the cylinder. In this way, the piston "shuttles" heat from the warm end to the cold end.

transient conduction [ZL71]. Shortly thereafter, Ríos presented a revised version of the analysis in his thesis which permitted transient conduction in the cylinder as well as the piston, approximated the effects of mass flow in the appendix gap and non-linear expander temperature profiles, explored the effects of both thick- and thin-walled pistons and cylinders, and in the general case, supported non-sinusoidal piston motion [Río71]. This analysis still remains one of the most thorough in the literature.

Numerous studies were published in the decades after Ríos's paper, though not all will be enumerated here. A highlight of the literature was presented by Chang and Baik in 1996; this included an expression which, while algebraically identical to a special case of Ríos's 1971 result, was presented and discussed in a convenient and physically relevant form [CB96]. Chang, Park, and Jeong later examined the effects of visco-inertial fluid flow in the gap driven solely by piston motion; their results demonstrate that such flow can significantly affect the heat transfer at higher frequencies [CPJ00]. An analysis including the effects of fluid motion was also published by Kotsubo and Swift, who applied thermoacoustic formalism to produce a very general solution for the local fluid flow and heat transfers in the displacer gap of a Stirling cryocooler [KS06]; this analysis is certainly the most general of its type, including the effects of local pressure fluctuations, multi-layered piston or cylinder walls, first-order real gas effects, and both inertial and bulk fluid flow (though the most general forms do appear to require a numerical integration step).

With the introduction of fluid flow into several of the analyses above, it can be difficult to provide a definitive separation between shuttle heat transfer and another loss known as gas enthalpy transfer (discussed in the following section). One common approach is to refer to the net enthalpy flow in the *solids* as shuttle and the net enthalpy flow in the *fluid* as gas enthalpy transfer; it turns out, however, that such an approach yields a different categorization of the losses depending on the reference frame in which the analysis is performed. To avoid siding with one reference frame over another, this thesis will take the approach of using "shuttle" to refer exclusively to the mechanism described in Figure 3-7 (i.e., without any pressure and mass flow effects) and will reserve "gas enthalpy transfer" for the remaining enthalpy transport arising from fluid motion in the gap, regardless of whether such transport occurs in the fluid or in the wall at a given point in the cycle. Such a definition, while unconventional, is entirely reference-frame independent.

Chang and Baik's expression for shuttle heat transfer (which does not include any fluid flow effects) is reproduced below with some minor algebraic and nomenclature changes:

$$\dot{Q}_{\text{shuttle}} = \left(\frac{T_{\text{warm}} - T_{\text{cold}}}{L}\right) \frac{\pi D S^2 k_{\text{gap}}}{8\delta_{\text{gap}}} \frac{b_{\text{pis}} + b_{\text{cyl}} + 1}{\left(b_{\text{pis}} + b_{\text{cyl}}\right)^2 + \left(b_{\text{pis}} + b_{\text{cyl}} + 1\right)^2}, \tag{3.11}$$

where S is the stroke length of the piston, k_{gap} is the thermal conductivity of the fluid in the appendix gap, and δ_{gap} is the width of the appendix gap. The new quantities b_{pis} and b_{cyl} are Biot numbers for the piston and cylinder with characteristic lengths

given by the thermal penetration depth into the solids; these are in turn dependent on the solids' radial-direction thermal conductivities ($k_{\text{pis},r}$ and $k_{\text{cyl},r}$) and thermal diffusivities ($\alpha_{\text{pis},r}$ and $\alpha_{\text{cyl},r}$) as well as on the expander's angular frequency of operation $\omega \equiv 2\pi f$:

$$b_{\text{pis}} \equiv \frac{\left(k_{\text{gap}}/\delta_{\text{gap}}\right)}{k_{\text{pis},r}}\sqrt{\frac{\alpha_{\text{pis},r}}{2\omega}}, \qquad b_{\text{cyl}} \equiv \frac{\left(k_{\text{gap}}/\delta_{\text{gap}}\right)}{k_{\text{cyl},r}}\sqrt{\frac{\alpha_{\text{cyl},r}}{2\omega}}. \tag{3.12}$$

Like conduction, shuttle heat transfer scales with diameter, but favors short stroke lengths due to its dependence on S^2. Shuttle is also proportional to the temperature gradient, which Chang and Baik assumed to be linear. The remaining variables (gap width, fluid thermal conductivity, material properties, and frequency) appear inside the Biot numbers b_{pis} and b_{cyl} and their behavior is therefore less apparent from equation (3.11). If the Biot numbers are small such that heat transfer is limited by the resistance of the fluid (a "wide" gap), shuttle is most strongly mitigated by a wider gap and a less-conductive fluid. If the Biot numbers are large such that heat transfer is limited by transient conduction in the solids (a "narrow" gap), the shuttle is most strongly mitigated by lower operating frequencies and lower solid thermal conductivities, densities, and heat capacities. For a 1 Hz expander with a helium working fluid, a 304 stainless steel cylinder, and a G10 piston, the crossover between these two regimes occurs at gap widths ranging from 0.04 mm (~0.002 inches) at 300 K to 0.1 mm (~0.005 inches) at 10 K. Chang and Baik illustrate these trends in more detail and provide limiting-case expressions [CB96].

Gas enthalpy transfer and combined gap losses

The discussion of shuttle above suggests that the appendix gap should be widened to decrease the thermal communication between the piston and cylinder. However, another loss known as gas enthalpy transfer (often called "pumping loss" in the literature, though the same term is also used for unrelated phenomena) becomes increasingly important at larger gap sizes. As the pressure in the cold-end fluctuates, fluid is forced in and out of the appendix gap, where it undergoes heat transfers with the gap walls and ultimately contributes a net enthalpy flow into the cold end. The resulting tradeoff between shuttle and gas enthalpy transfer (GET) typically leads to a minimum loss at an intermediate gap size.

A wide appendix gap also has other detrimental effects. Fluid leaving the gap is rarely at the temperature of the cold-end working fluid, resulting in irreversible mixing. In adiabatic expanders, fluid similarly enters the gap at a different temperature than the gap walls, leading to irreversible heat transfers. Additionally, by adding to the dead volume of the expander, large appendix gaps increase the length of the recompression stroke required to bring the cold-end up to the desired high pressure; this increased stroke can in turn increase the amount of shuttle, as well as provide more surface area for irreversible cyclic heat transfers in the cold end.

In order to illustrate some of the characteristics of GET, the gap model developed later in this section was exercised to produce data for a representative 25 K expander; the data is summarized in Figures 3-8 and 3-9. The first of these typifies the shuttle/GET tradeoff discussed above; as the gap width grows larger, the average prevalence of shuttle decreases and that of GET increases, yielding a minimum total loss at an intermediate value of δ_{gap}. However, these curves also belie the complexity of the gas enthalpy transfer loss, which varies strongly with position in the gap (Figure 3-9a) and can significantly affect the expander's temperature profile (Figure 3-9b). In effect, since reciprocating fluid in the gap receives its energy from the piston and cylinder walls, gas enthalpy transfer allows some of the shuttle and conduction heat transfers from the warm end to bypass part of the expander's length.

The body of literature on gas enthalpy transfer seems considerably less mature than that of shuttle heat transfer; several investigations of the mechanism exits, but these differ considerably in their approaches and results. Ríos seems to have introduced the first model of this loss in his 1969 doctoral dissertation; he treated gas enthalpy transfer independently from shuttle, computed a mass flow rate assuming a uniform sinusoidally-varying pressure in the gap, and assumed that the fluid enters and exits the gap at a temperature mid-way between the cylinder and displacer temperatures (this temperature varies as the displacer moves due to its

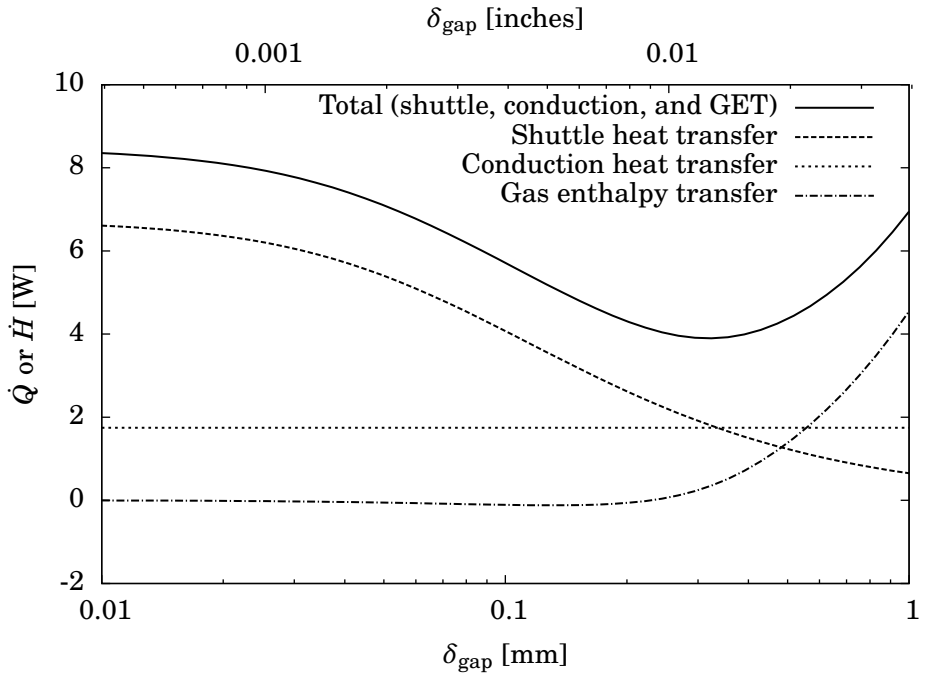

Figure 3-8: Breakdown of appendix gap heat transfers as a function of gap width in a representative 25 K FPE (averaged along expander length). Shuttle heat transfers dominate the total loss for narrow gaps, while gas enthalpy transfers dominate for wider gaps; this yields a clear minimum in the total loss at intermediate gap sizes. (Data are for a 1 Hz expander with T_{cold} = 25 K, T_{warm} = 300 K, P_{in} = 1.0 MPa, P_{out} = 0.1 MPa, D = 8 cm, S = 2 cm, L = 0.5 m, t_{pis} = 3 mm of G10, and t_{cyl} = 1 mm of 304 stainless steel.)

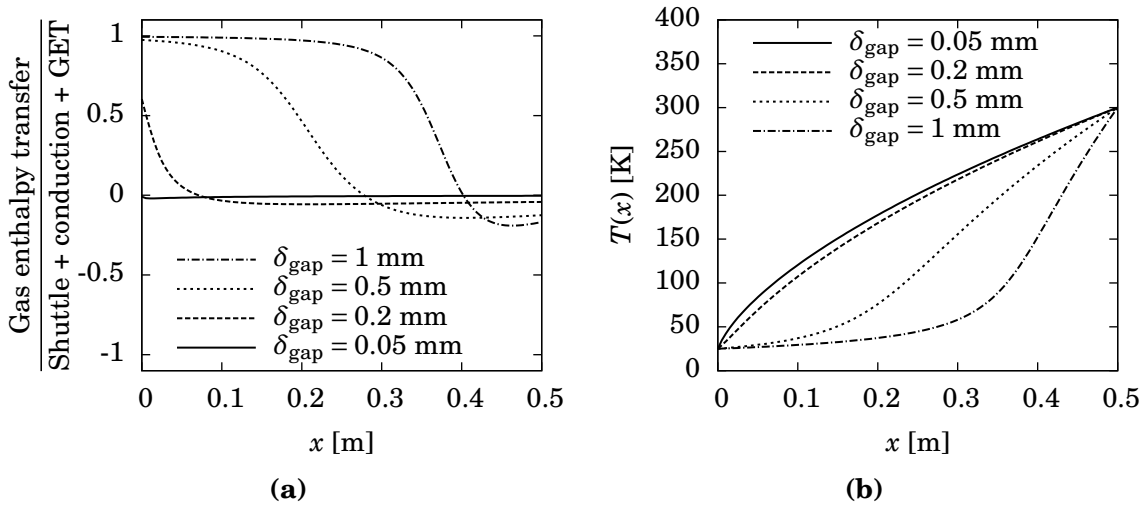

Figure 3-9: (a) Normalized gas enthalpy transfer distribution and (b) expander temperature profile as functions of gap width for the expander in Figure 3-8. For very small gaps, the temperature profile is dominated by shuttle and conduction and gas enthalpy transfer is practically nonexistent. As the gap is widened, the effect of gas enthalpy transfer penetrates increasingly further into the gap, isothermalizing the cold end and steepening the temperature gradient near the warm end. Note that in this example the gas enthalpy transfer actually reverses sign near the warm end.

axial temperature gradient) [Río69]. The next year Leo presented a correlation for gas enthalpy transfer in an Air Force Flight Dynamics Laboratory design handbook for Vuilleumier cryocoolers [Leo70]; a copy of the handbook could not be located to examine the details, but the correlation is reproduced by Martini [Mar83].

Leo's work was followed by an updated analysis from Ríos which uses Fourier series to determine the combined effect of shuttle and gas enthalpy transfer [Río71]. In addition to addressing the losses simultaneously as a function of local temperature gradient, Ríos proposed an interesting way to estimate the non-linear axial temperature profiles cause by mass flow rate gradients along the gap (which he assumed sealed at the warm end and open at the cold end). In this method, the axial temperature profile of the expander was assumed to be parabolic with one unknown constant; the shuttle and gas enthalpy transfers were then computed at both ends in terms of this constant, and the First Law was enforced around the appendix gap allowing the constant to be solved analytically. As with his analysis of shuttle, Ríos's treatment of gas enthalpy transfer remains one of the most thorough in the open literature.

Gas enthalpy transfer was further explored by Berchowitz and Berggren in 1981 as part of the Automotive Stirling Engine Development Project [BB81]; while a copy of this report could not be located despite repeated attempts, a more recent version of the analysis was obtained via personal correspondence with Berchowitz [Ber02]. The analysis follows that of Ríos, but with different assumptions and simplifications; notably, Berchowitz's treatment of the problem, which is presumably focused on Stirling engines and heat pumps, includes the effects of inertia on appendix gap fluid

flow but justifies neglecting pressure-driven flows by means of an order-of-magnitude analysis.

A much-simplified version of Berchowitz and Berggren's 1981 analysis was published by Urieli and Berchowitz in their 1984 Stirling analysis text [UB84]. The simplified version first solves the pure shuttle problem assuming no pressure-driven flow in the gap (only a linear Couette flow due to displacer motion), then uses the resulting periodic gas temperature at the open end of the gap along with a pressure-driven mass flow to compute a net gas enthalpy transfer. The mass flow itself was computed by assuming a linear axial temperature profile along the displacer along with uniform pressure and locally-isothermal compression and expansion of the gas. This analysis demonstrates a clear minimum in the combined shuttle and pumping loss as expected. Berchowitz presented this analysis in his doctoral thesis with one substantial modification: the periodic gas temperature is only used for flow exiting the gap, while flow is assumed to enter the gap at the time-averaged mean temperature of the working volume [Ber86].

West also presented a simple treatment of the gas enthalpy transfer by assuming that flows occur at the average of the local displacer and cylinder temperatures (without regards to the flow direction), though he did not include transient conduction in the solids and instead assumed that local temperature variations are due solely to displacer motion [Wes86]. Like Urieli and Berchowitz, he computed the mass flow in and out of the gap assuming a uniform time-varying pressure, a linear displacer temperature profile, and locally-isothermal compression and expansion. Finally, the study by Kotsubo and Swift (described earlier in the review of shuttle heat transfer literature) presents a very detailed treatment of the local fluid and heat transfer behavior in the gap by applying the techniques of thermoacoustic analysis [KS06].

Several other analytical treatments exist as subsets of broader studies on cyclic heat transfer in oscillating working volumes, though these are similar to those already mentioned [Cha88, Jeo91, JS92]. A small handful of numerical studies focused specifically on the appendix gap are also available; the most recent appears to be a numerical Stirling engine study by Andersen, Carlsen, and Thomson which discretizes the gas and walls in the axial direction but does not consider radial temperature gradients in the solids [ACT05]. The net loss predicted by Andersen et al. has a local minimum at intermediate gap sizes as expected, but also decreases for wider gaps as a result of poor gas-wall heat transfer.

One shortcoming of the approaches above is that they do not provide a method for computing mass flows in the case of non-linear gap temperature profiles[2]. This problem is non-trivial: the axial temperature profile affects the amount of mass in the gap and in turn the mass flow, but the mass flow imposes significant heat transfers which in turn affect the temperature profile. The potential for partial sealing and non-uniform pressures in thin gaps further complicates matters. For the present thesis, a new analysis of shuttle and gas enthalpy transfer losses was therefore carried out

[2]While Ríos's method may be used to estimate the effect of known mass flows on the temperature profile, it does not provide a way to compute the mass flows themselves.

which includes such effects in a way compatible with the expander model presented later in this chapter.

Following the examples of others in the field, a number of simplifying assumptions were first made:

1. End effects are negligible.
2. Velocities, temperatures, and pressures all vary sinusoidally.
3. The axial temperature gradient is locally linear over a distance of one stroke length and is identical in the piston, cylinder, and fluid.
4. Material and fluid properties are uniform over a distance of one stroke length.
5. Material and fluid properties at a given axial position are constant at their time-averaged mean values (including fluid density).
6. The penetration depth of heat transfer into the piston and cylinder walls is much smaller than the wall thicknesses and expander diameter; both walls may therefore be modeled as semi-infinite solids with negligible curvature.
7. The gap width is much smaller than the expander diameter such that curvature effects may be neglected.
8. The gap is of uniform width and is perfectly sealed at the warm end (e.g., by means of an O-ring or ideal clearance seal).
9. In the First Law for fluid in the gap, viscous dissipation and pressure gradients are negligible compared to other terms.
10. Fluid flow is laminar, hydrodynamically fully developed, and thermally fully developed.
11. The gap mass flow rate and pressure fluctuations were both assumed to have a uniform phase angle throughout the gap.
12. Pressure-driven Poiseuille flow dominates in the gap; Couette flow due to piston motion is small in comparison.

Most of these are similar to those in the literature, with the exception of the Poiseuille-flow-only assumption (number 12 in the list above).

The first part of the analysis focuses on modeling the fluid-flow behavior in the gap. Conservation of mass is addressed first; for a differential slice of the gap with width dx in the axial direction,

$$\dot{m}(x,t) - \dot{m}(x+dx,t) = \frac{\partial}{\partial t} dm(x,t). \tag{3.13}$$

Substituting for dm using the ideal gas law and taking the limit as dx approaches zero yields an equation relating the mass flow rate gradient to the local rate of change of pressure:

$$\frac{\partial \dot{m}(x,t)}{\partial x} = \left(\frac{\pi D \delta_{\text{gap}}}{RT(x)}\right)\frac{\partial P(x,t)}{\partial t}. \tag{3.14}$$

When the flow is laminar and fully developed, the local pressure gradient may be related to the mass flow rate using the solution for Poiseuille flow between infinite parallel plates and rewriting the mean flow velocity $\overline{U}$ in terms of $\dot{m}$ and other variables:

$$\frac{\partial P(x,t)}{\partial x} = \frac{-12\mu(T)}{\delta_{\text{gap}}^2}\overline{U}(x,t) = \left(\frac{-12\mu(T)RT(x)}{\pi D \delta_{\text{gap}}^3 P(x,t)}\right)\dot{m}(x,t), \tag{3.15}$$

where $\mu(T)$ is the temperature-dependent viscosity of the fluid. Note that the fluid's density (required to relate $\overline{U}$ and $\dot{m}$) has been written using its ideal gas law equivalent, $P(x,t)/\big(RT(x)\big)$.

Equations (3.14) and (3.15) form a set of non-linear coupled partial differential equations. The $P(x,t)$ term in the denominator of equation (3.15) proves particularly troublesome as it makes the equations non-linear in t as well as in x. To make the equations more tractable, this pressure term was replaced with a time-invariant mean of the expander pressure $\overline{P} \equiv \sqrt{P_{\text{in}} \cdot P_{\text{out}}}$; physically, such a substitution is equivalent to ignoring the effect of cyclic density variations on the flow. A geometric mean was chosen with the intent of yielding a similar percent error between $\overline{P}$ and each of the extreme pressures.

The partial differential equations above may be simplified by introducing the following candidate solutions for the local mass flow rate and pressure:

$$\dot{m}(x,t) \equiv \text{Re}\left\{\dot{m}_1(x)e^{i\omega t}\right\}, \tag{3.16}$$

$$P(x,t) \equiv \text{Re}\left\{P_1(x)e^{i\omega t}\right\} + P_0, \tag{3.17}$$

where "Re" is the real-part operator, $P_1(x)$ and $\dot{m}_1(x)$ are the complex amplitudes of the pressure and mass flow rate at different positions in the gap, i is equal to $\sqrt{-1}$, and $P_0 \equiv \frac{1}{2}(P_{\text{in}} + P_{\text{out}})$ is the pressure's arithmetic mean or "DC offset" which is assumed uniform throughout the gap (note that this is not equal to $\overline{P}$ above). Substituting these candidate solutions into (3.14) and (3.15) and omitting the real operators[3] transforms

[3]This works because solutions to a complex-valued equation $A = B$ (with $A, B \in \mathbb{Z}$) also satisfy its real-valued counterpart $\text{Re}\{A\} = \text{Re}\{B\}$. Equations including *products* of periodic terms (such as the First Law) require slightly more care, but are easily transformed into the form above by means of a complex identity (Appendix A.2).

the partial differential equations into ordinary differential equations in x:

$$\frac{d\dot{m}_1(x)}{dx} = \left(\frac{-i\omega\pi D\delta_{\text{gap}}}{RT(x)}\right)P_1(x), \tag{3.18}$$

$$\frac{dP_1(x)}{dx} = \left(\frac{-12RT(x)\mu(T)}{\pi D\delta_{\text{gap}}^3\overline{P}}\right)\dot{m}_1(x). \tag{3.19}$$

Note that both (3.18) and (3.19) depend on the local temperature which is itself a function of position.

The gap mass flow rate and pressure fluctuations were eventually (and somewhat regrettably) assumed to have a uniform phase angle throughout the gap, with the mass flow rate in phase with the rate of change of pressure. In reality, these phase angles would vary along the gap's length when the gap offers significant flow resistance; however, the gap is typically small enough in this case that shuttle heat transfer dominates over the effects of mass flow and pressure variations. A more recent attempt to include phase angle variations suggest that the error from this assumption is below 8.5% for ~99.9% of the simulations conducted later in this chapter, with most of the errors falling below 1%.[4] Making the uniform-phase assumption yields the following modified forms of the above ODEs:

$$\frac{d|\dot{m}_1(x)|}{dx} = \left(\frac{-\omega\pi D\delta_{\text{gap}}}{RT(x)}\right)|P_1(x)|, \tag{3.20}$$

$$\frac{d|P_1(x)|}{dx} = \left(\frac{-12RT(x)\mu(T)}{\pi D\delta_{\text{gap}}^3\overline{P}}\right)|\dot{m}_1(x)|. \tag{3.21}$$

The remainder of the analysis process is similar to that above: periodic variables such as velocity and temperature were represented as the real part of complex exponentials and substituted into appropriate versions of the First Law for the fluid and the walls. Under the assumptions above, this substitution transforms the PDEs describing temperature as a function of time and radial position into ODEs, enabling a closed-form analytical solution to the shuttle and gas enthalpy transfers at any axial position x along the gap (assuming the temperature, mass flow rate amplitude, and pressure amplitude are known at that point); further details of the process are

[4]The new analysis follows the procedure described in Appendix A.3 but introduces an additional phase angle for the bulk fluid velocity, yielding several extra terms in the solution. To estimate the error, the new and old appendix gap models were both run on a 1% subset (10,461 valid simulations) of the "fpe_exploration_NASA5" data described later in this chapter, and the total gap heat transfers were compared with the new model used as the baseline. The 1% subset was chosen randomly; while a potential for experimental bias exists since 493 simulations did not converge and could not be included in the results, the ones that did converge seem to cover a wide swath of the design space and are hopefully representative of the larger dataset.

described in Appendix A.3. The final result is

$$\begin{aligned}\dot{Q}_{\text{shuttle}}(x)+\dot{H}_{\text{GET}}(x) = {} & \frac{dT}{dx}\frac{\pi D S^2 k_{\text{gap}}}{8\delta_{\text{gap}}}\left(\frac{b_{\text{pis}}+b_{\text{cyl}}+1}{\beta}\right) \\ & + \frac{dT}{dx}\frac{|\dot{m}_1|\,c_P S}{4}\left(\frac{(b_{\text{cyl}}-b_{\text{pis}})\cos\phi}{\beta}\right) \\ & + \frac{\omega|P_1|\pi D S\delta_{\text{gap}}}{8}\left(\frac{(b_{\text{pis}}-b_{\text{cyl}})\cos\phi+\left[4b_{\text{cyl}}\left(b_{\text{pis}}+b_{\text{cyl}}+\frac{3}{4}\right)+b_{\text{pis}}+1\right]\sin\phi}{\beta}\right) \\ & + \frac{dT}{dx}\frac{(|\dot{m}_1|\,c_P)^2\delta_{\text{gap}}}{4\pi D k_{\text{gap}}}\left(\frac{(b_{\text{pis}}+b_{\text{cyl}})\left[\left(2b_{\text{pis}}+1\right)\left(2b_{\text{cyl}}+1\right)+\frac{1}{2}\right]+\frac{1}{2}}{\beta}-\frac{9}{35}\right) \\ & - \frac{\omega|P_1\dot{m}_1|\,c_P\delta_{\text{gap}}^2}{4k_{\text{gap}}}\left(\frac{(b_{\text{pis}}+b_{\text{cyl}})\left[\left(2b_{\text{pis}}+1\right)\left(2b_{\text{cyl}}+1\right)+\frac{1}{2}\right]+\frac{1}{2}}{\beta}-\frac{3}{10}\right), \end{aligned} \tag{3.22}$$

where β (introduced purely for readability) is given by

$$\beta \equiv \left(b_{\text{pis}}+b_{\text{cyl}}\right)^2+\left(b_{\text{pis}}+b_{\text{cyl}}+1\right)^2$$

and ϕ is the phase lead of the pressure (measured relative to the pressure phase in an ideal gas spring with identical piston motion). While not shown explicitly to avoid cluttering the equation, all variables are functions of axial position or local temperature *except* for ω, D, S, and δ_{gap}.

Note that the first term in equation (3.22) is simply Chang and Baik's expression for shuttle heat transfer (3.11) without the assumption of a linear temperature profile; the remaining terms capture the effects of flow and pressure fluctuations in the gap.

Equation (3.22) cannot be directly applied to the appendix gap in the form shown as the axial temperature gradient and mass flow rate amplitudes are not yet known. It seems difficult to find a closed-form solution for these terms; even approximating the temperature profile as a modest parabola with a single unknown (Ríos's approximation) yields a transcendental equation for the unknown parameter. There is, however, an effective way to compute the mass flow and temperature profile using a combination of equation (3.22) and numerical integration. In the absence of other heat transfers interactions, the First Law requires that the overall heat transfer rate from conduction, shuttle, and gas enthalpy transfer be constant along the expander's length in cyclic steady state; equation (3.22) may therefore be added to the equation for conduction heat transfer (3.10) and the result rearranged to isolate dT/dx:

$$\frac{dT}{dx} = \frac{\overbrace{\left[\dot{Q}_{\text{cond}}(x)+\dot{Q}_{\text{shuttle}}(x)+\dot{H}_{\text{GET}}(x)\right]}^{\equiv\,\dot{Q}_{\text{gap,net}},\ \text{constant along } x} - f\left(T(x),|P_1(x)|,|\dot{m}_1(x)|,\ldots\right)}{g\left(T(x),|P_1(x)|,|\dot{m}_1(x)|,\ldots\right)}, \tag{3.23}$$

where $f()$ and $g()$ are lengthy but closed-form functions of the other variables at a given axial position (reproduced in Appendix A.4).

Equation (3.23) along with equations (3.20) and (3.21) constitute a system of three non-linear, first-order ODEs which may be integrated numerically from the cold end to the warm end. Since $\dot{Q}_{\text{gap,net}}$ and the cold-end mass flow rate amplitude are initially unknown, an iterative "shooting" method is used: guess values are first assumed for the heat transfer rate and cold-end mass flow rate amplitude, then adjusted until the computed warm-end temperature is T_{warm} and the computed warm-end mass flow rate is zero. This hybrid analytical-numerical method captures the effects of transient conduction in the solids as well as non-linear temperature and velocity profiles in the fluid, but without the computational cost of finding a cyclic-steady-state solution to a 2-D finite difference problem. The approach also fits well with the iterative solution procedure used for the expander as a whole (described later in section 3.3.3).

With the expander temperature profile, mass flow rate amplitudes, and pressure amplitudes known, the results of the gap analysis can be distilled into three outputs for use in the expander cycle simulation:

- $\dot{Q}_{\text{gap,net}}$, the combined heat transfer rate due to conduction, shuttle, and gas enthalpy transfer (used to find the cyclic steady-state temperatures in the cold end of the expander);
- dm_{gap}/dP, a ratio relating the change of total fluid mass in the gap to the change of pressure in the cold end (used to find the mass flow rates into and out of the gap during the expander cycle); and
- $\overline{T}_{\text{gap,out}}$, the average temperature of fluid exiting the gap (used to approximate the effects of gap fluid mixing with fluid in the cold volume during the expansion and blow-out processes).

The first of these, $\dot{Q}_{\text{gap,net}}$, is one of the guess variables used in the iterative shooting method (the other is the cold-end mass flow rate amplitude) and is therefore found as part of the iterative solution process.

Finding dm_{gap}/dP is slightly more involved. First, conservation of mass is applied to a control volume consisting of the entire gap,

$$\frac{dm_{\text{gap}}}{dt} = \dot{m}(0). \tag{3.24}$$

Then, applying the chain rule to dm_{gap}/dP and substituting dm_{gap}/dt above,

$$\frac{dm_{\text{gap}}}{dP} = \frac{dm_{\text{gap}}}{dt} \Big/ \frac{dP}{dt} = \frac{\dot{m}(0)}{dP/dt}. \tag{3.25}$$

Replacing $\dot{m}$ and P in (3.25) with their complex exponential forms (3.16) and (3.17) yields

$$\frac{dm_{\text{gap}}}{dP} = \frac{\text{Re}\left\{\dot{m}_1(0)e^{i\omega t}\right\}}{\text{Re}\left\{i\omega P_1(0)e^{i\omega t}\right\}}; \tag{3.26}$$

since $\dot{m}$ was assumed to be in phase with dP/dt, this ratio may be simplified to

$$\frac{dm_{\text{gap}}}{dP} = \frac{|\dot{m}_1(0)|}{\omega |P_1(0)|}, \tag{3.27}$$

where $|\dot{m}_1(0)|$ is found during the iterative solution procedure and $|P_1(0)|$ is an input to the gap model.

The third output, $\overline{T}_{\text{gap,out}}$, may be related to the total enthalpy and mass of fluid exiting the gap ($H_{\text{gap,out}}$ and $m_{\text{gap,out}}$, respectively):

$$H_{\text{gap,out}} = m_{\text{gap,out}}\, c_P \left(\overline{T}_{\text{gap,out}} - T_{\text{cold}}\right). \tag{3.28}$$

Note that the enthalpy has been referenced to T_{cold}, the wall temperature of the cold working volume (and by extension, the wall temperature at the cold end of the gap). Now, the mass $m_{\text{gap,out}}$ may be found by integrating the mass flow rate from (3.16) over the half-cycle where $\dot{m} < 0$ (with an added negative sign to account for the opposite sign convention used for $m_{\text{gap,out}}$):

$$m_{\text{gap,out}} = -\int_{\dot{m}<0} \text{Re}\left\{\dot{m}_1(0) e^{i\omega t}\right\} dt = \frac{2\,|\dot{m}_1(0)|}{\omega}. \tag{3.29}$$

The enthalpy $H_{\text{gap,out}}$ may be found by returning to the derivation of equation (3.22) above, isolating terms corresponding only to the fluid, and integrating over one half-cycle (i.e., the time during which fluid is assumed to exit the gap with the present assumption of sinusoidal mass flow). The result is similar in form to equation (3.22) and is reproduced in Appendix A.4. As all quantities in equation (3.28) are now know, $\overline{T}_{\text{gap,out}}$ may be computed as

$$\overline{T}_{\text{gap,out}} = T_{\text{cold}} + \frac{H_{\text{gap,out}}}{m_{\text{gap,out}}}. \tag{3.30}$$

The temperature of fluid exiting the gap is determined by heat transfer within the gap and is expected to be largely independent of fluid temperature in the cold end. Fluid *entering* the gap during the other half of the cycle, however, is not influenced by gap heat transfer but by the processes in the cold-end working volume. This gives rise to an entry region at the cold end of the gap where the periodic solutions for fluid and solid temperature derived earlier (and therefore the breakdown of gas enthalpy transfer, conduction, and shuttle heat transfer) do not apply. As long as this entry region doesn't substantially affect the overall expander temperature profile, it may be dealt with by enforcing a First-Law constraint for a volume including the appendix gap, piston, and cylinder wall in the entry region as well as the cold-end walls as in Figure 3-10. As this constraint is dependent on the heat transfer from the cold-end walls to the working fluid it must ultimately be enforced by the expander model, not the gap model.

The appendix gap solution approach described above was implemented in MAT-

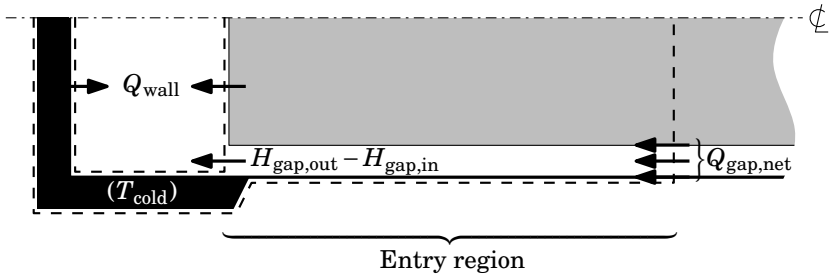

Figure 3-10: Control volume used to enforce the First Law at the cold end of the expander, consisting of the cold-end walls and a length of the appendix gap, piston, and cylinder wall. Over the course of a cycle, this control volume experiences heat transfers with fluid in the cold end (Q_{wall}), a net enthalpy transfer from cold-end fluid flowing in and out of the appendix gap ($H_{\text{gap,out}} - H_{\text{gap,in}}$), and a combination of conduction heat transfer, shuttle heat transfer, and gas enthalpy transfer from outside the entry region ($Q_{\text{gap,net}} \equiv Q_{\text{cond}} + Q_{\text{shuttle}} + H_{\text{GET}}$). Piston work transfers do not contribute a net energy flux to the indicated control volume and have been omitted for clarity.

LAB [TMW11]; the code is reproduced in Appendix B.2. Correlations in the NIST cryogenic properties database were used to compute the thermal conductivity and specific heat capacity of the piston and cylinder [NIST], and the densities of both materials (assumed to be independent of temperature) were obtained from the MatWeb database[5] [MW]. When G10 was used, the warp was assumed be oriented in the axial direction of the expander. The thermal conductivity of the fluid (helium) was computed from the following approximate fit in SI units, based on values from the NIST Chemistry WebBook [LMF] and accurate to within 1.1% of that data at 0.5 MPa and 10–400 K:

$$\log_{10}\left(k_{\text{He}}(T)\right) \approx 0.0665 \cdot (\log_{10} T)^2 + 0.3896 \cdot (\log_{10} T) - 2.1794 \tag{3.31}$$

Like shuttle and conduction, gas enthalpy transfer is reduced by smaller expander diameters. The effect of piston length is less clear: lengthening the piston reduces the temperature gradient but increases the total appendix gap volume, and correspondingly, both the dead volume of the expander and the mass flow rate in the gap (though longer pistons may also offer sealing effects that reduce the impact of the added volume). Gas enthalpy transfer is also mitigated by smaller gap widths; these offer lower total volume, smaller fluid-wall temperature differences, and at times better sealing. Additionally, the loss is expected to increase with higher expander pressure ratios as these would drive more fluid into and out of the appendix gap.

Cyclic heat transfer

Even in the absence of conduction, shuttle, or gas enthalpy transfer losses, cyclic fluid-wall heat transfers in the cold-end working volume give rise to irreversibility. As

[5] Specifically, from the material entries titled “304 Stainless Steel” and “G-10 Fiberglass Epoxy Laminate Sheet”.

the temperature and pressure of cold-end working fluid varies over each cycle, heat transfers are forced into and out of the relatively-isothermal walls. In general, such heat transfers are out of phase with the temperature fluctuations of the fluid due to the pressure work on the fluid's thermal boundary layer and are largest at intermediate operating speeds. For "high" operating speeds (when the thermal boundary layer is much smaller than the size the cold volume), a large temperature gradient exists between the fluid and the walls, but little heat transfer occurs during each cycle and the overall loss is small. For "low" operating speeds (when the characteristic length of heat transfer exceeds the size of the working volume), larger heat transfers are present but the fluid is nearly isothermal, again yielding little entropy generation. At intermediate speeds, however, significant temperature gradients and heat transfers are both present; these generate entropy and ultimately decrease the performance of the expander.

A multitude of papers and several theses have been written on the topic of cyclic heat transfer, which is also referred to in the literature as hysteresis heat transfer, compression-driven heat transfer, transient heat transfer, gas spring heat transfer, and gas spring hysteresis loss. It is no surprise that this has been a popular topic since it is important to the operation of internal combustion and Stirling engines as well as cryocoolers; however, only relevant highlights of the literature will be presented here.

Analyses of heat transfer in piston-cylinder machines date back to at least the early 1930s, with several papers appearing in the German-language literature. In 1940, Pfriem presented an analysis of periodic heat transfer, with an oft-cited English translation appearing in 1943 [Pfr40, Pfr43]. Pfriem considered an ideal gas with a well-mixed turbulent core and a low-velocity boundary layer, both subject to a small periodic pressure variation (which may in general be represented by a Fourier series). By assuming one-dimensional transient conduction in the boundary layer and wall, Pfriem derived a complex Nusselt number which captures both the magnitude and phase of the gas-wall heat transfer relative to the temperature of the turbulent gas core.

In MIT's Cryogenic Engineering Lab, experimental research by Lee and Smith showed the loss to be important to the operation of a heat engine in 1978 [LS78]. Faulkner and Smith showed the loss to be effectively independent of the cylinder wall material in 1983 [FS83]. Later the same year, Lee presented simple analytical expressions for the heat transfer coefficient and power loss due to cyclic heat transfer in a gas spring [Lee83]. Lee used similar assumptions as Pfriem but did not include a distinct turbulent core, opting instead to model turbulence with a uniformly-enhanced "effective thermal diffusivity." The resulting dimensionless power loss expression is plotted in Figure 3-11 in terms of the oscillating Peclet number, $\mathrm{Pe}_\omega \equiv \omega D_h^2/(4\alpha)$, and demonstrates the expected maximum at intermediate operating speeds.

Following the work of Pfriem, Lee and others, Kornhauser and Smith used the complex Nusselt number to correlate heat transfer data in a gas spring in 1988 [KS88]. Yagyu and Smith further extended the analysis to model heat transfer in a cylinder with non-sinusoidal piston motion [YS91]. Kornhauser and Smith later performed a

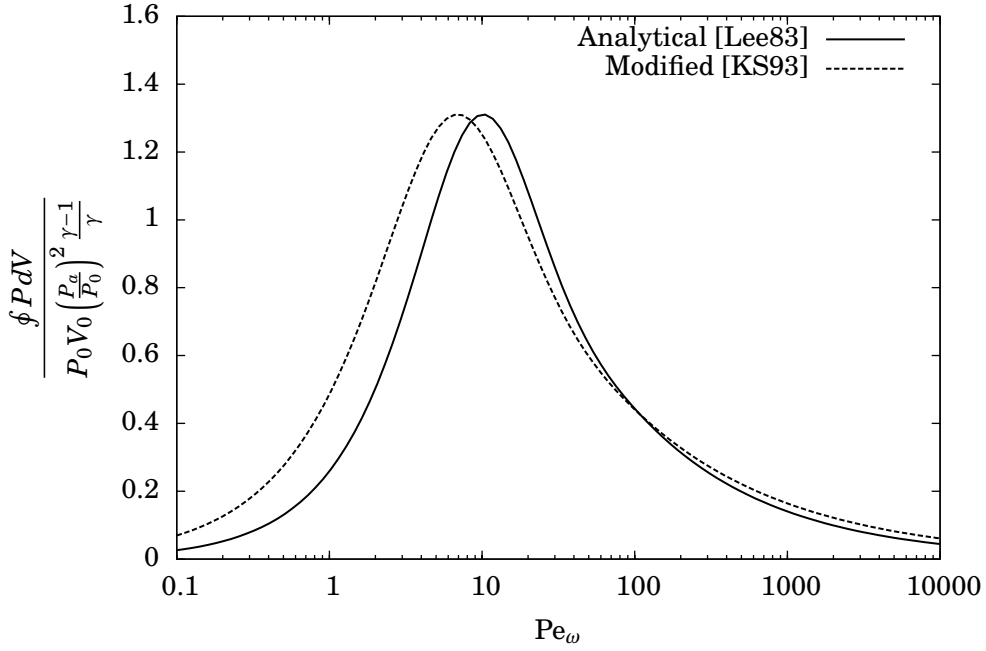

Figure 3-11: Dimensionless cyclic heat transfer power loss in a gas spring as a function of oscillating Peclet number (a dimensionless measure of operating speed). Losses are greatest for intermediate Peclet numbers, while they are small for both low and high Peclet numbers corresponding to nearly-isothermal and nearly-adiabatic working volumes, respectively. Both the analytical expression derived by Lee and the empirically-based modification proposed by Kornhauser are shown, though Kornhauser showed that these underpredict the actual loss in the high-Peclet-number regime when large volume ratios are used.

variety of experimental measurements of the net cyclic heat transfer loss and slightly modified Lee's analytical correlation of the loss to better fit the experimental data at high and low Peclet numbers [KS93]; the resulting modification is also plotted in Figure 3-11. Notably, the experimental data also showed that large volume ratios substantially increase the loss in the mostly-adiabatic regime; both the modified correlation and Lee's analytical expression therefore underpredict the loss at high Peclet numbers when the volume ratio is much greater that ~2. Kornhauser and Smith also published a revised version of their 1988 paper in 1994; this revised version includes additional experimental data and a revised least-squares fit of the complex Nusselt number for $\mathrm{Pe}_\omega \geq 100$ [KS94]. There have also been several attempts to better model the effect of turbulence on cyclic heat transfers; a paper by Cantelmi, Gedon, and Kornhauser [CGK98] gives a good review of the background in this area, and presents both an analytical model and a preliminary experimental validation.

The cyclic heat transfer model in this work followed an approach used by Wang to model heat transfer in a numerical Stirling cryocooler model [Wan89]. A complex Nusselt number was used to compute the instantaneous heat transfer $\dot{Q}_{\mathrm{wall}}$ from the working fluid to the walls was in terms of the instantaneous mixed-mean temperature

T of the cold end fluid and its time derivative dT/dt:

$$\dot{Q}_{\text{wall}} = \frac{k\left(\overline{T}\right)\overline{A_s}}{\overline{D_h}}\left[\text{Nu}_r\left(T - T_{\text{wall}}\right) + \frac{\text{Nu}_i}{\omega}\frac{dT}{dt}\right], \tag{3.32}$$

where $k\left(\overline{T}\right)$ is the thermal conductivity of the *fluid* in the cold end evaluated at the average gas temperature, $\overline{A_s}$ and $\overline{D_h}$ are the surface area and hydraulic diameter of the cold working volume at mean stroke (when the piston is halfway between its warm and cold extremes), and Nu_r and Nu_i are the real and imaginary components of the complex Nusselt number.

The use of an expression based on dT/dt over one based on dP/dt was deliberate: while dP/dt is completely agnostic to energy injected into the boundary layer during the isobaric intake process, using dT/dt is equivalent to assuming that the energy from entering fluid is distributed uniformly throughout both the core and the boundary layer. Neither of these approaches is fully physical, though the latter seemed more likely to capture the effects of fluid mixing during intake.

The choice of Nusselt number correlation also followed that of Wang. At low Peclet numbers the Nusselt number is computed using Lee's unmodified analytical correlation,

$$\text{Nu}_{[\text{Lee83}]} = \sqrt{2\text{Pe}_\omega}\frac{(1+i)\tanh z}{1-(\tanh z)/z}, \quad \text{where} \quad z \equiv (1+i)\sqrt{\text{Pe}_\omega/8}, \tag{3.33}$$

while at high Peclet numbers it is computed using the experimental fit presented by Kornhauser and Smith in 1994 (which is based on the observation that the real and imaginary parts of the Nusselt number are approximately equal when $\text{Pe}_\omega \geq 100$):

$$\text{Nu}_{[\text{KS94}]} = (1+i)0.56\text{Pe}_\omega^{0.69}. \tag{3.34}$$

Both correlations are plotted in Figure 3-12a. The use of (3.34) is admittedly questionable as it includes neither the effects of volume ratios greater than two nor the effects of inflow-induced turbulence, though developing an appropriate means of including these would likely require considerable guesswork or additional study (or both).

While Wang's model used a fixed Peclet-number cutoff to decide whether Lee's correlation (for $\text{Pe}_\omega < 100$) or the then-current version of Kornhauser and Smith's correlation (for $\text{Pe}_\omega \geq 100$) would be used, the present work interpolates smoothly between the two regimes in an effort to avoid numerical discontinuities. The large- and small-Peclet-number asymptotes of the correlations were combined through interpolants of the form[6]

$$y = \left(y_1^c + y_2^c\right)^{1/c}, \tag{3.35}$$

with values of $c = 2$ (for real parts) and $c = -7$ (for imaginary parts) chosen by eye to

[6]Note that a positive c yields an expression that asymptotes to $\max(y_1, y_2)$ and a negative c yields an expression that asymptotes to $\min(y_1, y_2)$. The width of the blending region is controlled by the magnitude of c, with greater magnitudes yielding narrower blending regions.

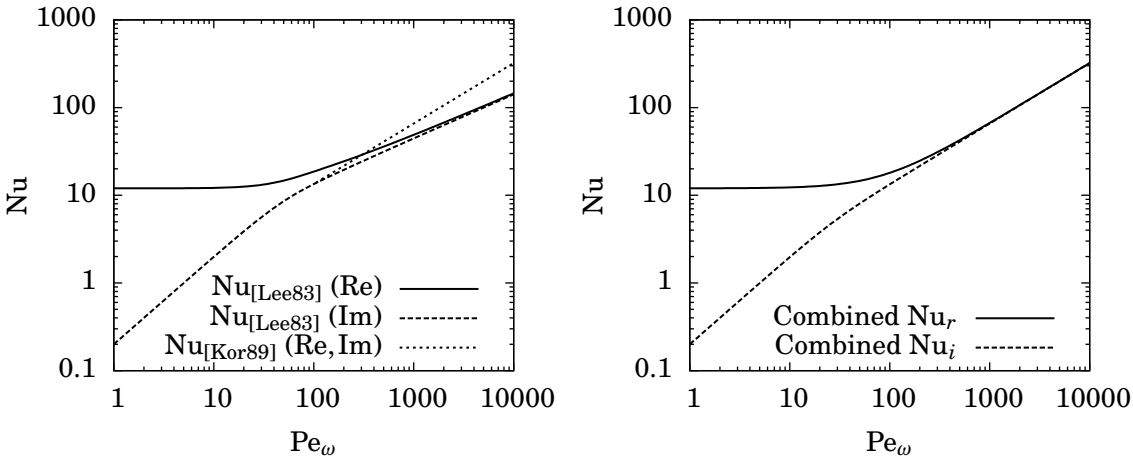

(a) Original correlations **(b)** Blended fit

Figure 3-12: Complex Nusselt number as a function of oscillating Peclet number. The analytical expression published by Lee is plotted in (a) along with the modified high-Peclet-number fit by Kornhauser, while (b) shows the blended Nusselt number used for the expander models in this thesis.

give a sensible amount of blending between the asymptotes. The resulting expressions (also plotted in Figure 3-12b) are:

$$\mathrm{Nu}_r \approx \left[(12)^2 + \left(0.56\mathrm{Pe}_\omega^{0.69}\right)^2\right]^{1/2}, \tag{3.36a}$$

$$\mathrm{Nu}_i \approx \left[(\mathrm{Pe}_\omega/5)^{-7} + \left(0.56\mathrm{Pe}_\omega^{0.69}\right)^{-7}\right]^{-1/7}. \tag{3.36b}$$

In expanders that are closer to adiabatic than isothermal (where Pe_ω is greater than ~100) the cyclic heat transfer loss is mitigated by using higher Peclet numbers. Lower-temperature expanders should be naturally biased towards higher Peclet numbers due to the lower thermal diffusivity of the working fluid. From an expander design perspective, a higher Peclet number may be attained by increasing the expander's operating frequency, raising the mean fluid pressure to reduce its thermal diffusivity, and minimizing the surface area per unit cooling in the cold working volume. The latter of these led to the design heuristic used in earlier versions of the FPE, which suggests that the stroke length should be about the same as the expander diameter ($S \approx D$). This heuristic makes sense when the cyclic heat transfer loss dominates the performance of the expander, but does not always hold in the presence of other losses. The cyclic heat transfer is also mitigated by using lower pressure ratios as these reduce the energy imparted to the boundary layer (but also provide less cooling).

Intake mixing

In addition to being irreversible in and of themselves, cyclic and appendix gap heat transfers influence the temperature of the working fluid in the cold end. Consequently, it is unlikely that fluid in the cold end will have the same temperature as the fluid entering during the blow-in and intake processes, a discrepancy which leads to entropy generation by irreversible mixing.

At first glance it seems like this loss is mitigated by decreasing the heat transfer from the walls to the cold volume as much as possible, with the aim to make the expansion proceed nearly adiabatically; however, this simple reasoning is complicated by the presence of the appendix gap losses. Since shuttle and conduction transfer heat into the walls of the cold end, a lower heat transfer coefficient from the cold end walls to the fluid may result in a higher wall temperature, with reduced shuttle and conduction losses but an unclear effect on gas enthalpy transfer losses. While these interactions may make an interesting topic for future study, they are not examined separately in this work but implicitly incorporated into the expander model by virtue of the numerical solution approach used.

Incidentally, the intake mixing loss described above is similar to the well-known "adiabatic loss" in Stirling modeling. Expansion and compression are isothermal in ideal Stirling machines, with fluid entering and exiting the working volumes at a constant temperature. In actual Stirling machines, however, expansion and compression are not perfectly isothermal, leading to irreversibilities when fluid enters and exits the working volumes. Further information about such adiabatic losses may be found without difficulty in the Stirling engine literature.

Blow-in and blow-out

Unlike the other cold-end processes in the expansion cycle (which are plagued by parasitic losses but are not inherently lossy), blow-in and blow-out are run-down processes and therefore irreversible by nature. Furthermore, these processes are always present in the current FPE design: since recompression is driven by the warm-end reservoirs, the expander pressure at the end of recompression cannot exceed P_{A} which itself is less than P_{in}, and the resulting pressure difference causes fluid to rush irreversibly into the expander when the cold-end intake valve is opened. Similarly, since expansion does not proceed all the way to P_{out}, there is an irreversible outrush of fluid when the exhaust valve is opened.

As with the intake mixing loss above, irreversibilities arising from rapid blow-in and blow-out flows are implicitly accounted for when the governing equations for the expander cycle are integrated; no separate loss model is needed. What *is* needed, however, is a way of specifying the warm-end pressures on which these losses depend. While this thesis does not examine how stable warm-end reservoir pressures are established or controlled, the topic was recently investigated by Hogan [Hog12]. Instead of conducting a separate warm-end analysis for the present work, the pressures

at the end of expansion and recompression are considered inputs to the model and captured in two dimensionless factors f_{high} and f_{low}, defined such that $f_{\text{high}}P_{\text{in}}$ is the pressure immediately before blow-in and $f_{\text{low}}P_{\text{out}}$ is the pressure immediately before blow-out. The closer these factors are to unity, the less the blow-in and blow-out. For high-pressure-ratio expanders similar to those examined here, numerical simulations conducted by Hogan suggests typical values of $0.9 < f_{\text{high}} < 0.95$ and $1.5 < f_{\text{low}} < 2$ when warm-end bleed flows are not used. Additionally, the control algorithm presented by Hogan permits the amount of blow-in to be reduced at the expense of blow-out and vice-versa.

Interestingly, blow-in and blow-out can be *beneficial* to expander performance when considered alongside the other losses. While they themselves are irreversible, blow-in and blow-out permit the use of shorter stroke lengths and smaller diameters and can thus reduce losses from shuttle and other mechanisms. This unexpected conclusion is demonstrated by the results shown later in this chapter. Of course, other factors must be considered in selecting suitable blow-in and blow-out amounts, as both processes have the potential to accelerate the piston to high velocities and cause damage to the expander. The piston's motion may be limited during the blow-out process by reducing the warm-end clearance volume, but motion during the blow-in process is more difficult to control; since the piston is at the cold end of its stroke, the volume of the warm end is at a maximum and so has a lower effective spring constant. Particular care should therefore be taken if blow-in factors are large, either by necessity or by design.

Valve losses (neglected)

In addition to the six losses above, at least five more losses have been identified that were *not* included in the present model of the FPE. The first of these results from the pressure drops across the cold-end valves during the intake and exhaust processes. Commonly referred to as "valve losses", these irreversibilities are distinct from blow-in and blow-out since they occur during parts of the cycle where the rate is nominally limited by warm-end throttling. Blow-in and blow-out, in contrast, are necessarily limited by a combination of cold-end flows and piston dynamics since the warm-end valves are closed during those processes.

Larger valve losses impact expander performance by reducing the pressure difference available for useful expansion. The losses are a function of both the valve design and the mass flow rate through the valves during intake and exhaust.

Appendix gap hysteresis (neglected)

A little-discussed phenomenon know as appendix gap hysteresis was also not included in this work, though it is possible that some of its effects are implicitly included in the gas enthalpy transfer analysis. Conceptually, appendix gap hysteresis losses are similar to cyclic heat transfer losses except for their location: entropy is generated by

irreversible heat transfer between fluid in the appendix gap and the appendix gap walls instead of in the cold-end working volume.

The only explicit analysis of this loss in the literature appears to be that of Berchowitz and Berggren [BB81] (and by extension, the updated version obtained from Berchowitz). As discussed earlier, however, this study assumes that flow in the gap is entirely inertial; it is therefore unlikely that the analysis applies to low-frequency, high-pressure-ratio FPEs. For the present work, the treatment of shuttle and gas enthalpy transfer presented earlier (pp. 65–71) was assumed to suffice in modeling the effects of the gap on the expansion cycle, though further examination of appendix gap hysteresis may make an interesting topic for future study.

Piston blow-by (neglected)

One additional gap-related loss was ignored when modeling the floating expander: fluid flow past the piston, either from the warm end working volume to the cold end or vice versa. Such piston "blow-by" can occur whenever there is a pressure difference across the piston that forces fluid past the piston-cylinder seal. If a net non-regenerative flow occurs from the warm end to the cold end (as may be the case when warm-end bleed flows are used) it can impose a significant heat load on the expander, though it may be possible to mitigate this by placing the expander walls in thermal contact with the recuperator in order to capture some of that load at a higher temperature. The shuttle, conduction, and gas enthalpy transfers affecting the steady-state axial temperature distribution in the appendix gap may also alter the impact of blow-by losses.

Pressure differences driving blow-by may occur as a result of gravity acting on the piston in terrestrial applications, friction resisting the piston's motion, or the piston's finite inertia (which will introduce a time lag between warm- and cold-volume pressure changes and potentially oscillations in pressure if the piston's motion is underdamped). Another major source of blow-by could result if the piston were allowed to reach and sit against the cold end of the expander before recompression had increased the cold-end pressure to P_A; in that case, the fluid in the cold end could not be compressed any further, but the pressure in the warm end would continue to rise as mass is added from the reservoirs. The piston would no longer "float" between the two working volumes. In some cases this may result in a net efficiency gain due to the shorter piston stroke and correspondingly reduced shuttle losses, though other factors will also govern the feasibility of large pressure imbalances (including the compressive load that the piston would need to withstand).

Blow-by can also affect the mass and pressure of fluid in the warm end reservoirs; since this affects the execution of the cycle, care must be taken to keep the pressures in the desired ranges. While warm-end bleed valves can be used to accomplish this, an alternative is to use a control algorithm that deliberately induces blow-by in the direction needed (e.g., by seating the piston against one end of the expander). The latter strategy was explored in considerable detail by Hogan [Hog12], but for the

expander models in the present work the piston was constrained to float at all times and blow-by from the other sources described above was assumed to be small.

Warm-end bleed loss (neglected)

Even if they are not a source of non-regenerative blow-by, warm-end bleed flows require mass flow from the compressor which bypasses the recuperators, expanders, and load heat exchangers and does not directly contribute to the cooling power of the cryocooler. While the added compressor power does not show up in the expander efficiency (which is only concerned with the enthalpy decrease of the cold-end working fluid), it must be considered when computing the overall cryocooler efficiency should it ever prove necessary to use bleed flows.

Warm-end dissipation (neglected)

Lastly, the current design of the floating piston expander dissipates all the energy removed from the cold-end working fluid.[7] The impact of this loss is felt most in cryocoolers operating across a small temperature ratio (that is, the temperature at which heat is rejected to ambient is relatively close to the cold-end temperature); in such machines, the work extracted from the cold end represents a substantial fraction of the overall compressor work. The situation is considerably better in high-delta-T cryocoolers where the required compressor power greatly exceeds the cooling power. Engineering a mechanism to capture some of the expander work nevertheless seems like an attractive prospect, though no mechanism has yet been proposed which retains the simplicity of the original FPE design.

Like the warm-end bleed loss, warm-end dissipation reduces the overall efficiency of the cryocooler but does not directly appear in the expander efficiency as defined in this thesis (i.e., as the ratio of actual refrigeration to ideal refrigeration). Nevertheless, warm-end dissipation may indirectly reduce the expander's efficiency by increasing the temperature of the warm end and thus increasing the amount of shuttle and conduction heat transfer. This may be mitigated by providing a suitable means for transferring heat away from the warm end.

3.3.2 Cycle Model

Understanding the key losses in an FPE is an important precursor to making well-informed design tradeoffs. The models described above, however, do not paint a clear picture of how the losses affect an expander's performance in aggregate. The goal of the cycle model presented in this section is to examine the combined effect of the losses in the context of an expander.

[7] While the warm-end reservoirs do store energy on a per-cycle basis to execute the recompression process, the *net* energy removed is ultimately dissipated and exits the warm end as a heat transfer instead providing usable work.

The cycle model was developed by applying conservation laws to the cold-end working volume of the expander (incorporating Nusselt numbers from the cyclic heat transfer analysis and mass flow rates and temperatures from the appendix gap analysis), yielding a non-linear ordinary differential equation for each of the processes in the cycle. The ODEs may then be integrated numerically, though they must be combined with a suitable solver (section 3.3.3) to enforce a cyclic steady state.

Several simplifying assumptions were made in addition to those inherent in the loss models:

- The working fluid was assumed to be an ideal gas with gas constants R and c_P.
- Any fluid exiting the cold-end working volume was assumed to do so at its instantaneous mixed-mean temperature, $T(t)$.
- The pressure $P(t)$ was assumed to be spatially-uniform and identical in the warm end and cold end of the expander (inertial effects, friction, and gravity acting on the piston were thus all neglected).
- For the purpose of computing wall heat transfers in the cold volume, dP/dt and dV/dt were approximated as known constants (discussed in more detail below).
- Kinetic and gravitational terms were neglected in all governing equations.
- The walls of the cold-end working volume (including the cold end of the piston) were assumed to have very high heat capacity and thermal effusivity such that they remained at a constant temperature throughout each cycle.

Additionally, all equations were nondimensionalized (primarily to improve the accuracy of the numerical integrations) using the following relations:

$$\tilde{P} \equiv P/P_{\text{in}}, \tag{3.37a}$$
$$\tilde{V} \equiv V/V_{\text{swept}}, \tag{3.37b}$$
$$\tilde{T} \equiv T/T_{\text{in}}, \tag{3.37c}$$
$$\tilde{m} \equiv mRT_{\text{in}}/\left(P_{\text{in}}V_{\text{swept}}\right), \tag{3.37d}$$
$$\tilde{h} \equiv h/(RT_{\text{in}}), \tag{3.37e}$$
$$\tilde{E} \equiv E/\left(P_{\text{in}}V_{\text{swept}}\right), \tag{3.37f}$$
$$\tilde{Q} \equiv Q/\left(P_{\text{in}}V_{\text{swept}}\right), \tag{3.37g}$$
$$\tilde{W} \equiv W/\left(P_{\text{in}}V_{\text{swept}}\right), \tag{3.37h}$$
$$\tilde{t} \equiv t\omega, \tag{3.37i}$$

where the variables represent, in order, dimensionless versions of pressure, volume, temperature, mass, specific enthalpy, energy, heat transfer, work transfer, and time. Applying these substitutions leads to the following general form of the First Law (neglecting kinetic and gravitational terms),

$$d\tilde{E} = \delta\tilde{Q} - \delta\tilde{W} + \tilde{h}_{\text{in}}\delta\tilde{m}_{\text{in}} - \tilde{h}_{\text{out}}\delta\tilde{m}_{\text{out}}, \tag{3.38}$$

as well as dimensionless forms of the ideal gas energy, enthalpy, and property constitutive relations,

$$\tilde{E} = \frac{1}{\gamma - 1}\tilde{m}\tilde{T}, \tag{3.39}$$

$$\tilde{h} = \frac{\gamma}{\gamma - 1}\tilde{T}, \tag{3.40}$$

$$\tilde{P}\tilde{V} = \tilde{m}\tilde{T}. \tag{3.41}$$

The dm_{gap}/dP ratio from the pumping loss analysis (equation (3.27)) was also nondimensionalized,

$$\frac{d\tilde{m}_{\text{gap}}}{d\tilde{P}} = \left(\frac{dm_{\text{gap}}}{dP}\right)\frac{RT_{\text{in}}}{V_{\text{swept}}}, \tag{3.42}$$

along with the wall heat transfer expression from the cyclic heat transfer analysis (equation (3.32)) which was rewritten in terms of the heat transfer $\delta\tilde{Q}$ into the fluid instead of the heat transfer into the walls:

$$\delta\tilde{Q} = \tilde{C}_r\left(\tilde{T} - \tilde{T}_{\text{wall}}\right)d\tilde{t} + \tilde{C}_i d\tilde{T}, \tag{3.43}$$

where $\tilde{C}_r$ and $\tilde{C}_i$ are dimensionless coefficients based on the real and imaginary parts of the Nusselt number:

$$\tilde{C}_r \equiv \left(\frac{-k\left(\overline{T}\right)\overline{A_s}}{\overline{D_h}} \cdot \text{Nu}_r\right)\frac{T_{\text{in}}}{\omega P_{\text{in}} V_{\text{swept}}}, \tag{3.44a}$$

$$\tilde{C}_i \equiv \left(\frac{-k\left(\overline{T}\right)\overline{A_s}}{\overline{D_h}} \cdot \frac{\text{Nu}_i}{\omega}\right)\frac{T_{\text{in}}}{P_{\text{in}} V_{\text{swept}}}. \tag{3.44b}$$

Note that the heat transfer (3.43) has an explicit dependence on time. Since the durations of each process in the cycle are not known a priori, however, an approximate method was used: the time dependence was rewritten as either $dt = dV \cdot (dV/dt)^{-1}$ or $dt = dP \cdot (dP/dt)^{-1}$, with the rates dV/dt and dP/dt estimated in terms of known quantities. Since the piston must traverse the swept volume twice each cycle, the magnitude of dV/dt is approximately twice the swept volume divided by the cycle's period, $t_{\text{cycle}} = 2\pi/\omega$:

$$\left|\frac{dV}{dt}\right| \approx \frac{2V_{\text{swept}}}{t_{\text{cycle}}} = \frac{\omega V_{\text{swept}}}{\pi}. \tag{3.45}$$

Similarly, the magnitude of dP/dt is approximately twice the difference in the inlet and outlet pressures divided by the cycle time:

$$\left|\frac{dP}{dt}\right| \approx \frac{2(P_{\text{in}} - P_{\text{out}})}{t_{\text{cycle}}} = \frac{\omega(P_{\text{in}} - P_{\text{out}})}{\pi}. \tag{3.46}$$

Using these estimates, the dimensionless differential time $d\tilde{t}$ in equation (3.43) may be replaced with either $\pm\pi d\tilde{V}$ or $\pm\pi d\tilde{P}/(1 - \tilde{P}_{\text{low}})$, where the signs depend on the direction of the process.

Since the pressure in the cold volume was assumed to be uniform at all times, the work transfer from the cold volume to the floating piston may be written as $\delta\tilde{W} = \tilde{P}d\tilde{V}$. Additionally, since the temperature of fluid exiting the cold volume was always assumed to be at the mixed-mean temperature, $\tilde{T}_{\text{out}}$ may be replaced with $\tilde{P}\tilde{V}/\tilde{m}$. Applying the First Law (3.38) to the cold-end working volume and using the substitutions above along with the ideal gas constitutive relations (3.39)–(3.41) yields

$$\gamma\tilde{P}d\tilde{V} + \tilde{V}d\tilde{P} = (\gamma-1)\delta\tilde{Q} + \gamma\tilde{T}_{\text{in}}\delta\tilde{m}_{\text{in}} - \gamma\left(\frac{\tilde{P}\tilde{V}}{\tilde{m}}\right)\delta\tilde{m}_{\text{out}}; \tag{3.47}$$

this equation is the starting point for all the process analyses below. For reference, a P-V diagram of the cycle with the processes labeled is shown in Figure 3-13.

For the remainder of section 3.3.2, the tildes (˜) denoting dimensionless variables will be omitted for clarity.

Blow-in and blow-out

During the blow-in and blow-out processes all warm-end valves are closed. Gas in the warm end is assumed to undergo a reversible adiabatic process with volume and pressure related by

$$PV_{\text{warm}}^{\gamma} = \text{Const.} = P_1 V_{1,\text{warm}}^{\gamma}. \tag{3.48}$$

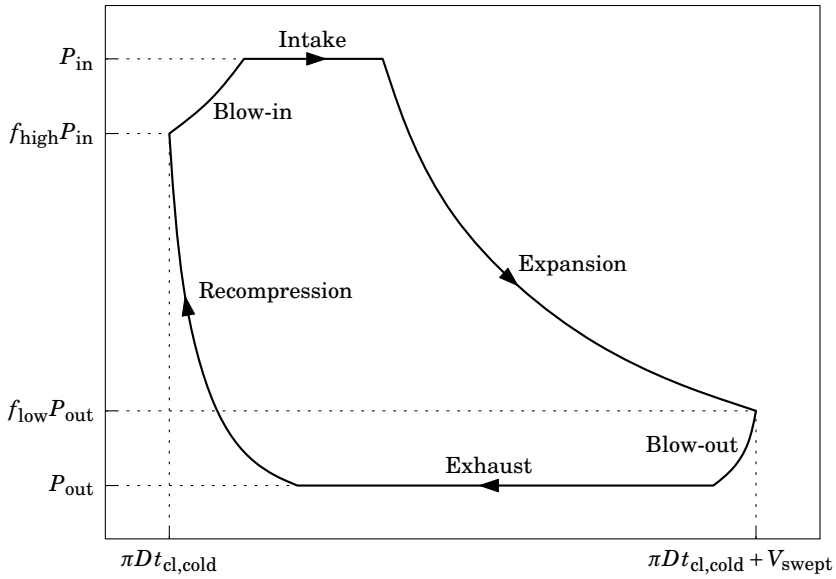

Figure 3-13: Cold-end P-V diagram for the irreversible FPE model. For full descriptions of each process, see p. 21.

Since the cold-end volume is related to the warm-end volume by geometry, the cold-end volume is therefore also known as a function of pressure.

Changes in pressure also force fluid into and out of the appendix gap as described in the analysis of gas enthalpy transfer (see section 3.3.1); the amount and direction of this mass flow is given by $\delta m = -\left(dm_{\text{gap}}/dP\right) \cdot dP$, where positive values of δm correspond to mass flows from the gap to the cold-end volume.

The differential equations for blow-in and blow-out were constructed with the pressure P as the independent variable, as both processes have prescribed initial and final pressures. Combining the modified First Law (3.47) with conservation of mass, the wall heat transfer expression (3.43), and the warm-end pressure-volume relation (3.48) yields the following ODE:

$$\frac{dT}{dP} = \frac{\left(\frac{\gamma-1}{\gamma}\right) C_r \left(T - T_{\text{wall}}\right) \frac{dt}{dP} + \left(\frac{T_{\text{io}}}{T} - 1\right) P \frac{dV}{dP} + \left(\frac{T_{\text{io}}}{T} - \frac{1}{\gamma}\right) V + \frac{dm_{\text{gap}}}{dP}\left(T_{\text{io}} - T_{\text{gap,io}}\right)}{\frac{T_{\text{io}}}{T}\left(\frac{PV}{T}\right) - \left(\frac{\gamma-1}{\gamma}\right) C_i}, \tag{3.49a}$$

$$\text{where} \quad V = V_1 + V_{1,\text{warm}} \left[1 - \left(\frac{P}{P_1}\right)^{-1/\gamma}\right], \tag{3.49b}$$

$$\frac{dV}{dP} = \frac{V_{1,\text{warm}}}{\gamma P_1} \left(\frac{P}{P_1}\right)^{-1-1/\gamma}, \tag{3.49c}$$

$$T_{\text{io}} = \begin{cases} 1 & \text{for blow-in,} \\ T & \text{for blow-out,} \end{cases} \tag{3.49d}$$

$$\text{and} \quad T_{\text{gap,io}} = \begin{cases} T & \text{for blow-in,} \\ \overline{T}_{\text{gap,out}} & \text{for blow-out.} \end{cases} \tag{3.49e}$$

The variables T_{io} and $T_{\text{gap,io}}$ have been introduced to represent the temperature of flows into and out of the cold-end working volume as these depend on which process (blow-in or blow-out) is being modeled. T_{io} is the temperature of fluid entering and exiting via the inlet and exhaust valves, while $T_{\text{gap,io}}$ is the temperature of fluid entering or exiting via the appendix gap.

Equation (3.49) may now be integrated over the domain $P = [f_{\text{high}}, 1]$ for the blow-in process and $P = [f_{\text{low}} P_{\text{out}}, P_{\text{out}}]$ for the blow-out process. Once the final temperature is known, it may be used along with pressure and volume to find the remaining state variables (including the mass of fluid in the cold end).

Integrated values for the wall heat transfer Q_{wall} and net fluid enthalpy transfer H_{gap} from the appendix gap may also be calculated simultaneously with the temperature by integrating two more equations (again with P as the independent

variable):

$$\frac{\delta Q_{\text{wall}}}{dP} = -C_r (T - T_{\text{wall}}) \frac{dt}{dP} - C_i \frac{dT}{dP}, \tag{3.50}$$

$$\frac{\delta H_{\text{gap}}}{dP} = \gamma \left(T_{\text{gap,io}} - T_{\text{wall}}\right) \left(\frac{dm_{\text{gap}}}{dP}\right). \tag{3.51}$$

These quantities are not needed to solve the blow-in and blow-out processes but are used later in the solution process when the First Law is enforced for the appendix gap and cold-end walls. The choice of T_{wall} as the reference temperature for the enthalpy transfer is arbitrary since T_{wall} is assumed constant and will therefore not contribute to the integrated value of H_{gap} for the cycle as a whole.

Intake and exhaust

During both intake and exhaust the pressure is assumed constant. Since the appendix gap mass flow was assumed to be in phase with cold-end pressure fluctuations, this also implies that there is no flow into or out of the appendix gap. In both processes, the cold-end mass m is used as the independent variable, which allows the amount of intake mass to be varied by changing the limits of integration. Just as for the blow-in and blow-out processes, an ODE was derived for the intake and exhaust processes:

$$\frac{dV}{dm} = \frac{\left(\frac{\gamma-1}{\gamma}\right) C_i \frac{PV}{m^2} - T_{\text{io}}}{\left(\frac{\gamma-1}{\gamma}\right) C_r \left(\frac{PV}{m} - T_{\text{wall}}\right) \frac{dt}{dV} + \left(\frac{\gamma-1}{\gamma}\right) C_i \frac{P}{m} - P}, \tag{3.52a}$$

$$\text{where} \quad T_{\text{io}} = \begin{cases} 1 & \text{for intake,} \\ \frac{PV}{m} & \text{for exhaust,} \end{cases} \tag{3.52b}$$

$$\text{and} \quad P = \begin{cases} 1 & \text{for intake,} \\ P_{\text{out}} & \text{for exhaust.} \end{cases} \tag{3.52c}$$

Corresponding equations for the wall heat transfer and gap-flow enthalpy transfer were also found:

$$\frac{\delta Q_{\text{wall}}}{dm} = -C_r \left(\frac{PV}{m} - T_{\text{wall}}\right) \frac{dt}{dV} \frac{dV}{dm} - C_i \frac{P}{m} \left(\frac{dV}{dm} - \frac{V}{m}\right), \tag{3.53}$$

$$\frac{\delta H_{\text{gap}}}{dm} = 0. \tag{3.54}$$

Expansion and recompression

The expansion and recompression processes begin and end at known pressures, making P a natural choice for the independent variable. Once again deriving an ODE for

the processes,

$$\frac{dT}{dP} = \frac{\left(\frac{\gamma-1}{\gamma}\right) C_r (T - T_{\text{wall}}) \frac{dt}{dP} + \left(\frac{\gamma-1}{\gamma}\right) \frac{mT}{P} + \frac{dm_{\text{gap}}}{dP} \left(T - T_{\text{gap,io}}\right)}{m - \left(\frac{\gamma-1}{\gamma}\right) C_i}, \tag{3.55a}$$

$$\text{where} \quad m = m_1 - \left(\frac{dm_{\text{gap}}}{dP}\right)(P - P_1) \tag{3.55b}$$

$$\text{and} \quad T_{\text{gap,io}} = \begin{cases} \overline{T}_{\text{gap,out}} & \text{for expansion,} \\ T & \text{for recompression,} \end{cases} \tag{3.55c}$$

with integration limits of $P = [1, f_{\text{low}} P_{\text{out}}]$ for expansion and $P = [P_{\text{out}}, f_{\text{high}}]$ for recompression. The wall heat transfer and gap enthalpy flow expressions are the same as for the blow-in and blow-out processes (equations (3.50) and (3.51)).

3.3.3 Solution Procedure

The ODEs developed above may be used to simulate the behavior of an expansion cycle for a given set of initial conditions and parameters (e.g., the initial pressure, cold-end mass, and steady-state wall temperature T_{wall}, among others). What is now needed is a way of identifying the cyclic steady state of the expander.

The cyclic-solution approach taken in this work is known as a "single shooting method": guesses are chosen for unknown variables at the beginning of a cycle, a complete cycle is integrated, and the guesses are adjusted using a numerical solver until a cyclic steady state is found. Several other methods exists for identifying cyclic steady states; while these will not be discussed here, a good summary including various references to the literature is given by Andersen [And06, Ch. 4].

Algorithm

The solution algorithm used in the present work comprises five basic steps:

1. **Input:** Fixed parameters and guess variables are provided to the model
2. **Losses:** Loss-related variables are computed based on the guesses
3. **Processes:** ODEs are integrated over one cycle, beginning with blow-in
4. **Output:** Outputs and constraints for the iterative solver are computed
5. **Iteration:** The guesses are adjusted by a numerical solver and 1–4 are repeated until the constraints are satisfied

This approach proved fairly robust and converged with most geometries and operating conditions tested.

The majority of the inputs to the model are fixed parameters that describe the geometry, materials, and operating conditions of the expander; these are summarized in Table 3.2. The remaining five inputs are guess variables which are varied by the numerical solver (in dimensionless form) to find a cyclic steady state:

- m_{intake}, the mass of fluid taken into the expander during the intake stroke
- T_{recomp}, the cold-end fluid temperature following recompression and immediately preceding blow-in, used as an initial condition
- T_{wall}, the cold-end wall temperature, required both to compute cold-end wall heat transfers and as a boundary condition for the appendix gap model
- $\dot{Q}_{\text{gap,net}}$, the sum of conduction, shuttle, and pumping, required for the appendix gap solution method (see equation (3.23) and the surrounding discussion)

Table 3.2: Floating piston expander model inputs.

Category	Input	Description	Units
Operating conditions	f	Frequency	[Hz]
	T_{warm}	Average warm-end temperature	[K]
	T_{in}	Inlet temperature	[K]
	P_{in}	Inlet pressure	[Pa]
	$P_{\text{in}}/P_{\text{out}}$	Expander pressure ratio	[]
	f_{bi}	Blow-in factor $\left(\equiv \frac{P_{\text{in}}-f_{\text{high}}P_{\text{in}}}{P_{\text{in}}-P_{\text{out}}}\right)$	[]
	f_{bo}	Blow-out factor $\left(\equiv \frac{f_{\text{low}}P_{\text{out}}-P_{\text{out}}}{P_{\text{in}}-P_{\text{out}}}\right)$	[]
Geometry	D	Diameter	[m]
	S/D	Stroke-length-to-diameter ratio	[]
	δ_{gap}/D	Gap-thickness-to-diameter ratio	[]
	t_{pis}/D	Piston-thickness-to-diameter ratio	[]
	t_{cyl}/D	Cylinder-thickness-to-diameter ratio	[]
	$t_{\text{cl,cold}}/D$	Cold unswept-length-to-diam. ratio	[]
	$t_{\text{cl,warm}}/D$	Warm unswept-length-to-diam. ratio	[]
Materials	mat_{pis}	Piston material (G10 or 304 steel)	–
	mat_{cyl}	Cylinder material (G10 or 304 steel)	–
Guess variables	$m_{\text{intake}}/m_{\text{ideal}}$	Intake-stroke mass correction*	[]
	$T_{\text{recomp}}/T_{\text{in}}$	N.D. post-recompression temperature	[]
	$T_{\text{wall}}/T_{\text{in}}$	N.D. cold-end wall temperature	[]
	$f_{\text{gap},\dot{\text{Q}}}$	Gap heat transfer correction**	[]
	$f_{\text{gap,m}}$	Gap mass flow correction**	[]

* Ratio of actual intake mass to "ideal" mass from section 3.2 (T_{out} in equation (3.2))
** Ratios of actual $\dot{Q}_{\text{gap,net}}$ and dm_{gap}/dP to estimates based on a linear temp. profile

- dm_{gap}/dP, the pressure derivative of mass in the appendix gap, required for both the gap solution method and the integration of most cold-end processes

Note that the intake mass will directly affect the computed cold-end volume at the end of the expansion process (which proceeds to a pressure of $f_{\text{low}}P_{\text{out}}$ regardless of the amount of mass). For the solution to be valid, however, this computed volume must match the volume specified by geometric inputs such as the diameter and the stroke-to-diameter ratio. A total of five such constraints must be satisfied by adjusting the guess variables as described above:

- The swept volume computed during the integration process must match the given expander geometry.
- The final cold-end volume must match the initial cold-end volume.
- The First Law must be satisfied for a system consisting of the cold-end walls, the piston and cyclinder, and the appendix gap (see Figure 3-10).
- The appendix gap warm-end temperature computed by integration must match the specified temperature T_{warm}.
- The appendix gap mass flow rate must be zero at the gap's sealed warm end.

These constraints are provided as outputs from the model along with other important results such as the adiabatic efficiency, cooling power, and mass flow per cycle (summarized in Table 3.3).

Of course, this is only one way to solve the behavior of the cycle; as an example of another, the temperature following expansion and immediately preceding blow-out could have been chosen as the initial condition, with a different set of guess variables to match.[8]

Implementation

The algorithm described above was implemented in MATLAB [TMW11]. The MATLAB code is included in Appendix B. The bulk of the code follows the algorithm straightforwardly, but is split into two files: "fpe_model.m", which contains all but the appendix gap model, and "fpe_gap.m", a function dedicated to solving the appendix gap behavior as described in section 3.3.1. Both of these relied on MATLAB's built-in numerical integration functions, though no additional toolboxes were used. Specifically, the expander model employs the `ode15s` stiff-equation solver with its default options to integrate the process ODEs. The trapezoidal integration function `trapz` is also used to compute the enthalpy efflux during blow-out and exhaust (a precursor to computing

[8] A previous attempt to integrate some of the processes *backwards* in time, however, proved to be numerically unstable due to the gas-wall heat transfers in the cold end. When reversed in time, such heat transfers can cause the integration to diverge rapidly from an initial condition.

Table 3.3: Floating piston expander model outputs.

Category	Output	Description	Units
State	P_{vec}	Cold-end pressure vector	[Pa]
	V_{vec}	Cold-end volume vector	[m^3]
	T_{vec}	Cold-end temperature vector	[K]
	s_{vec}	Cold-end specific entropy vector	[J/kg-K]
	T_{wall}	Steady-state cold wall temperature	[K]
Loss-related	$Q_{\text{wall,vec}}$	Heat transfer to cold walls (vector)	[J]
	$H_{\text{gap,vec}}$	Enthalpy flow into gap (vector)	[J]
	$Q_{\text{shuttle}} + Q_{\text{cond}}$	Shuttle and conduction heat trans. per cycle*	[J]
	H_{GET}	Gas enthalpy transfer per cycle*	[J]
	$\overline{T}_{\text{gap,out}} - T_{\text{wall}}$	Temp. difference of fluid *exiting* gap	[K]
Performance	η	Adiabatic efficiency	[]
	$\dot{Q}_{\text{cool}}$	Cooling power	[W]
	$\dot{m}$	Time-averaged mass flow rate	[kg/s]
Constraint	$\frac{V_{\text{swept,actual}}}{V_{\text{swept,guess}}} - 1$	Swept volume must match guess	[]
	$\frac{V_{\text{final}}}{V_{\text{initial}}} - 1$	Final volume must match initial volume	[]
	$\oint \frac{\delta Q_{\text{wall+gap}}}{P_{\text{in}} V_{\text{swept}}}$	First Law must be satisfied	[]
	$\frac{T(L)}{T_{\text{warm}}} - 1$	Gap temp. must be T_{warm} at warm seal	[]
	$\dot{m}_1(L)/\dot{m}_1(0)$	Gap flow must be zero at warm seal	[]

* Spatially averaged over length of gap (as in Figure 3-8)

cooling power and adiabatic efficiency) based on the output of `ode15s`. The gap model uses the non-stiff `ode45` solver to integrate the coupled ODEs governing appendix gap heat transfer and fluid motion.

The gap model may be run as a stand-alone module by calling fpe_gap.m without guesses for $\dot{Q}_{\text{gap,net}}$ and $|dm_{\text{gap}}/dP|$; this causes the function to invoke MATLAB's `fsolve` method and iterate internally to convergence. When integrated into another program however (e.g., fpe_model.m), these guesses may be provided as inputs to the gap model. This allows a single iterative solver to adjust all five guess variables simultaneously (including the two for the gap model) instead of using nested solution loops; such nesting would require the gap model to reach convergence for each iteration of the expander model, and the numerical solution process of the inner gap loop could yield discontinuous derivatives which may hamper the convergence of the outer expander loop.

Similarly, fpe_model.m may be run as a stand-alone module by omitting the five guess variables, or may be integrated into a higher-level program such as a test case

coordinator which provides these guesses externally.

Test cases

With the floating piston expander model complete, several sets of simulations were run to examine the effect of various design parameters on the expander's performance; these sets are summarized in Table 3.4. All simulations used `fsolve` to solve for the constraints in the expander model (along with an additional constraint on $\dot{Q}_{\text{load}}$ as needed).

The first study (naïvely named "fpe_exploration" with no trailing version numbers) was based on a pure Monte Carlo approach: values for most inputs were selected pseudo-randomly based on either uniform or power-law probability distributions, and the corresponding outputs were recorded. The second study (fpe_exploration_b) began a series of attempts to obtain data more specific to the NASA ZBO cryocooler requirements, with the input temperature randomly specified as either 25 K or 100 K instead of being selected from a continuous probability distribution.

The remaining studies followed a slightly different paradigm: beginning with fpe_exploration_NASA2, the diameter was no longer specified as a free parameter, but instead varied by the solver to achieve a cooling load of either 20 W (for the low-temperature expander) or 100 W (for the high-temperature expander). The expander inlet temperatures were also reduced to 95% of the stage temperatures to reflect the imperfect heat transfer in the load heat exchangers, though no attempt was made to consider additional temperature defects in the recuperators. Additionally, the simulations alternated between the two expander configurations systematically instead of randomly.

The fpe_exploration_NASA3 study saw further modifications. Most notably, the current version of the expander model was used (and with it, the current definitions of

Table 3.4: Free variables and constraints adjusted in each expander study. Filled circles denote quantities that were varied across a continuous range independent of expander configuration, while hollow circles denoted configuration-specific parameters such as inlet temperature that chosen discretely based on particular expander configurations.

Study	f	δ_{gap}/D	T_{in}	P_{in}	$P_{\text{in}}/P_{\text{out}}$	L_{pis}/D	m_{aspect}	f_{low}	f_{high}	$V_{\text{cl}}/V_{\text{swept}}$	D	$\dot{Q}_{\text{load}}$	L_{pis}	S/D	f_{bi}, f_{bo}	t_{cl}/D
fpe_exploration	●	●	●	●	●	●	●	●			●					
fpe_exploration_b	●	●	○	●	●	●	●	●			●					
fpe_exploration_NASA2	●	●	○	●	●	●	●	●	●	●		○				
fpe_exploration_NASA3	●	●	○									○	●	●	●	●
fpe_exploration_NASA4	●	●	○	○								○	●	●	●	●
fpe_exploration_NASA5	●	●	○	○	○							○	●	●	●	●

● = Varied continuously independent of expander configuration
○ = Chosen discretely based on expander configuration

t_{cl}/D, S/D, and the blow-in and blow-out factors), and the expander inlet pressure and pressure ratio were fixed at 1.0 MPa and 10, respectively. Additionally, the gap width and piston length ranges were specified directly (instead of being specified as fractions of diameter) in order to better reflect manufacturing constraints on the expander. The variable ranges used by the Monte Carlo simulations were also adjusted, and a power law was used for all continuous probability distributions to yield evenly-distributed values on a logarithmic scale.

The fpe_exploration_NASA4 study was intended to explore lower-pressure-ratio expanders for the double-expander configurations discussed in Chapter 2, but was otherwise identical to fpe_exploration_NASA3. Four configurations were explored in this study:

- A 10 W, 25 K expander with a 1.0 MPa inlet and a 0.316 MPa outlet
- A 10 W, 25 K expander with a 0.316 MPa inlet and a 0.1 MPa outlet
- A 50 W, 100 K expander with a 1.0 MPa inlet and a 0.316 MPa outlet
- A 50 W, 100 K expander with a 0.316 MPa inlet and a 0.1 MPa outlet

Lastly, the fpe_exploration_NASA5 study examined all six previously-described expander configurations (two HPR and four LPR), but used a more structured approach than its precursors: instead of simultaneously sampling all design variables using continuous probability distributions, only one variable at a time was allowed to vary continuously and the rest were constrained to fixed values. The approach is illustrated graphically in Figure 3-14 for a simplified 2-D example.

The sampling method in fpe_exploration_NASA5 was chosen to address the difficulty of visualizing functions in more than three dimensions. While tools exist to aid in this endeavor (e.g., the Trade Space Visualizer developed at the Pennsylvania State University [ARL10], which was used to examine the results of earlier simulations),

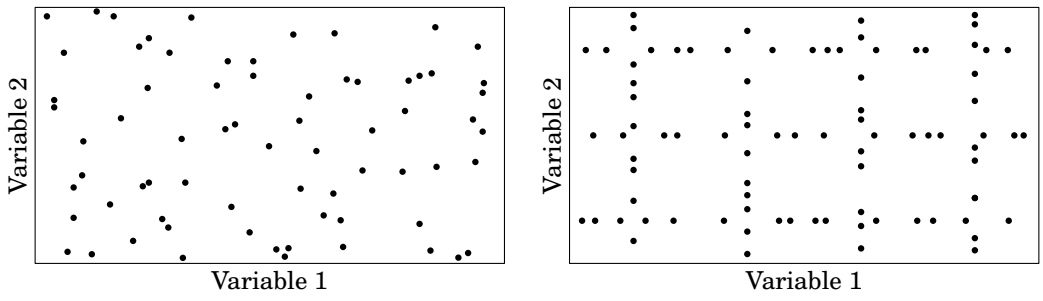

(a) Point "cloud" sampling **(b)** Hypergrid sampling

Figure 3-14: Sampling approaches used by (a) studies preceeding fpe_exploration_NASA5, and (b) the fpe_exploration_NASA5 study. Both subfigures depict 70 sample points, though the data shown here are hand-drawn and intended for illustration only (the actual studies used MATLAB's pseudo-random number generator function, `rand`, seeded from the system timer).

many first- and second-order interactions can be explored with simple 2-D contour plots. Such plots rely on human intuition to "fill in the gaps" between contour lines instead of explicitly examining the entire design space, but should give a good portrayal of the system's behavior provided there are no significant features hiding between adjacent contours. Of course, arbitrary contour plots could in theory be generated from the point clouds in earlier simulations, but fitting six-dimensional scattered data proves difficult in practice. The current approach is also more economical with computer resources than Monte Carlo sampling since only values to be plotted are simulated (though this comes at the expense of reduced flexibility; the contours cannot be arbitrarily changed post-simulation).

The choices of variable ranges and contours used for the fpe_exploration_NASA5 study are listed in Table 3.5; should more details be needed, the test code itself is reproduced in Appendix B.3.

Note that the design-space explorations described above all rely on random sampling. This approach permits an easy form of parallel computing: multiple instances of the same code may be run on several CPU cores or distinct computers to increase the data production rate with no need for coordination between code instances. Since a pseudo-random number generator was used to produce sample points, the success of this method is predicated on each instance having a different "seed".[9] In the present work, this was accomplished by seeding the pseudo-random number generator from the system timer and deliberately waiting for each instance of the code to begin processing before starting subsequent instances; the randomness introduced by such manual intervention makes it unlikely that instances will generate identical data.

[9]Notably, this is *not* the default behavior of MATLAB's `rand` function at the time of this writing.

Table 3.5: Continuous variable ranges, discrete values, and fixed parameters used in the fpe_exploration_NASA5 study. Recall that a power-law probability distribution is used for all continuous ranges (i.e., sample points are evenly distributed on a logarithmic scale between the limits shown). Discrete values are also pseudo-logarithmically spaced and sorted into five bins: very low ("VL"), low, nominal, high, and very high ("VH").

		Discrete values					
Variable	Range	VL	Low	Nominal	High	VH	Units
f	0.25–4.0		0.3	1.0	3.0		[Hz]
f_{bi}, f_{bo}	0.005–0.25		0.01	0.05	0.2		[]
L_{pis}	0.25–2.0		0.25	0.5	1.0	2.0	[m]
δ_{gap}	0.01–1.0	0.01	0.03	0.1	0.3	1.0	[mm]
t_{cl}/D	0.005–0.1		0.005	0.02	0.1		[]
S/D	0.05–2.0	0.1	0.2	0.5	1.0		[]
T_{warm}				300			[K]
t_{pis}/D				0.03			[]
t_{cyl}/D				0.01			[]
$\mathrm{mat}_{\mathrm{pis}}$				G10			–
$\mathrm{mat}_{\mathrm{cyl}}$				304 steel			–

3.3.4 Results & Discussion

The simulations from the fpe_exploration_NASA5 study yielded total of ~1 million valid data points with a runtime of approximately 4500 core-hours on middle-of-the-line computer hardware (circa 2012). As it would be infeasible to publish the entire dataset in paper form, only a small subset of the raw data is reproduced for reference in Appendix C; larger datasets may be produced by re-running the code itself.

Note that only results from the fpe_exploration_NASA5 study are shown and discussed. While earlier studies served to iteratively inform the choice of variables and variable ranges used in this study, their results add little to those of fpe_exploration_NASA5 and are therefore not reported here.

N.B.: The discussions below make heavy use of plots to illustrate trends in the data. In each plot, two design parameters are varied at once; all others are held constant at the "Nominal" values in Table 3.5.

Efficiency as a function of *S*/*D*

As expected, there is an optimum ratio of stroke length to diameter for all six expander configurations simulated. The optimum shifts as other design variables depart from their nominal values, though it rarely exceeds a value of 0.6 and is generally lower. The exception to this trend occurs only with very wide appendix gaps (on the order of 1 mm), where the optimum approaches $S/D = 1$ in all but the low-pressure LPR expanders and slightly exceeds it in the 25 K HPR expander as shown in Figure 3-15.

Physically, the presence of the shuttle heat transfer favors expanders with shorter strokes, as the shuttle loss is proportional to S^2. This may also explain why a lower mean expander pressure favors lower values of S/D as illustrated in Figure 3-16;

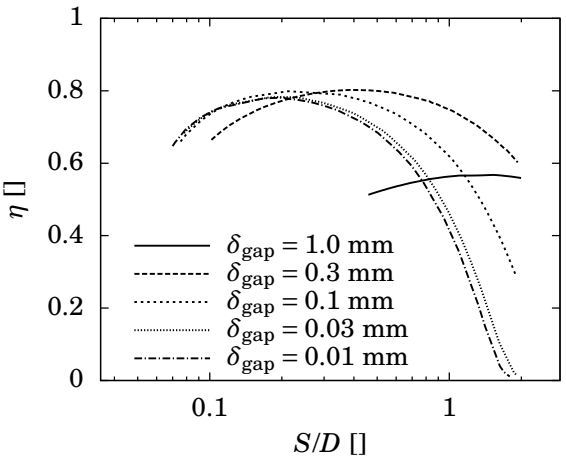

Figure 3-15: Influence of gap width on optimum S/D in a 25 K HPR expander. As the appendix gap is widened the importance of shuttle decreases (reducing the benefit of low S/D ratios) and the dead volume introduced by the appendix gap increases (favoring high S/D ratios with correspondingly larger ratios of swept volume to dead volume); the optimum therefore shifts toward a higher S/D.

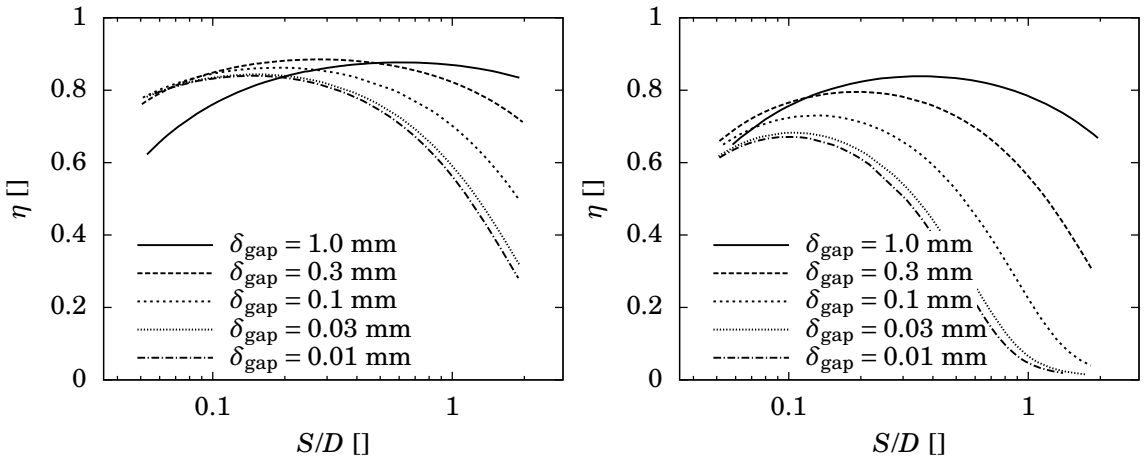

(a) High-pressure LPR expander **(b)** Low-pressure LPR expander

Figure 3-16: Comparison of optimum S/D in high- and low-pressure 100 K LPR expanders. Shuttle heat transfers play an important role in establishing the optimum S/D ratio; this likely explains why expanders with a lower mean pressure and correspondingly-larger diameters and stroke lengths favor slightly smaller values of S/D.

lower-pressure LPR expanders require a larger swept volume for the same amount of cooling as a result of the lower fluid density, and therefore suffer from an increased amount of shuttle heat transfer per unit cooling. While it is true that the larger surface area available for cyclic heat transfer should favor S/D ratios closer to unity, this appears to be outweighed by the effect of shuttle.

The effect of shuttle heat transfer is also reflected in the variation of the optimum S/D as a function of piston length (Figure 3-17a). For longer expanders, the reduced temperature gradient permits the use of a longer stroke, though the optima are still lower than 0.5 for the cases shown. Interestingly, the piston length affects the importance of the stroke length as well as its value; for short pistons, the optimum S/D is much more pronounced than for very long pistons, and the expander efficiency decays quickly with departures from the optimum value. A similar effect is visible in the impact of the operating frequency on the optimum S/D in Figure 3-17b; lower frequencies yield smaller optimum strokes and more pronounced peaks, as they yield expanders with larger diameters and stroke lengths and correspondingly higher shuttle heat transfers. In contrast, the amount of blow-in and blow-out does not seem to affect the position of the optimum, though larger values of f_{bi} and f_{bo} do broaden the width of the peak considerably for HPR expanders as typified in Figure 3-18.

The clearance fraction has a strong influence on the optimum S/D as illustrated in Figure 3-19. Larger clearance fractions favor higher stroke-to-diameter ratios, as this maximizes the ratio of swept volume to clearance volume (recall that the clearance was defined as having a thickness that scales with diameter; the ratio of swept volume to clearance volume is therefore directly proportional to S/D). For large clearances ($t_{\mathrm{cl}}/D = 0.1$), the efficiency begins to falls rapidly as the amount of swept volume approaches the amount of dead volume. The lack of data below this region suggests

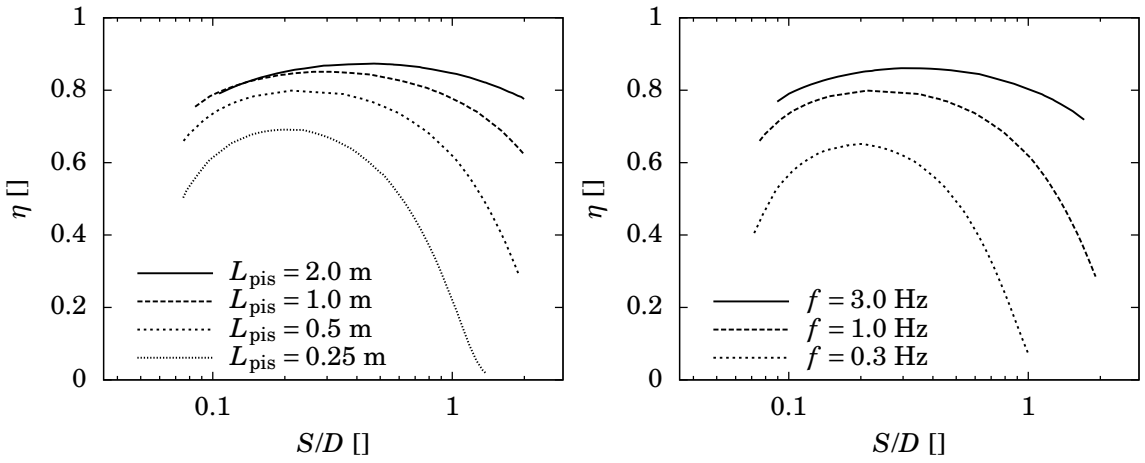

(a) Piston length effect on optimum S/D

(b) Frequency effect on optimum S/D

Figure 3-17: Influence of piston length and frequency on optimum S/D in a 25 K HPR expander. Shorter pistons and lower frequencies have nearly identical effects; both increase the importance of shuttle heat transfers (the former via an increased temperature gradient, the latter via the larger strokes and diameters required to achieve a suitable mass flow rate) and therefore both favor lower values of S/D and increase the importance of the optimum.

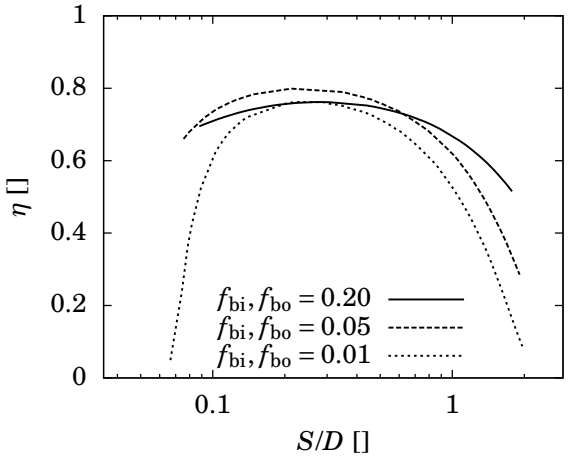

Figure 3-18: Influence of blow-in and blow-out factors on optimum S/D in a 25 K HPR expander. Increasing the amount of blow-in and blow-out has little effect on the optimum value of S/D, but does broaden the peak and decrease the impact of a suboptimal choice (especially for low values of S/D, where increased blow-in and blow-out reduce the amount of valuable stroke length that must be used for recompression).

that simulations with lower S/D failed to converge.

Efficiency as a function of appendix gap width

One of the key goals of this work was to develop a model of the appendix gap that captured the effects of large pressure-driven mass flows while remaining computationally efficient. The resulting expander performance curves demonstrate the key trends expected of such a model, typified by Figure 3-20. For very long expanders where the temperature gradient between the warm and cold ends is small, efficiency is optimized by using thin appendix gaps to reduce gas enthalpy transfer losses and expander dead volume. Conversely, for short expanders with higher temperature gradients, wider

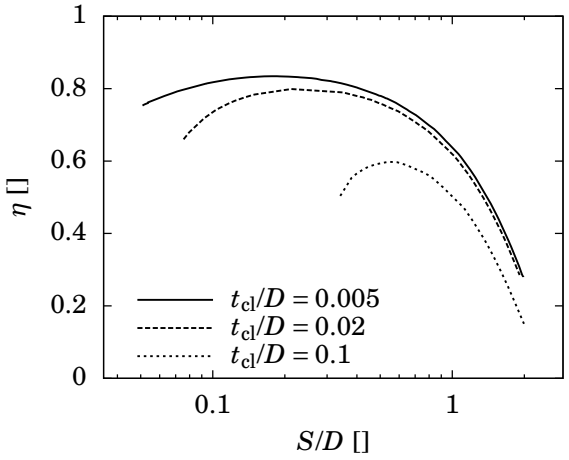

Figure 3-19: Influence of clearance fraction on optimum S/D in a 25 K HPR expander. Unsurprisingly, the longer recompression strokes required by larger clearance fractions favor larger values of S/D. The effect is particularly noticeable for $t_{cl}/D = 0.1$; efficiency falls off steeply below $S/D \simeq 0.4$ where a significant fraction of the swept volume must be devoted to recompression.

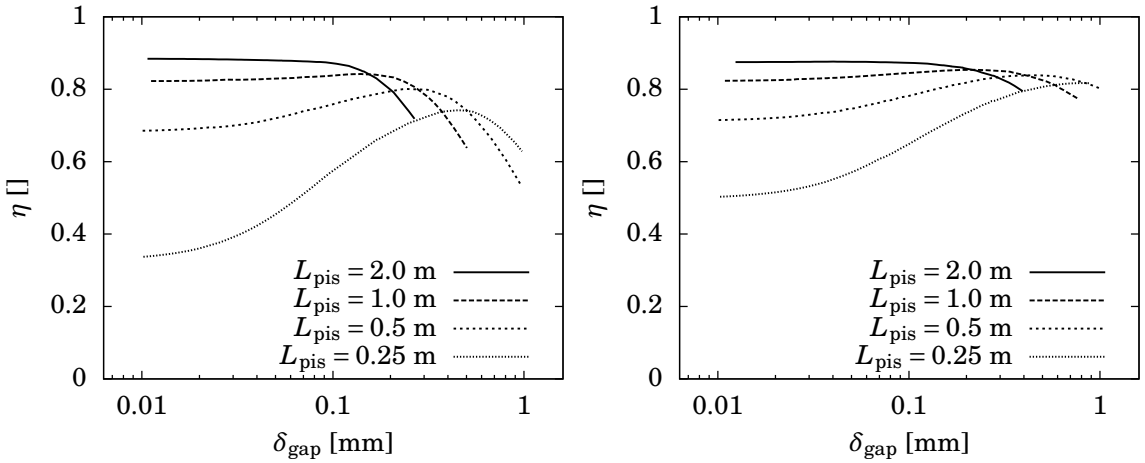

(a) 25 K HPR expander **(b)** 100 K HPR expander

Figure 3-20: Influence of piston length on optimum appendix gap width in HPR expanders. The gap-width optima arise from the tradeoff between shuttle heat transfers (which favor wide gaps) and a combination of gas enthalpy transfers and dead volume (which favor narrow gaps). A proper choice of gap width can largely mitigate the effect of shorter pistons, which emphasize the effect of shuttle due to their steeper temperature gradients and introduce less dead volume for a given gap cross section.

appendix gaps provide a way of mitigating shuttle heat transfer without adding too much dead volume or incurring excessive gas enthalpy transfers (which depend on the amount of gap mass flow and therefore on the gap volume in the absence of significant sealing), with the added benefit that they are easier to manufacture. Nevertheless, the predictions for particularly wide gaps should be treated with some distrust since the gap model assumes laminar fully-developed flow and has not been experimentally validated.

The operating frequency of the expander also affects the gap width optimum (Figure 3-21), with higher frequencies favoring smaller gaps. At least two physically-viable mechanisms may exist for this effect. First, higher frequencies should require a smaller working volume for a given heat load; with a fixed S/D, the stroke length

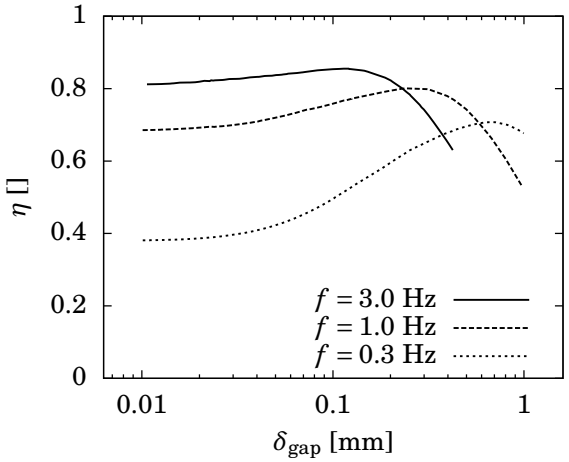

Figure 3-21: Influence of frequency on optimum gap width in a 25 K HPR expander. Higher-frequency expanders should have smaller diameters and strokes, thus reducing the impact of shuttle; the shift may also arise from the frequency-dependence of the gas enthalpy transfer (see equation (3.22)).

is correspondingly reduced and smaller gap sizes may be used before the increase in shuttle heat transfer outweighs the decrease in gas enthalpy transfer and dead volume. Second, the terms describing the effects of gas motion in the gap (from equation (3.22)) all depend on frequency either directly (ω) or indirectly via the bulk velocity amplitude $\overline{U}$, while the "pure" shuttle heat transfer loss is nearly independent of frequency when limited by conduction through the appendix gap fluid; as a result, higher frequencies may bias the optimum towards smaller gap sizes to reduce the impact of the gas enthalpy transfer.

As a result of the gap optimum being governed by the tradeoff between gas enthalpy transfer and shuttle (which in its pure form is proportional to the square of the stroke length), the stroke-to-diameter ratio also plays a significant role in determining the best choice of gap width as illustrated in Figure 3-22. Larger S/D ratios increase the relative importance of shuttle losses and shift the optimum towards wider gaps, while smaller ratios make it more difficult for shuttle to dominate and shift the optimum in favor of narrower gaps which reduce dead volume and gas enthalpy transfer. The lower S/D ratios make efficiency mostly insensitive to gap width below $\delta_{gap} \approx 0.1$ mm in the 25 K expander presumably because the impact of

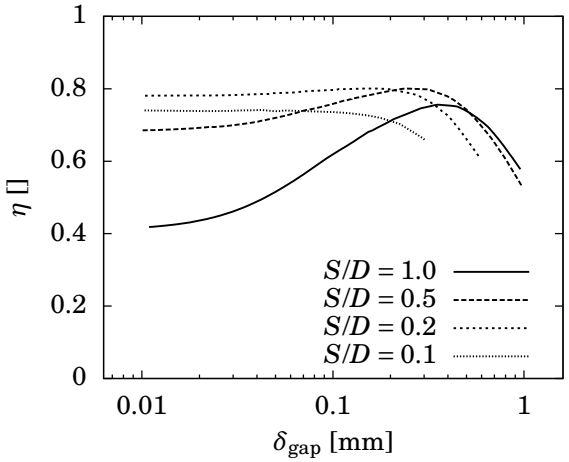

Figure 3-22: Influence of S/D ratio on optimum gap width in a 25 K HPR expander. Lower S/D ratios reduce the importance of shuttle heat transfer; they therefore favor smaller gaps which reduce gas enthalpy transfer and dead volume (though these losses also appear to be small below $\delta_{gap} \approx 0.1$ mm as inferred from the flattened $S/D = 0.1$ curve).

both shuttle and gas enthalpy transfer are small. A similar trend is visible in the 100 K expander (not shown) below $\delta_{\text{gap}} \approx 0.3$ mm.

The blow-in and blow-out factors had only a small effect on the optimum gap width in HPR expanders and an almost-negligible effect in LPR expanders, with higher factors favoring a marginally narrower gap (Figures 3-23 and 3-24; presumably this is a result of the shorter stroke lengths required when blow-in and blow-out are used). As expected, the HPR expanders and high-pressure LPR expanders also favored smaller gaps than the low-pressure LPR expanders which are more strongly affected by shuttle heat transfers. The clearance fraction had almost no effect on the optimum gap width in the expanders examined, though narrow gaps were slightly more detrimental to performance when the clearance fraction was larger (Figure 3-25).

Efficiency as a function of piston length

In contrast to the clear optima which exist for stroke-to-diameter ratio and appendix gap thickness, the effect of piston length was typically monotonic in the simulations conducted, with longer pistons yielding more efficient expanders. This is no surprise: long pistons reduce the temperature gradient between the warm and cold end, mitigating the shuttle heat transfer which seems to play a large role in the performance of these machines.

One particularly strong exception to the longer-is-better trend is demonstrated in Figure 3-26. The optimum piston length becomes much shorter when very wide gaps are used, to the point that a 0.25 m expander becomes optimal for the 100 K HPR expander (with a surprisingly small impact on the efficiency, provided the gap model still yields reasonable results at such large gap widths). Physically, wider appendix gaps mitigate the effect of shuttle at the expense of increased gas enthalpy transfer and increased dead volume, driving the design toward shorter pistons with higher temperature gradients but smaller appendix gap volumes.

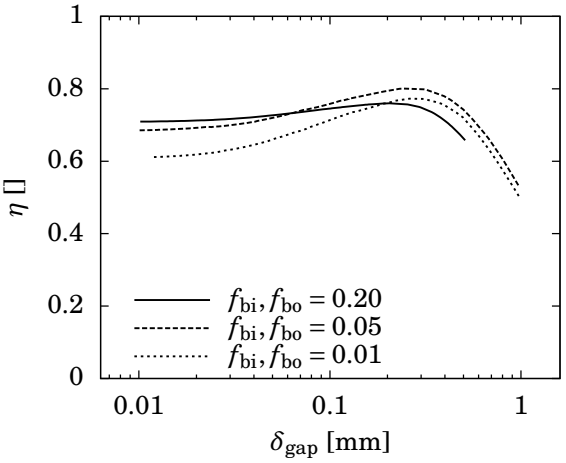

Figure 3-23: Influence of blow-in and blow-out factors on optimum appendix gap width in a 25 K HPR expander. Only a small effect is visible, with more blow-in and blow-out favoring narrower gaps. This may results from a reduction in the required swept volume and a corresponding decrease in the importance of shuttle.

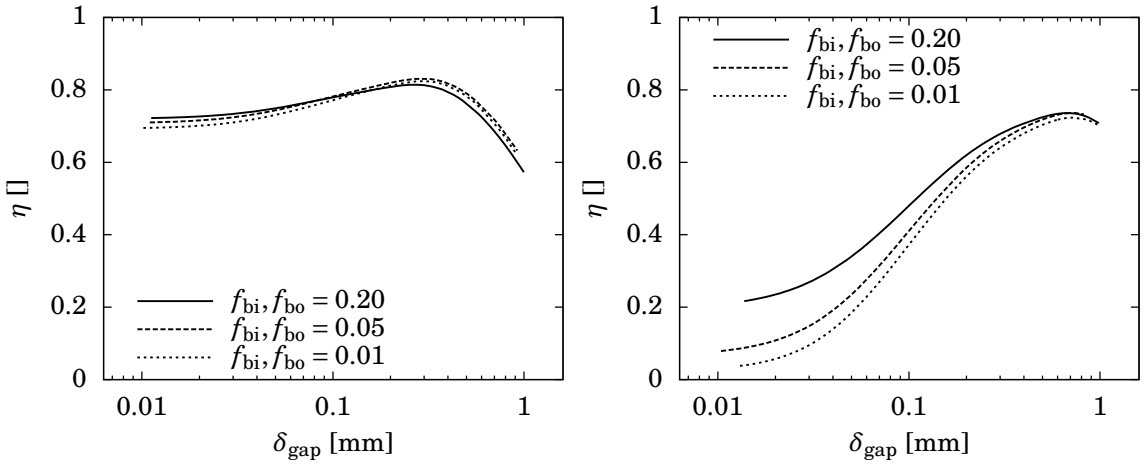

(a) High-pressure LPR expander **(b)** Low-pressure LPR expander

Figure 3-24: Influence of mean pressure and blow-in and blow-out factors on optimum appendix gap width in 25 K LPR expanders. Unlike in the HPR expanders, the factors have almost no influence on optimum gap width. The mean pressure, however, does have an effect: wider gaps are optimal in the low-pressure expander, presumably because its larger swept volume makes it more susceptible to the effects of shuttle heat transfer.

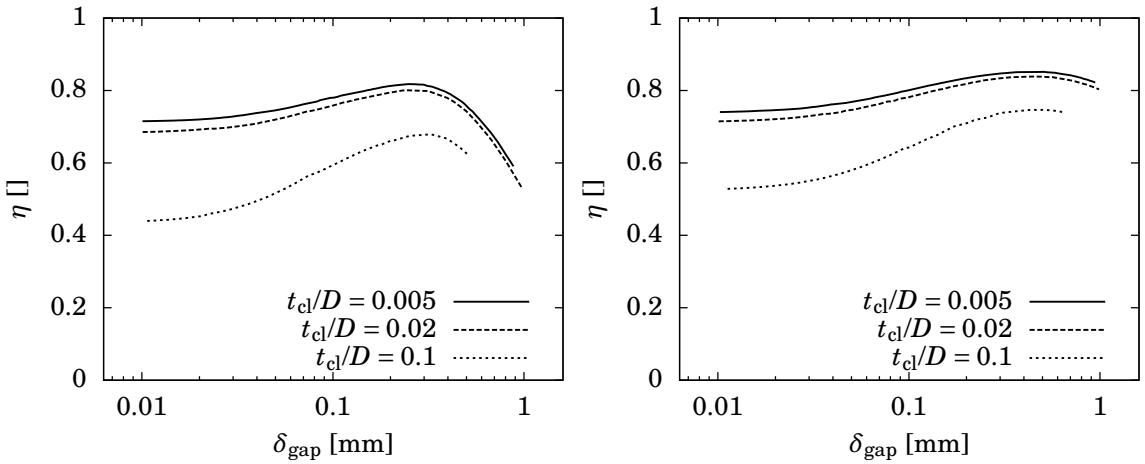

(a) 25 K HPR expander **(b)** 100 K HPR expander

Figure 3-25: Influence of clearance fraction and expander configuration on optimum appendix gap width in HPR expanders. Clearance fraction has essentially no effect on the optimum appendix gap width, though higher values increase the impact of suboptimal gaps. The optimum appendix gap width is smaller in the 20 W, 25 K expander than in the 100 W, 100 K expander. The reason is unknown, though the different slopes of the efficiency curves for gaps wider than the optimum suggest that gas enthalpy transfer or gap dead volume have a stronger effect in the 25 K configuration.

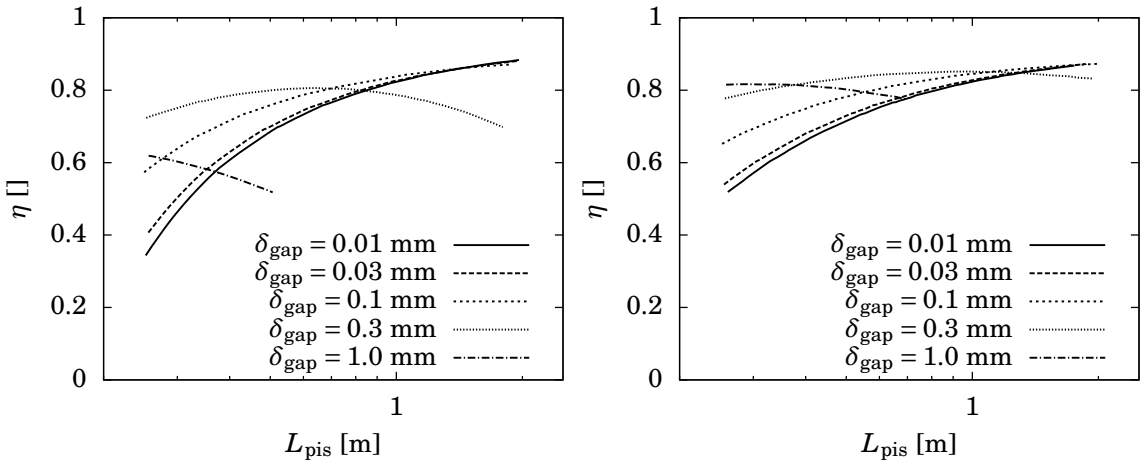

(a) 25 K HPR expander **(b)** 100 K HPR expander

Figure 3-26: Influence of appendix gap width on optimum piston length in HPR expanders. Longer pistons are typically better, though wide gaps favor intermediate or even short pistons (presumably to mitigate their larger gas enthalpy transfers and added dead volumes). Accordingly, the choice of gap width can largely offset the impact of a short piston, especially in the 100 K expander. Note that this same trend is visible from Figure 3-20.

Another more subtle exception is visible in the 25 K HPR expander as shown in Figure 3-27a. At a frequency of 3 Hz, the optimum length is reduced to about 0.96 m, presumably due to the increased importance of gas enthalpy transfer and the reduced importance of shuttle at higher frequencies, and the impact of length on efficiency is reduced dramatically. The shift is also present for the lowest S/D ratio (Figure 3-27b) and the highest blow-in and blow-out factors (Figure 3-27c), where the efficiency's sensitivity to piston length is greatly reduced and the optimum length shifts below 2 m. Higher clearance fractions also reduce the sensitivity of efficiency to piston length, but without an apparent shift in optimum (Figure 3-27d).

Higher frequencies similarly reduce the efficiency's sensitivity to length in LPR expanders (Figure 3-28). While a reduced piston length optimum is visible in the high-pressure expander, though, the best performance in the low-pressure expander was always obtained with the longest pistons simulated ($L_{pis} = 2$ m). The tendency towards longer pistons is this configuration is likely a result of the larger swept volume required at lower mean pressures and, consequently, the increased impact of shuttle heat transfer.

Efficiency as a function of clearance fraction

While all other geometric variables in this study had non-trivial optima in at least some circumstance, the clearance fraction was unconditionally detrimental to expander performance for all the cases examined, albeit with varying degrees of severity. In the HPR expanders, high clearance fractions were more hurtful in combination

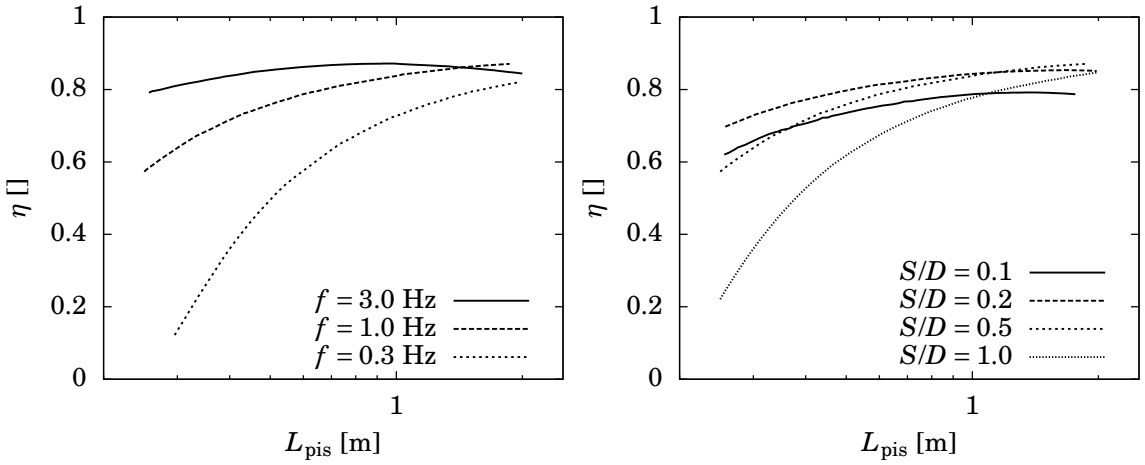

(a) Influence of frequency

(b) Influence of S/D ratio

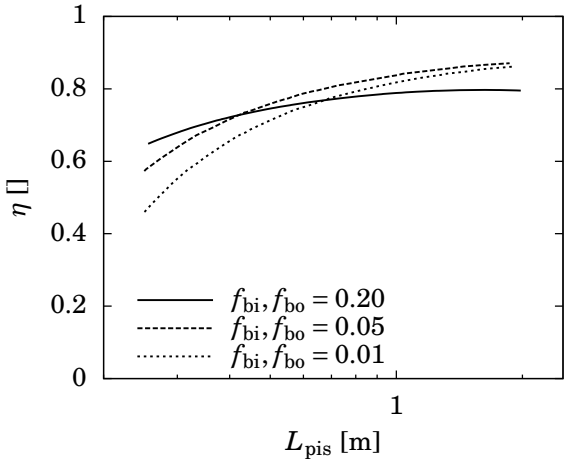

(c) Influence of blow-in/blow-out

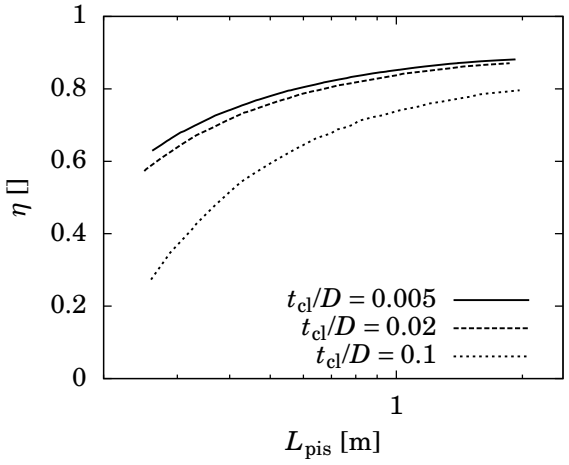

(d) Influence of clearance fraction

Figure 3-27: Influence of frequency, S/D, blow-in and blow-out, and clearance fraction and on optimum piston length in a 25 K HPR expander. The efficiency's sensitivity to length is reduced by higher frequencies, lower S/D ratios, higher blow-in/blow-out fractions, and lower clearance fractions (though note that this trend may change in expanders substantially different than those here and should not be applied indiscriminately). For extreme values of all but the clearance fraction, the optimum piston length shifts below the maximum of 2 m, if only slightly.

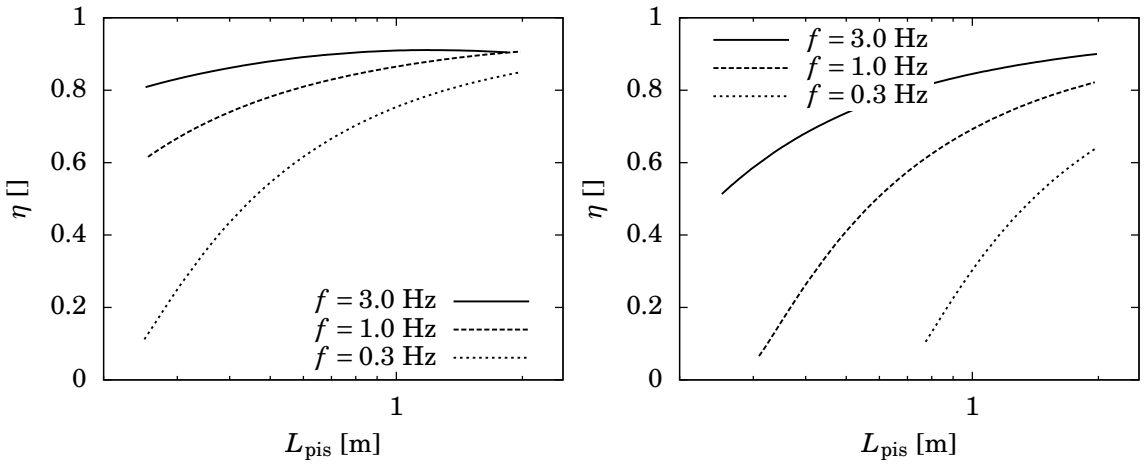

(a) High-pressure LPR expander **(b)** Low-pressure LPR expander

Figure 3-28: Influence of frequency on optimum piston length in 25 K LPR expanders. The trend is similar to that in the corresponding HPR expander (Figure 3-27a), with higher frequencies reducing the sensitivity of efficiency to piston length. For the low-pressure expander, however, the need for increased swept volume increases the impact of shuttle, preventing the appearance of an optimum below L_{pis} = 2 m and requiring longer pistons to match the efficiency of the high-pressure and HPR configurations.

with low frequencies, short pistons, and to a much lesser extent, narrow appendix gaps (Figures 3-29a–c), suggesting appendix gap losses played a significant role. The most dramatic increase in sensitivity, however, occurred with small blow-in and blow-out fractions (Figure 3-29d).

Since variations in blow-in and blow-out demonstrated the effect the most, a separate study was conducted to observe the influence of these variables with large clearance volumes. The results as summarized in Table 3.6. The study indeed pointed to appendix gap heat transfer as the cause of the increased sensitivity; at a clearance fraction of 0.062 and $f_{bi} = f_{bo} = 0.01$, the 25 K HPR expander experienced an appendix gap heat transfer of 17.8 W, nearly four times the value at $f_{bi} = f_{bo} = 0.2$. The higher loss stems from an increased diameter and stroke length, and these in turn arise from the increased fraction of the stroke that must be devoted to recompression at low blow-in and blow-out fractions. Further compounding this is a positive feedback loop

Table 3.6: Effect of blow-in and blow-out on expander geometry and appendix gap losses. Values are for the 25 K HPR expander configuration with a clearance fraction of 0.062 and a range of f_{bi} and f_{bo} choices; other design variables were held constant at their nominal values.

f_{bi} & f_{bo}	D [mm]	S [mm]	$\dot{Q}_{gap,net}$ [W]
0.01	80.8	40.4	17.8
0.05	66.2	33.1	10.0
0.2	51.1	25.5	4.7

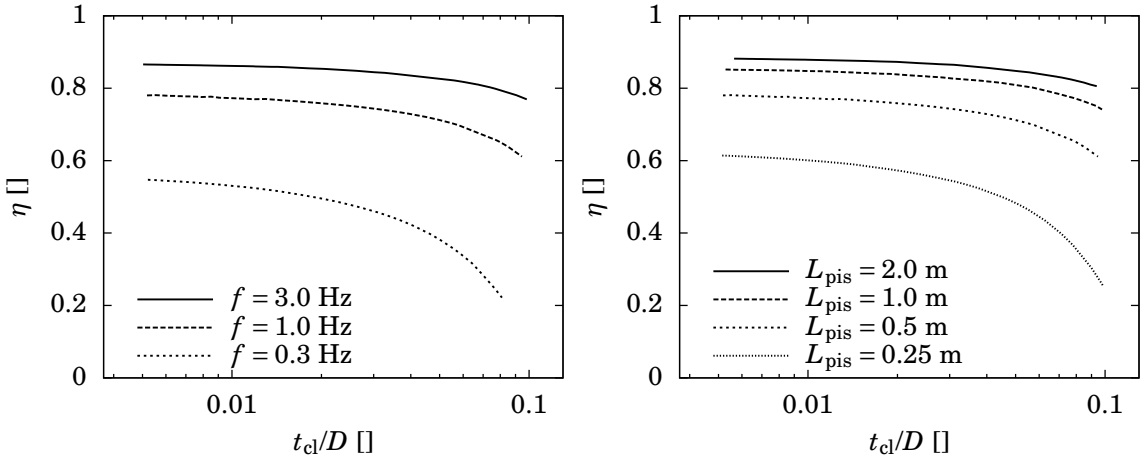

(a) Influence of frequency

(b) Influence of piston length

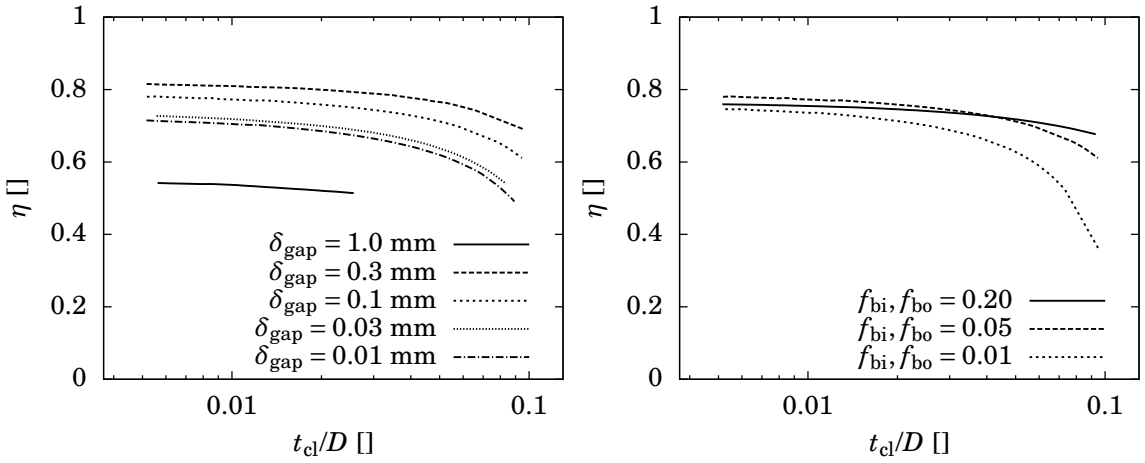

(c) Influence of gap width

(d) Influence of blow-in/blow-out

Figure 3-29: Influence of frequency, piston length, appendix gap width, and blow-in/blow-out on impact of clearance fraction in a 25 K HPR expander. The detriment of large clearance fractions is increased by lower frequencies, shorter pistons, smaller appendix gaps, and most of all, by less blow-in and blow-out. These trends suggest appendix gap losses as a probably cause, a hypothesis verified for the blow-in and blow-out dependence (see Table 3.6).

between the swept volume and the appendix gap losses: larger strokes or diameters increase the gap losses in an expander, which necessitates even larger swept volumes in order to meet the required cooling power, *et cetera*.

The effects above were also visible in the LPR expanders, if strongly muted in comparison (e.g., Figure 3-30). Interestingly, the blow-in and blow-out fractions which had such a strong effect in the HPR expander had almost no effect in the high-pressure LPR expanders, though no explanation is put forward in the present work.

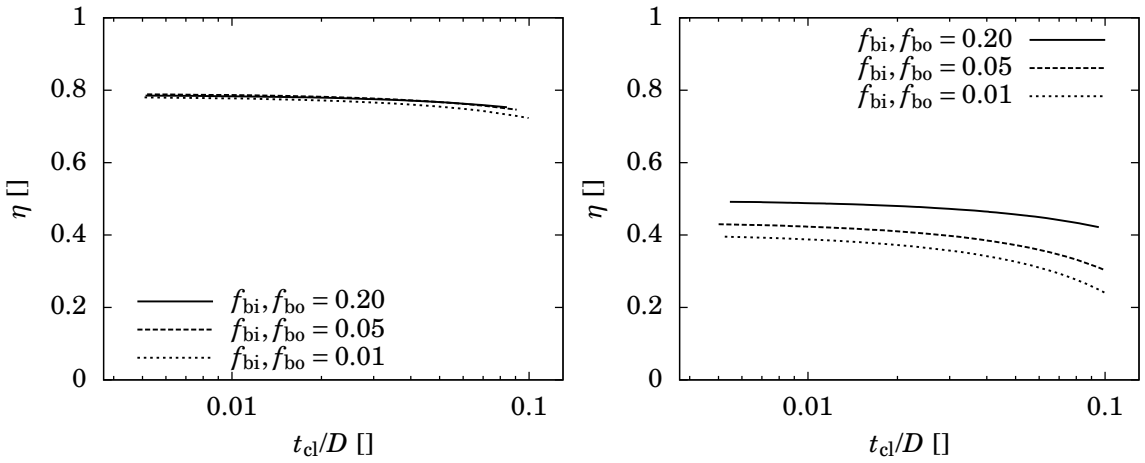

(a) High-pressure LPR expander **(b)** Low-pressure LPR expander

Figure 3-30: Influence of blow-in/blow-out factors on impact of clearance fraction in 25 K LPR expanders. The penalty of larger clearance fractions is still greater when the blow-in and blow-out factors are reduced, though almost insignificantly for the high-pressure configuration and in both cases much less than in the 25 K HPR expander (Figure 3-29d).

Efficiency as a function of blow-in and blow-out fraction

The results of the clearance study above highlight one of the more unexpected (albeit physically straightforward) conclusions of this work: blow-in and blow-out can be highly beneficial to an expander's performance under the right operating conditions. This is most strongly illustrated by Figure 3-31, which plots efficiency as a function of f_{bi} and f_{bo} for a range of clearance fractions. Not only are clear optima visible, but for large clearance fractions, the choice of blow-in and blow-out fractions can make the difference between an expander with 25% adiabatic efficiency (when blow-in and blow-out are minimized) and one with 68% adiabatic efficiency (when optimal values are used).

For smaller clearance fractions, the results in Figure 3-31 show that there is

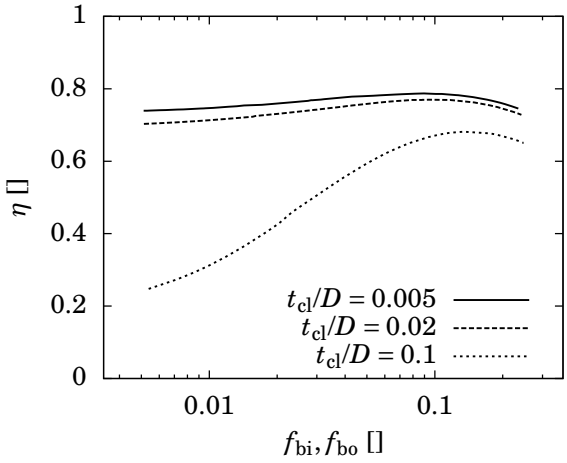

Figure 3-31: Influence of clearance fraction on optimum blow-in/blow-out fraction in a 25 K HPR expander. The existence of an optimum is one of the more unexpected conclusions of the present work, but stems from a simple physical cause: blow-in and blow-out permit shorter stroke lengths and diameters, reducing appendix gap losses and yielding a net efficiency gain for moderate f_{bi} and f_{bo}.

considerable flexibility in the choice of f_{bi} and f_{bo}; this translates to relaxed design requirements for the warm-end reservoir pressures. Furthermore, the preferred fraction of $f_{bi} = f_{bo} \simeq 0.09$ for both HPR expanders seems quite achievable, corresponding to high and low warm-end reservoir pressures around $P_A = 0.92$ MPa and $P_D = 0.18$ MPa, respectively.

The optimum f_{bi} and f_{bo} in HPR expanders seems to be influenced most by the operating frequency and length of the expander as shown in Figures 3-32a and 3-32b. Lower frequencies and shorter pistons favor larger amounts of blow-in and blow-out, presumably for the same reason that they favor shorter stroke-to-diameter ratios: the

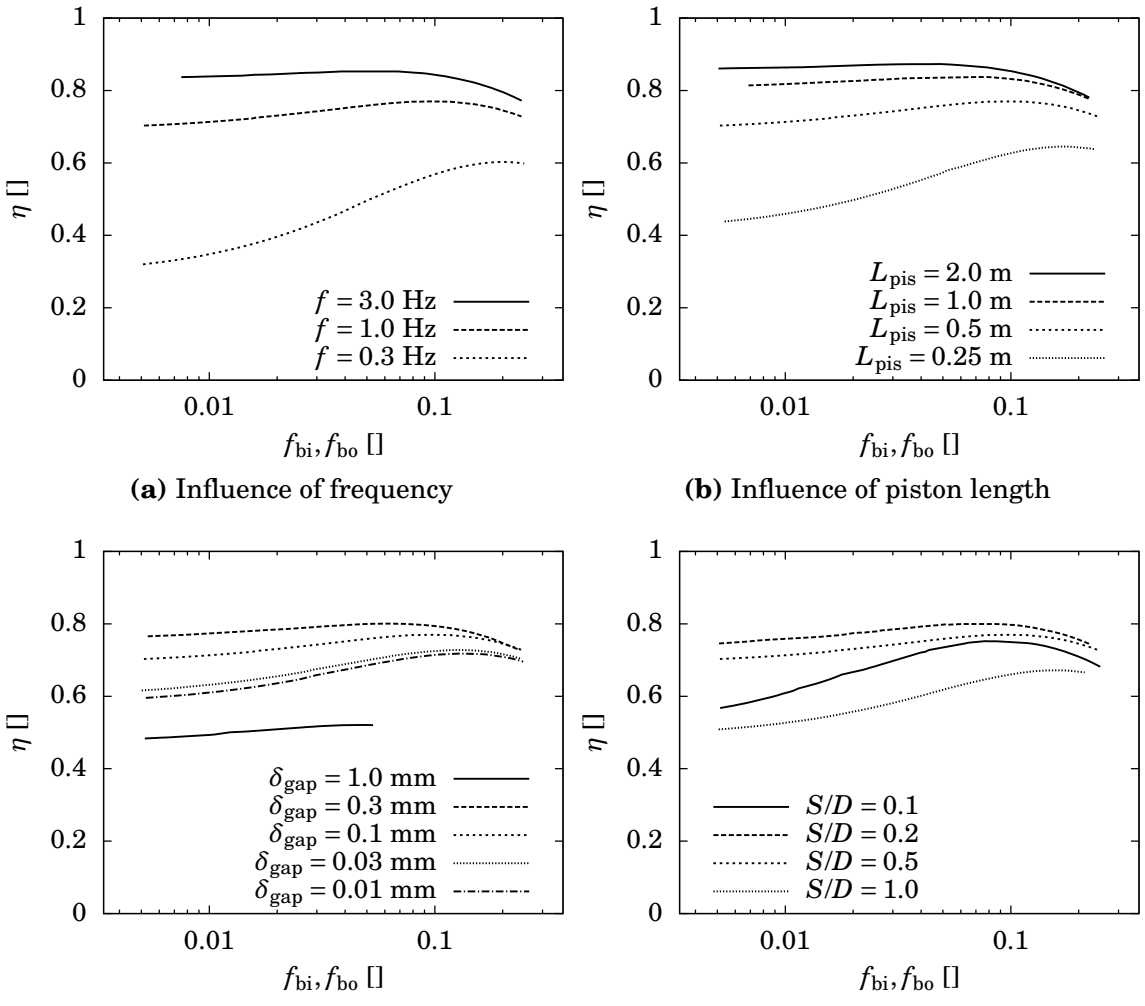

(a) Influence of frequency

(b) Influence of piston length

(c) Influence of gap width

(d) Influence of S/D ratio

Figure 3-32: Influence of frequency, piston length, appendix gap width, and S/D ratio on optimum blow-in and blow-out fractions in a 25 K HPR expander. Higher values of f_{bi} and f_{bo} are preferred when shuttle heat transfer is more prevalent, that is, for designs with lower operating frequencies, shorter pistons, narrower appendix gaps, and larger stroke-to-diameter ratios. One small exception to this trend occurs at $S/D = 0.1$, which favors slightly more blow-in and blow-out than $S/D = 0.2$.

impact of shuttle heat transfer is larger. The dependence of the optimum on appendix gap width and S/D also reflect this (Figures 3-32c and 3-32d), with thin gaps and higher S/D both favoring larger f_{bi} and f_{bo}.

In high-pressure LPR expanders, the behavior is qualitatively similar to that above but the sensitivity of efficiency to f_{bi} and f_{bo} is much lower (e.g., Figure 3-33a). The sensitivity is not quite as low in the low-pressure LPR expanders, but the optima themselves are shifted to larger values (e.g., Figure 3-33b). This may be due in part to the larger strokes and diameters typical of those expanders which further increase the importance of shuttle losses, though the definitions of the f_{bi} and f_{bo} factors may also play a role: the pressure differences driving both blow-in and blow-out were assumed to scale with the total pressure difference across the expander, and the effects of this scaling have not been considered in much detail in the present work.

Efficiency as a function of operating frequency

Given the importance of shuttle heat transfer in the results already discussed, it is unsurprising that higher operating frequencies typically yielded higher efficiencies; for a fixed cooling power, increasing f permits the use of a smaller working volume, which in turn reduces shuttle heat transfers. Exceptions do exist though: wide appendix gaps (Figure 3-34), very long pistons (Figure 3-35a), and a low S/D (Figure 3-35b) all shifted the optimum frequency away from the maximum simulated value of 4 Hz, presumably because they reduce the relative importance of shuttle compared to that of gas enthalpy transfer or other frequency-dependent losses. Conversely, changes that

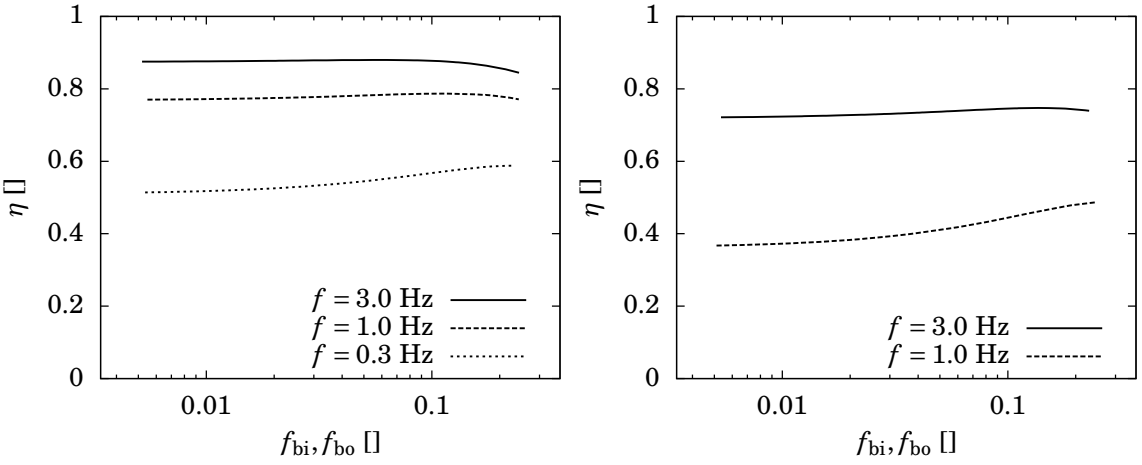

(a) High-pressure LPR expander **(b)** Low-pressure LPR expander

Figure 3-33: Influence of mean pressure and frequency on optimum blow-in and blow-out fractions in 25 K LPR expanders. Both high- and low-pressure LPR configurations display similar trends to those in the HPR expander, though the optima are less prominent. In the low-pressure expander, the optima also occur at higher values of f_{bi} and f_{bo}; this may result from the increased importance of shuttle in the low-pressure configuration, though the definitions of the blow-in and blow-out factors themselves may also play a role.

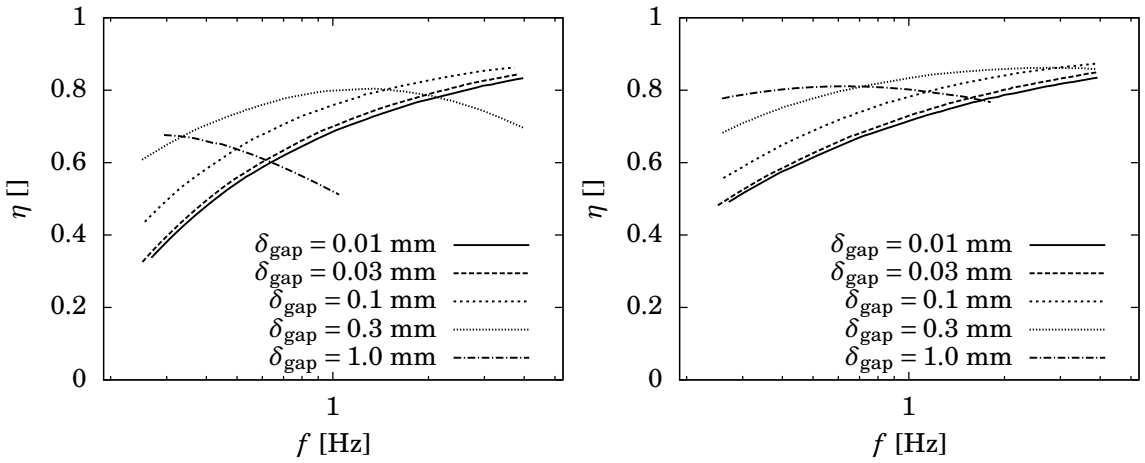

(a) 25 K HPR expander **(b)** 100 K HPR expander

Figure 3-34: Influence of appendix gap width on optimum operating frequency in HPR expanders. Higher frequencies are beneficial except when wide appendix gaps increase the importance of gas enthalpy transfers.

favor increased shuttle (such as narrower gaps, shorter pistons, higher S/D ratios, lower blow-in and blow-out factors, and larger clearance fractions) tended to increase the importance of high operating frequencies.

Of course, additional considerations such as valve timing, piston inertia, and warm-end reservoir behavior may place a practical limit on the frequency of floating piston expanders. The inclusion of valve losses may also alter the trends described above, though it seems most likely that they would *increase* the benefit of high frequencies: since high-frequency expanders are typically more efficient, the expander mass flow rates required to cool a given load (and the attendant valve losses) are expected to be lower than those in low-frequency expanders.

Higher-order interactions and design tables

The discussions above highlight numerous first-order interactions between design variables, but do not address any higher-order interactions that may arise when more than two variables depart from their nominal values simultaneously. Such higher-order interactions were not examined with the same amount of detail as the first-order interactions above; instead, the analysis in this section focused only on the most efficient expanders obtainable with a given set of design constraints. These expander designs are presented in Tables 3.7 and 3.8. Higher-order interactions were only explored for the two HPR expander configurations.

The first row in each of the two tables was generated by pruning the simulation dataset to retain points where all design variables were at their nominal values "or easier" (that is, with an operating frequency of 1 Hz or less, a gap width of 0.1 mm or greater, and so on), and recording the efficiency and design variables of

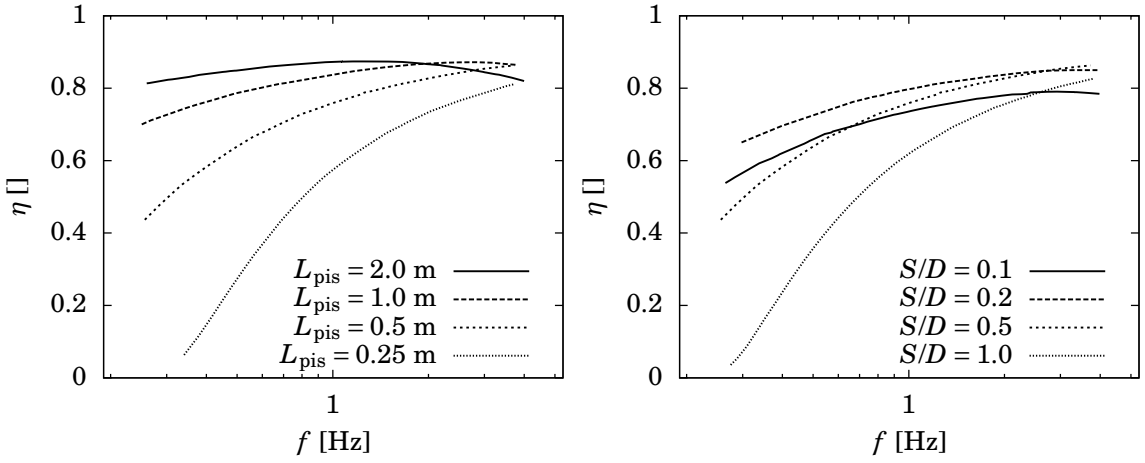

(a) Influence of piston length

(b) Influence of S/D ratio

(c) Influence of blow-in/blow-out

(d) Influence of clearance fraction

Figure 3-35: Influence of piston length, S/D, blow-in and blow-out, and clearance fraction and on optimum operating frequency in a 25 K HPR expander. Higher frequencies typically improved performance for the expanders in this work, presumably by yielding smaller working volumes which in turn reduce the amount of shuttle heat transfer. The trend is more pronounced with shorter pistons, larger S/D ratios, reduced f_{bi} and f_{bo}, and larger clearance fractions, all of which tend to aggravate shuttle; conversely, very long pistons and low values of S/D deemphasize shuttle and shift the optimum frequency away from the upper limit of the design space.

Table 3.7: Best efficiencies attainable by relaxing design constraints in the 25 K HPR expander. Simulated efficiencies ranged from 80.2% for the most manufacturable design (top row) to 92.5% for the least manufacturable design (bottom row). Note that S/D rarely falls outside the range of 0.2–0.5. *(To reduce visual clutter, nominal values are printed in gray.)*

Variables with relaxed constraints							
f [Hz]	f_{bi}, f_{bo} []	L_{pis} [m]	δ_{gap} [mm]	t_{cl}/D []	D [mm]	S/D []	η_{max} []
1.0	0.05	0.5	*0.300**	0.02	67.6	0.39	80.2
1.0	0.05	0.5	*0.162**	0.005	77.0	0.20	83.6
1.0	0.05	1.0	0.1	0.02	69.9	0.29	85.1
1.0	*0.050**	1.0	0.030	0.02	77.7	0.20	85.1
1.0	*0.058**	1.0	0.010	0.02	75.2	0.20	85.3
3.0	0.05	0.5	0.1	0.02	48.2	0.30	86.1
2.8	0.05	1.0	0.1	0.02	42.3	0.50	87.2
1.0	0.05	1.0	0.1	0.005	70.9	0.24	87.2
1.0	0.041	1.0	0.1	0.005	77.3	0.20	87.2
3.0	0.035	1.0	0.1	0.02	43.1	0.50	87.3
1.0	0.05	2.0	0.1	0.02	59.6	0.47	87.3
1.2	0.05	2.0	0.1	0.02	55.2	0.50	87.4
1.0	0.05	1.0	0.030	0.005	73.8	0.18	87.7
3.0	0.05	0.5	0.1	0.005	46.2	0.29	87.8
1.0	0.05	1.0	0.010	0.005	75.7	0.16	87.9
2.7	0.05	1.0	0.1	0.005	41.4	0.50	88.1
3.0	0.05	0.5	0.058	0.005	50.7	0.20	88.1
3.0	0.036	1.0	0.1	0.005	41.6	0.50	88.4
1.0	0.05	2.0	0.1	0.005	64.1	0.36	88.4
1.0	0.010	2.0	0.1	0.005	73.0	0.32	88.5
1.0	0.05	2.0	0.030	0.02	63.7	0.31	88.9
3.0	0.05	1.0	0.030	0.02	44.4	0.31	89.2
3.0	0.05	1.0	0.010	0.02	47.6	0.24	89.2
1.0	0.05	2.0	0.030	0.005	65.4	0.25	90.4
1.0	0.030	2.0	0.030	0.005	73.0	0.20	90.5
1.0	0.05	2.0	0.013	0.005	69.1	0.20	90.6
3.0	0.05	1.0	0.030	0.005	48.1	0.21	90.7
3.0	0.033	1.0	0.030	0.005	50.5	0.20	90.9
3.0	0.05	1.0	0.010	0.005	47.2	0.21	90.9
3.0	0.027	1.0	0.010	0.005	49.6	0.20	91.1
3.0	0.05	2.0	0.030	0.02	41.2	0.37	91.2
3.0	0.05	2.0	0.019	0.02	36.0	0.50	91.3
3.0	0.029	2.0	0.030	0.02	38.0	0.50	91.4
3.0	0.05	2.0	0.030	0.005	41.5	0.32	92.2
3.0	0.010	2.0	0.030	0.005	47.5	0.27	92.4
3.0	0.010	2.0	0.021	0.005	51.9	0.20	92.5

(easier) ↑ ↓ (harder)

* These are *easier* to achieve than the nominal values

Table 3.8: Best efficiencies attainable by relaxing design constraints in the 100 K HPR expander. Simulated efficiencies ranged from 83.9% for the most manufacturable design (top row) to 91.5% for the least manufacturable design (bottom row). Note that S/D rarely falls outside the range of 0.2–0.5. *(To reduce visual clutter, nominal values are printed in gray.)*

Variables with relaxed constraints							
f [Hz]	f_{bi}, f_{bo} []	L_{pis} [m]	δ_{gap} [mm]	t_{cl}/D []	D [mm]	S/D []	η_{max} []
1.0	0.05	0.5	*0.443**	0.02	104.1	0.50	83.9
1.0	0.05	1.0	*0.218**	0.02	102.3	0.50	85.4
1.0	0.05	0.5	*0.300**	0.005	117.4	0.29	85.5
3.0	0.05	0.5	*0.191**	0.02	69.6	0.50	87.0
1.0	0.05	1.0	0.1	0.005	116.9	0.26	87.1
1.0	0.05	2.0	0.1	0.02	103.8	0.44	87.3
1.0	0.031	2.0	0.1	0.02	102.5	0.50	87.4
1.0	0.05	2.0	0.030	0.02	102.7	0.36	87.8
3.0	0.05	1.0	0.1	0.02	69.0	0.49	88.3
3.0	0.05	0.5	0.1	0.005	79.7	0.27	88.3
3.0	0.05	1.0	0.030	0.02	73.4	0.33	88.5
1.0	0.05	2.0	0.1	0.005	105.3	0.38	88.5
3.0	0.031	1.0	0.1	0.02	71.2	0.50	88.5
3.0	0.05	2.0	0.1	0.02	60.8	0.74	89.2
1.0	0.05	2.0	0.030	0.005	104.7	0.30	89.2
3.0	0.05	1.0	0.1	0.005	74.7	0.36	89.3
3.0	0.031	2.0	0.1	0.02	74.7	0.50	89.4
3.0	0.031	1.0	0.1	0.005	68.3	0.50	89.5
3.0	0.05	1.0	0.030	0.005	74.3	0.28	89.8
3.0	0.030	1.0	0.030	0.005	86.6	0.20	89.9
3.0	0.05	2.0	0.1	0.005	64.1	0.60	89.9
3.0	0.025	2.0	0.1	0.005	72.8	0.50	90.3
3.0	0.05	2.0	0.032	0.02	62.5	0.50	90.4
3.0	0.028	2.0	0.030	0.02	64.8	0.50	90.7
3.0	0.05	2.0	0.030	0.005	66.2	0.38	91.3
3.0	0.026	2.0	0.030	0.005	62.5	0.50	91.5

(easier) ▲ ▼ (harder)

* These are *easier* to achieve than the nominal values

the *most efficient* point in the pruned data. The remaining rows were generated by systematically relaxing these constraints and recording the most efficient design for each permutation. For the frequency, blow-in and blow-out fractions, and clearance fraction, this equated to removing the constraint entirely. For the piston length and gap width, the constraints were either removed entirely or replaced with looser "intermediate" constraints ($L_{pis} \leq 1$ m or $\delta_{gap} \geq 0.03$ mm) to fill the void between the nominal values and the most difficult. This yielded a total of 72 permutations, though some of these yielded identical solutions since not all constraints were binding all the time (these duplicates are only reported once in the tables, yielding fewer than 72 rows).

Tables 3.7 and 3.8 are included in this thesis primarily as a design reference for

the 25–100 K ZBO cryocooler and as a starting point for further analysis. Some higher-level trends are also visible directly from the data; for example, most of these high-performance expander design have S/D ratios between 0.2 and 0.5. Overall, however, these tables volunteer a limited amount of insight and persuading them to reveal more was not a focus of the present work. One study was nevertheless undertaken to quantify the typical impact of each design constraint (including the intermediate constraints for L_{pis} and δ_{gap}): the constraints were each assigned an efficiency cost, and the costs were varied using gradient-based optimization to best fit the simulated efficiencies. The results illuminate some patterns in the data, but also hide all variations due to higher-order interactions and are not intended replace proper design simulations.

The results of the constraint study (Table 3.9) suggest typical improvements of 1–3% from relaxing most binding constraints. A notable exception is found in the blow-in and blow-out factors, which typically offer little benefit when reduced. There is also little benefit to allowing appendix gap widths smaller than 0.03 mm; the impact on efficiency amounts to less than 0.1 points on average for the 25 K HPR expander, and seems to never be optimal in the 100 K HPR expander. Both conclusions are reflected in Tables 3.7 and 3.8, where the benefits of reduced blow-in/blow-out factors and 0.01 mm gap widths never exceed ~0.2 and ~0.4 points (respectively) in otherwise-identical configurations.

Note that the values in Table 3.9 only apply when constraints are binding. For example, allowing 0.03 mm appendix gaps in the 100 K expander yields an average benefit of 0.78 points; however, narrow gaps are never optimal when the piston is only 0.5 m long. The gap-width constraint is therefore not binding and relaxing it will have

Table 3.9: Approximate efficiency benefits of relaxing *binding* manufacturing constraints in HPR expanders. The impact of each constraint (and the efficiency of the nominal configuration with no constraints relaxed) were chosen to best fit the simulated efficiencies in Tables 3.7 and 3.8.

	Configuration		
	25 K HPR	100 K HPR	Units
Nominal-config. η used in fit	82.34	84.47	[%]
Approx. benefit over nominal η			[% points]
... f up to 3 Hz	2.73	2.30	
... f_{bi}, f_{bo} down to 0.01	0.09	0.21	
... L_{pis} up to 1.0 m	1.99	1.26	
... L_{pis} up to 2.0 m	4.13	2.62	
... δ_{gap} down to 0.03 mm	1.68	0.78	
... δ_{gap} down to 0.01 mm	1.75	*	
... t_{cl}/D down to 0.005	2.00	1.13	
Mean squared error of fit	0.73	0.30	[% points]
Max. absolute error of fit	2.10	0.75	[% points]

* δ_{gap} of 0.01–0.03 mm was never optimal for the 100 K HPR expander

no effect when a 0.5 m piston is used. Viewed another way, this means that choosing a 0.5 m piston instead of a 1.0 m piston has both a direct cost (it is typically ~1.26 points less efficient) and an option cost (it precludes the optional ~0.78 points that could be gained with a narrower gap).

Efficiency as a function of pressure and pressure ratio

Much of Chapter 2 was focused on demonstrating the benefit of using double expanders. The results of this chapter suggest that such designs are feasible, though particular care must be taken in the design of the low-pressure 25 K expander. Figure 3-36 summarizes (in the form of a strip plot) the efficiencies of various designs for each of the six configurations explored in the fpe_exploration_NASA5 study. The data for this plot was generated in a manner similar to the data in Tables 3.7 and 3.8: "nominal or easier" constraints on design variables were used to prune the dataset of simulated points, the best-efficiency point in the resulting subset was recorded, and the process was repeated with the constraints relaxed in every possible combination. In contrast to the tables above, however, duplicate points were not removed. The results in Figure 3-36 show that the performance of LPR expanders is on par with that of the HPR expanders, demonstrating the thermodynamic feasibility of the double-expander cryocooler designs proposed in Chapter 2.

Of the configurations simulated, the best possible efficiencies were achieved by the high-pressure LPR expanders. It is difficult to make an honest comparison between the LPR and HPR expanders since the cooling loads are different, but a few hypotheses are nevertheless put forth to explain the difference in performance. First, the reversible expander model examined in section 3.2 predicts that the ratio of cooling power to swept volume is maximized for a pressure ratio of ~3.6, or conversely, that this pressure ratio minimizes the swept volume for a given cooling load. This is very close to the ratio of 3.16 used in the LPR expanders and should yield improved performance compared to equivalent HPR configurations if the dominant losses scale with swept volume. Second, the lower pressure ratio in the LPR expander should reduce the impact of both cyclic heat transfers and appendix gap losses since pressure fluctuations are the driving factor for both of these. Third, the higher mean density of the working fluid should yield a lower thermal diffusivity; this in turn could contribute to a higher Peclet number and reduced cyclic heat transfer losses in the cold working volume, provided the expanders are already mostly-adiabatic such that the losses decrease with higher Peclet numbers (see Figure 3-11).

Unsurprisingly, the low-pressure LPR expanders were typically less efficient than their high-pressure LPR counterparts. For a given cooling power, low-pressure expanders have lower mean working fluid densities, yielding larger swept volumes and presumably-higher losses (e.g., shuttle heat transfer). This conclusion is supported by the simple model in section 3.2, which predicts an inverse relationship between expander inlet pressure and expander swept volume at a given cooling power, pressure ratio, and operating frequency. The simple model alone, however, cannot explain why the 100 K low-pressure LPR expanders are on average slightly *more* efficient than the

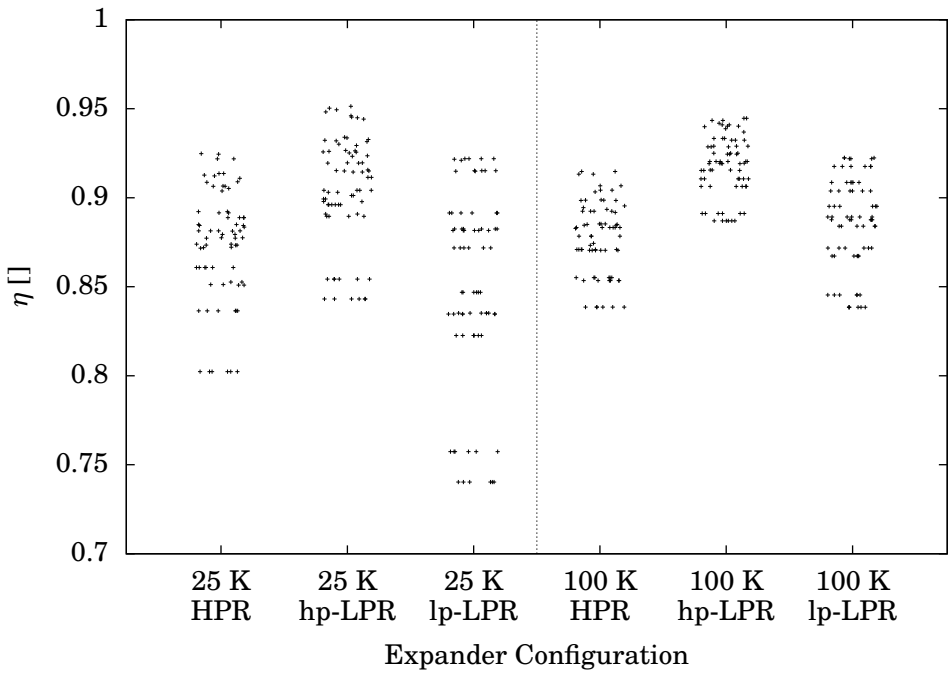

Figure 3-36: Efficiency comparisons for six expander configurations suitable for single- or double-expander ZBO cryocoolers. Various designs of differing manufacturability were presented in the form of a strip plot (with jitter used to visually separate points) for each of the six configurations in the fpe_exploration_NASA5 study. These results left further support to the double-expander designs of Chapter 2: LPR expanders either outperform HPR expanders (for both high-pressure configurations), match their efficiencies (for the 100 K low-pressure configuration) or come close for all but the worst designs (for the 25 K low-pressure configurations).

100 K HPR expanders; while its lower pressure ratio should indeed contribute to a higher cooling power per unit swept volume, this should also be heavily outweighed by the effect of the lower inlet pressure. The discrepancy likely arises from reduced cyclic heat transfer and appendix gap losses, though the different cooling powers of the LPR and HPR configurations may play a significant (and unknown) role. Regardless, the behavior is welcome given the benefits of dual LPR expanders discussed in Chapter 2.

3.4 Summary & Limitations

Parasitic losses play an important role in the performance of floating piston expanders, with efficiency losses of 30% typical in many of the expanders simulated. Furthermore, different loss mechanisms often favor different design choices and should therefore be considered in aggregate when designing an expander.

The need for aggregate loss modeling is readily apparent when selecting an expander's stroke-to-diameter ratio: shuttle heat transfers scale with S^2 and strongly favor shorter stroke lengths, cyclic heat transfer losses are minimized by S/D ratios of ~1, and the effects of clearance space limit how short the stroke can be without

excessive loss. In many of the configurations simulated, the tradeoff seems to favor S/D ratios in the range of 0.2–0.5 with the best value depending on the clearance fraction and the importance of shuttle heat transfer.

A similar tension exists between the shuttle heat transfer and gas enthalpy transfer losses: the former favors wider appendix gaps, the latter favors narrower appendix gaps, and a clear optimum often exists at an intermediate gap width. The location of this optimum is in turn influenced by other design variables such as expander length and blow-in/blow-out factors. Interestingly, while the optimum leans towards thinner gaps for the most efficient HPR expander designs in Tables 3.7 and 3.8, very efficient expanders ($\eta > 88\%$) may still be realized with relatively large 0.1 mm gaps.

The expander loss studies also yielded a few unexpected conclusions; perhaps most interesting, increasing the amount of irreversible blow-in and blow-out increased the overall expander efficiency instead of reducing it. Within reason, higher blow-in and blow-out factors can yield shorter expansion and recompression strokes for a given mass flow rate, which in turn reduces appendix gap losses enough to yield an overall performance improvement. The expander operating frequency also demonstrated an unexpected non-trivial optimum in some circumstances, seemingly owing to the behavior of the gas enthalpy transfer loss in the appendix gap (though in general higher operating frequencies seem to yield more efficient expanders, provided valve losses remain small).

Appendix gap losses play a particularly important role in driving the design of FPEs as illustrated by the examples above. Since existing models of these losses seemed unsuitable for high-pressure-ratio cryogenic expanders, a new gap model was created for this work (see section 3.3.1). The model combines locally-valid analytical expressions with 1-D numerical integration and a shooting method solution approach to capture the effects of large pressure fluctuations, pressure-driven mass flows, non-linear temperature profiles, and temperature-dependent properties. Of course, no model is without its limitations; the effects of imperfect warm-end sealing were neglected (along with any piston blow-by flows such as those proposed by Hogan), and the model's validity becomes questionable when wider gaps give rise to turbulence, larger fluid temperature fluctuations, and flows that are not thermally and hydrodynamically fully-developed throughout most of the gap. Fluid property variations resulting from density fluctuations over each cycle also have the potential to skew the model's predictions.

The technique used to estimate heat transfers in the cold end may also benefit from further study as it lacks appropriate consideration of inflow-induced turbulence and is based on heat transfer correlations which have been shown to yield artificially-low results when used for larger volume ratios. These effects would likely increase the importance of such heat transfers and may favor optimum S/D ratios closer to unity. Designers seeing to apply the results in this chapter should also bear in mind the lack of cold-end valve losses in the expander model: while the flow throttling used to regulate the speed of intake and exhaust processes is intended to occur primarily at

the warm end (between the warm end working volume and the warm end reservoirs), some operating conditions may necessitate non-negligible valve losses at the cold end.

Lastly, some attention was given to designs suitable for the double-expander configurations of Chapter 2. A simplified reversible expander model first demonstrated an interesting conclusion: an outlet pressure of $P_{\text{out}} \approx 0.3P_{\text{in}}$ minimizes the swept volume of a reversible expander for a given cooling power, inlet pressure, and operating frequency. This behavior arises from the tradeoff between the working fluid's outlet temperature (which favors lower outlet pressures for a given P_{in}) and the fluid's density at the end of expansion (which favors higher output pressures for a given P_{in}). Higher inlet pressures are always beneficial in this regard as the swept volume was found to be inversely proportional to inlet pressure at a given pressure ratio. The ratio of swept volume to cooling power, in turn, has implications for irreversible expanders: several significant losses scale with diameter or stroke length and are therefore mitigated by reducing this ratio.

In irreversible expander simulations, high-pressure LPR designs generally outperformed HPR designs. A likely explanation is that the lower pressure ratios and smaller swept volumes of the former reduce both cyclic heat transfers and appendix gap losses. The different cooling powers of the configurations may have also contributed to their different efficiencies, though how much is unknown. Low-pressure LPR designs were also found to work well despite their lower fluid densities, generally coming close to the efficiencies of the HPR configurations at 25 K and slightly exceeding them at 100 K. While a more in-depth examination of the simulation data would help to better understand the tradeoffs involved in LPR expander design, these preliminary results do support the feasibility of double-expander cryocoolers.

Chapter 4

Conclusions

4.1 Research Overview

The modified Collins cryocooler is a maturing technology, and considerable potential exists for improving performance and manufacturability through the analysis and mitigation of key losses. The work in this thesis centered around two main areas: the systems-level efficiency of the cryocooler, and the efficiency of the floating piston expanders critical to its operation. At the systems level, both simplified and detailed models were developed to evaluate the relative performance of different cryocooler configurations, with a focus on the impact of multiple expanders per stage (Chapter 2). At an expander-specific level, an expander model incorporating a variety of parasitic losses was developed and used to gain insight into loss-related design tradeoffs as well as to provide performance estimates for ZBO-specific expander designs (Chapter 3). An important component of this study was the development of a new appendix gap model incorporating the effects of the pressure-driven mass flows present in high-pressure-ratio expanders.

The remainder of Chapter 4 is devoted to presenting the primary findings of this work as well as suggesting directions for future study.

4.2 Primary Findings

The work described above yielded a variety of results and conclusions which were detailed throughout the second and third chapters. Five of these stand out as particularly significant:

1. A significant loss results from the inherent load-to-working-fluid temperature mismatch in remote-load HPR cryocoolers.

Temperature mismatch losses, which arise when a single-phase working fluid warms in a remote cooling loop in contact with an isothermal load, are one of the largest

sources of inefficiency in the Modified Collins Cryocooler. The loss's magnitude (specifically, the fractional increase in operating power for a given stage of the MCC) can be estimated by the simple heuristic $\log_{10}(\Pi)/(2n)$ for a helium working fluid, where Π is the compressor pressure ratio and n is the number of expanders in a given stage of the cooler.[1] With a pressure ratio of 10 and a single expander in each stage, this loss alone increases an MCC's operating power by an estimated ~50%.

2. In the ZBO MCC, using two expanders in the 100 K stage may be more effective than adding a third stage devoted to precooling.

To mitigate the large temperature mismatch loss described above, multiple LPR expanders may be used in series in a given stage with a fraction of the total cooling provided to the load after each expansion. Adding a second expander to the 100 K stage of a two-stage ZBO cryocooler yielded a simulated efficiency gain of 11%, despite the poorer precooling provided to the second stage; adding two expanders to both stages increased this to 24%. In contrast, adding an additional stage devoted exclusively to precooling was found to yield negligible benefit in simulations (though the recuperator models in Chapter 2 did not include the effects of axial conduction or radiation and may have also been oversized, all of which would understate the impact of precooling).

While the conclusion above may not hold in lower-temperature applications where non-idealities of the helium working fluid dominate, it appears reasonable in expanders operating at temperatures warmer than 20 K *provided that heat leaks into the recuperators can be kept small*. The conclusion is also supported by the detailed expander simulations in Chapter 3, which suggest that the efficiency of each 100 K LPR expander would be higher than that of a single HPR expander.

3. Losses in FPEs should be considered in aggregate in order to understand the resulting expander design tradeoffs.

In addition to demonstrating the feasibility of LPR expander designs, expander simulations revealed a variety of non-trivial tradeoffs between the various design variables in an FPE. The results in Chapter 3 demonstrate non-trivial optima in the appendix gap width, S/D, and blow-in and blow-out fractions, and in extreme cases even in the frequency and piston length. Furthermore, both the location and importance of these optima are in general a function of several design variables. These interactions are discussed in detail in section 3.3.4.

4. The $S/D \approx 1$ expander design heuristic may require modification when shuttle heat transfers are significant.

For a variety of expander designs at both 25 and 100 K, the expander studies above suggest that the $S/D \approx 1$ heuristic used for previous FPE designs yields excessive

[1] For an arbitrary ideal-gas working fluid the heuristic becomes $\left(\frac{5R}{4c_P}\right)\log_{10}(\Pi)/n$.

shuttle heat transfers (which scale with the square of the stroke length S^2 and therefore favor expanders with shorter strokes). In simulations, optimal values of S/D typically fell in the range of 0.2–0.5 for a variety of ZBO expander designs, a conclusion which appears to hold even with moderately high clearance fractions ($t_{cl}/D = 0.1$). These values should nevertheless be used with caution as the cyclic heat transfer model used lacks any consideration of high volume ratios or inflow-induced turbulence; both of these would increase cyclic heat transfers in the expanders studied and could drive the optimum value of S/D closer to unity.

5. Blow-in and blow-out are often beneficial to FPE efficiency, seemingly owing to the considerable effects of shuttle heat transfer.

Blow-in and blow-out merit some additional attention despite their mention above. The simulations in Chapter 3 unexpectedly demonstrated that blow-in and blow-out can be beneficial to FPE operation. These processes are themselves irreversible but reduce the swept volume devoted to expansion and recompression; for moderate amounts of blow-in and blow-out,[2] the resulting reduction in shuttle heat transfer (and perhaps other losses) often yields a net gain in simulated expander efficiency. This behavior should be considered when selecting warm-end reservoir parameters and expander control algorithm settings, though proper care must also be taken to avoid high piston velocities or excessive blow-by (neither of which were considered in this work).

4.3 Recommended Future Work

A variety of opportunities exist for future study of modified Collins cryocoolers and floating piston expanders. Even the models developed in this work were not used to their full potential; many effects could yet be explored with these, such as the influence of piston and cylinder material on appendix gap losses or the separate effects of blow-in and blow-out. Other potential areas of research involve addressing deficiencies in the current cooler and expander models; specifically,

- incorporating axial conduction, pressure losses, and variable heat transfer coefficients into the recuperator models,
- incorporating the effects of inlet-induced mixing and large volume ratios on cold-end heat-transfer correlations in the FPE, and
- incorporating the effect of valve breathing losses, piston inertia, and piston blow-by into the FPE model.

[2] While it is risky to present a general design rule without examining a wider range of configurations, blow-in and blow-out pressure defects of around 5~10% of the expander pressure drop (i.e., $f_{bi}, f_{bo} = 0.05 \sim 0.1$) seemed to yield good results for many of the expander designs in this thesis.

These should be followed by corresponding studies to examine the impact on FPE or cryocooler operation.

While many studies in this thesis would benefit from improved modeling, however, it seems prudent to pursue experimental or CFD validation as a next step. The latter may be particularly well suited to for validating the appendix gap model, where two-dimensional CFD should be sufficient to capture the main fluid flow and heat transfer behaviors while permitting geometry, materials, and operating parameters to be adjusted over a wide range. This could lead to mitigation strategies for the appendix gap losses as well as an understanding of end effects, non-sinusoidal pressure fluctuations, and interactions with piston blow-by.

The expander model is more complex and may require experimental studies in order to capture all of the thermal, fluid, and mechanical inefficiencies present; such realism is important in determining whether the model neglects any large losses present in an actual FPE. It seems feasible to build an apparatus that would allow the total clearance fraction and S/D ratio to be varied by using a movable warm-end cylinder head. Such a device could also explore variations in blow-in and blow-out factors by using a flexible control algorithm combined with warm-end bleed flows when necessary, and oversized low-resistance valves could be used in conjunction with adjustable throttles to vary the operating frequency. Though some variables such as the piston length and gap width would be more difficult to alter without constructing multiple pistons (and the diameter would be impractical to vary without constructing multiple expanders altogether), the data obtained from varying the other parameters along with the working fluid, pressure, pressure ratio, and temperature would likely provide enough data to assess the accuracy of the expander model in this thesis.

In addition to pursuing validation, it may also be interesting to broaden the scope of the present work by examining the effect of load temperature and cooling requirements in more detail, especially with regard to the design of miniaturized FPEs. A variable-load-and-temperature study performed on a multi-stage cryocooler model could also be informative, though an improved recuperator model is likely a prerequisite to this (along with a reasonable prediction of the effect of temperature and load on the efficiency of the cooler's expanders).

Finally, simplified analyses in the style of sections 2.2 and 3.2 may provide interesting insights into the effects of blow-in and blow-out factors, clearance volume, and intake mixing losses and could be a beneficial starting point for future work on FPEs.

Bibliography

[ACT05] S. K. Andersen, H. Carlsen, and P. G. Thomsen. Numerical study on the appendix gap losses in a stirling engine. In *Proceedings of the 12th International Stirling Engine Conference and Technology Exhibition*, pages 336–347, Durham, UK, 2005.

[AG71] R. A. Ackermann and W. E. Gifford. A heat balance analysis of a Gifford-McMahon cryorefrigerator. In K. D. Timmerhaus, editor, *Advances in Cryogenic Engineering 16*, pages 221–229, New York, NY, 1971. Plenum Press.

[And06] S. K. Andersen. *Numerical Simulation of Cyclic Thermodynamic Processes*. PhD thesis, Technical University of Denmark, Lyngby, Denmark, 2006.

[ARL10] Applied Research Laboratory, The Pennsylvania State University. Trade Space Visualizer 4.8.2 beta. `http://www.atsv.psu.edu/download.html`, 2010. Downloaded August 3, 2011.

[BB81] D. M. Berchowitz and R. W. Berggren. Appendix gap losses in reciprocating machines. Technical Report 81ASE187ER16, Mechanical Technologies Incorporated, 1981. Prepared for NASA Lewis Research Center.

[Ber86] D. M. Berchowitz. *Stirling cycle engine design and optimisation*. PhD thesis, University of the Witwatersrand, Johannesburg, South Africa, 1986.

[Ber02] D. M. Berchowitz. Appendix gap losses. Unpublished, 2002. Obtained via personal correspondence, January 5, 2012.

[CB96] H.-M. Chang and J. H. Baik. An exact expression for shuttle heat transfer. In P. Kittel, editor, *Advances in Cryogenic Engineering 41*, pages 1535–1542, New York, NY, 1996. Plenum Press.

[CGK98] F. J. Cantelmi, D. Gedeon, and A. A. Kornhauser. An analytical model for turbulent compression-driven heat transfer. *ASME Journal of Heat Transfer*, 120:617–623, 1998.

[Cha88] J. N. Chafe. *A study of gas spring heat transfer in reciprocating cryogenic machinery*. PhD thesis, Massachusetts Institute of Technology, Cambridge, MA, 1988.

[Cha05] G. Chaudhry. Modeling of a floating piston expander employed in a 10 K cryocooler. Master's thesis, Massachusetts Institute of Technology, Cambridge, MA, 2005.

[Col47] S. C. Collins. A helium cryostat. *The Review of Scientific Instruments*, 18(3):157–167, 1947.

[CPJ00] H.-M. Chang, D.-J. Park, and S. Jeong. Effect of gap flow on shuttle heat transfer. *Cryogenics*, 40(3):159–166, 2000.

[CS81] E. G. Cravalho and J. L. Smith, Jr. *Engineering Thermodynamics*. Pitman Publishing, Boston, MA, 1981.

[CS01] K. M. Ceridon and J. L. Smith, Jr. Remote cooling with a G-M cryocooler by use of cold electromagnetic valves driving an external flow loop. In R. G. Ross, Jr., editor, *Cryocoolers 11*, pages 393–400, New York, NY, 2001. Kluwer Academic/Plenum Publishers.

[CY11] C.-H. Cheng and H.-S. Yang. Analytical model for predicting the effect of operating speed on shaft power output of Stirling engines. *Energy*, 36(10):5899–5908, 2011.

[DWT04] R. W. Dyson, S. D. Wilson, and R. C. Tew. Review of computational stirling analysis methods (AIAA 2004-5582). In *2nd International Energy Conversion Engineering Conference*, Providence, RI, 2004. American Institute of Aeronautics and Astronautics.

[FLWW98] D. Fylstra, L. Lasdon, J. Watson, and A. Waren. Design and use of the Microsoft Excel Solver. *Interfaces*, 28(5):29–55, 1998.

[FS83] H. B. Faulkner and J. L. Smith, Jr. Instantaneous heat transfer during compression and expansion in reciprocating gas handling machinery (paper 839117). In *Proceedings of the 18th Intersociety Energy Conversion Engineering Conference*, pages 724–730, Orlando, FL, 1983.

[Gif66] W. E. Gifford. Basic investigation of cryogenic refrigeration methods. Technical Report AFFDL-TR-66-2, Wright-Patterson Air Force Base, 1966.

[GKT09] P. K. Gupta, P. K. Kush, and A. Tiwari. Experimental research on heat transfer coefficients for cryogenic cross-counter-flow coiled finned-tube heat exchangers. *International Journal of Refrigeration*, 32(5):960–972, 2009.

[GKT10] P. K. Gupta, P. K. Kush, and A. Tiwari. Experimental studies on pressure drop characteristics of cryogenic cross-counter flow coiled finned tube heat exchangers. *Cryogenics*, 50(4):257–265, 2010.

[HGK+04] C. L. Hannon, J. Gerstmann, B. J. Krass, M. J. Traum, J. G. Brisson, and J. L. Smith, Jr. Floating piston expander development for a small-scale Collins type 10 K cryocooler for space applications. In J. Waynert et al., editors, *Advances in Cryogenic Engineering 49*, pages 1650–1657, Melville, NY, 2004. American Institute of Physics.

[HGT+03] C. L. Hannon, J. Gerstmann, M. J. Traum, J. G. Brisson, and J. L. Smith, Jr. Development of a medium-scale Collins-type 10 K cryocooler. In R. G. Ross, Jr., editor, *Cryocoolers 12*, pages 587–594, New York, 2003. Kluwer Academic/Plenum Publishers.

[HKG+06] C. L. Hannon, B. J. Krass, J. Gerstmann, G. Chaudhry, J. G. Brisson, and J. L. Smith, Jr. Development and testing of a small-scale Collins type cryocooler. In J. G. Weisend, II, editor, *Advances in Cryogenic Engineering 51*, pages 1877–1884, Melville, NY, 2006. American Institute of Physics.

[HKG+07] C. L. Hannon, B. J. Krass, J. Gerstmann, G. Chaudhry, J. G. Brisson, and J. L. Smith, Jr. Modeling, development and testing of a small-scale Collins type cryocooler. In S. D. Miller and R. G. Ross, Jr., editors, *Cryocoolers 14*, pages 477–485, Boulder, CO, 2007. International Cryocooler Conference.

[HMF06] J. T. Howell, J. C. Mankins, and J. C. Fikes. In-space cryogenic propellant depot stepping stone. *Acta Astronautica*, 59(3):230–235, 2006.

[Hog12] J. Hogan. Development of a floating piston expander control algorithm for a Collins-type cryocooler. Master's thesis, Massachusetts Institute of Technology, Cambridge, MA, 2012.

[HPSK02] L. J. Hastings, D. W. Plachta, L. Salerno, and P. Kittel. An overview of NASA efforts on zero boiloff storage of cryogenic propellants. *Cryogenics*, 41(11–12):833–839, 2002.

[Jeo91] E. S. Jeong. *Heat transfer with oscillating pressure in reciprocating machinery*. PhD thesis, Massachusetts Institute of Technology, Cambridge, MA, 1991.

[Jon99] R. E. Jones. Design and testing of experimental free-piston cryogenic expander. Master's thesis, Massachusetts Institute of Technology, Cambridge, MA, 1999.

[JS92] E. S. Jeong and J. L. Smith, Jr. An analytical model of heat transfer with oscillating pressure. In M. Jensen, R. Mahajan, E. McAssey, M. F. Modest, D. Pepper, M. Sohal, and A. Lavine, editors, *General Papers in Heat Transfer*, volume 204, pages 97–104. ASME, 1992.

[Kor89] A. A. Kornhauser. *Gas-wall heat transfer during compression and expansion*. ScD thesis, Massachusetts Institute of Technology, Cambridge, MA, 1989.

[KS88] A. A. Kornhauser and J. L. Smith, Jr. Application of a complex Nusselt number to heat transfer during compression and expansion. In T. Uzkan, editor, *On Flows in Internal Combustion Engines–IV*, volume FED 65, New York, NY, 1988. ASME.

[KS93] A. A. Kornhauser and J. L. Smith, Jr. The effects of heat transfer on gas spring performance. *ASME Journal of Energy Resources Technology*, 115:70–75, 1993.

[KS94] A. A. Kornhauser and J. L. Smith, Jr. Application of a complex Nusselt number to heat transfer during compression and expansion. *ASME Journal of Heat Transfer*, 116(3):536–542, 1994.

[KS06] V. Kotsubo and G. Swift. Thermoacoustic analysis of displacer gap loss in a low temperature Stirling cooler. In J. G. Weisend, II, editor, *Advances in Cryogenic Engineering 51*, pages 353–360, Melville, NY, 2006. American Institute of Physics.

[Lee83] K. P. Lee. A simplistic model of cyclic heat transfer phenomena in closed spaces (paper 839116). In *Proceedings of the 18th Intersociety Energy Conversion Engineering Conference*, pages 720–723, Orlando, FL, 1983.

[Leo70] B. Leo. Designer's handbook for spaceborne two-stage Vuilleumier cryogenic refrigerators. Technical Report AFFDL-TR-70-54, Air Force Flight Dynamics Laboratory, 1970.

[LHM07] E. W. Lemmon, M. L. Huber, and M. O. McLinden. NIST Standard Reference Database 23: Reference fluid thermodynamic and transport properties—REFPROP, version 8.0. National Institute of Standards and Technology, Standard Reference Data Program, Gaithersburg, MD, 2007.

[LMF] E. W. Lemmon, M. O. McLinden, and D. G. Friend. Thermophysical properties of fluid systems. In P. J. Linstrom and W. G. Mallard, editors, *NIST Chemistry WebBook, NIST Standard Reference Database Number 69*. National Institute of Standards and Technology, Gaithersburg, MD, publication date unknown. `http://webbook.nist.gov/`, Accessed June 1, 2012.

[LS78] K. P. Lee and J. L. Smith, Jr. Influence of cyclic wall-to-gas heat transfer in the cylinder of the valved hot-gas engine (paper 789195). In *Proceedings of the 13th Intersociety Energy Conversion Engineering Conference*, pages 1798–1804, San Diego, CA, 1978.

[MA90] R. D. McCarty and V. D. Arp. A new wide range equation of state for helium. In R. W. Fast, editor, *Advances in Cryogenic Engineering 35*, pages 1465–1475, New York, NY, 1990. Plenum Press.

[Mar83] W. R Martini. Stirling engine design manual (second edition). Contractor Report NASA CR-168088, NASA Lewis Research Center, Cleveland, OH, 1983.

[Mar92] H. Martin. *Heat exchangers*. Hemisphere Publishing Corporation, Washington, DC, 1992.

[MD68] F. N. Magee and R. D. Doering. Vuilleumier cycle cryogenic refrigerator development. Technical Report AFFDL-TR-68-67, Air Force Flight Dynamics Laboratory, 1968.

[MG60] H. O. McMahon and W. E. Gifford. A new low-temperature gas expansion cycle—part I. In K. D. Timmerhaus, editor, *Advances in Cryogenic Engineering 5*, pages 354–367, New York, NY, 1960. Plenum Press.

[Min84] M. Minta. *Analytical and experimental studies of an optimum helium liquifaction cycle*. PhD thesis, Massachusetts Institute of Technology, Cambridge, MA, 1984.

[MW] MatWeb, LLC. Online materials information resource - MatWeb. `http://www.matweb.com/`, publication date unknown. Accessed June 1, 2012.

[NASA07] National Aeronautics and Space Administration. Small business innovation research & technology transfer 2007 program solicitations (topic T4.02: Space science and exploration sensors and instruments). `http://sbir.nasa.gov/SBIR/sbirsttr2007/solicitation/STTR/TOPIC_T4.html`, 2007. Accessed September 26, 2011.

[Nel03] G. F. Nellis. A heat exchanger model that includes axial conduction, parasitic heat loads, and property variations. *Cryogenics*, 43(9):523–538, 2003.

[NIST] National Institute of Standards and Technology, Cryogenics Technologies Group. Cryogenic material properties (NIST SRD #152). `http://cryogenics.nist.gov/MPropsMAY/material%20properties.htm`, publication date unknown. Accessed September 26, 2011.

[Pfr40] H. Pfriem. Der periodische Wärmeübergang bei kleinen Druckschwankungen. *Forschung auf dem Gebiete des Ingenieurwesens*, 11(2):67–75, 1940.

[Pfr43] H. Pfriem. Periodic heat transfer at small pressure fluctuations. Technical Report NACA-TM-1048, NACA, 1943. Translated from *Forschung auf dem Gebiete des Ingenieurwesens*, 11(2):67–75, 1940.

[PK03] D. Plachta and P. Kittel. An updated zero boil-off cryogenic propellant storage analysis applied to upper stages or depots in an LEO environment. Technical Report NASA TM—2003-211691, NASA Glenn Research Center, Cleveland, OH, 2003.

[Río69] P. A. Ríos. *An Analytical and Experimental Investigation of the Stirling Cycle*. ScD thesis, Massachusetts Institute of Technology, Cambridge, MA, 1969.

[Río71] P. A. Ríos. An approximate solution to the shuttle heat-transfer losses in a reciprocating machine. *ASME Journal of Engineering for Power*, 93(2):177–182, 1971.

[Smi02] J. L. Smith, Jr. 50 years of helium liquefaction at the MIT Cryogenic Engineering Laboratory. In S. Breon et al., editors, *Advances in Cryogenic Engineering 47*, pages 213–224, Melville, NY, 2002. American Institute of Physics.

[Sta08] W. L. Staats, Jr. Analysis of a supercritical hydrogen liquefaction cycle. Master's thesis, Massachusetts Institute of Technology, Cambridge, MA, 2008.

[TMW11] The MathWorks, Inc. MATLAB 7.12.0 (R2011a). Natick, MA, 2011.

[TSB+04] M. J. Traum, J. L. Smith, Jr., J. G. Brisson, J. Gerstmann, and C. L. Hannon. Electromagnetic smart valves for cryogenic applications. In J. Waynert et al., editors, *Advances in Cryogenic Engineering 49*, pages 428–435, Melville, NY, 2004. American Institute of Physics.

[UB84] I. Urieli and D. M. Berchowitz. *Stirling Cycle Engine Analysis*. Adam Hilger Ltd., Bristol, UK, 1984.

[Wan89] A. C. Wang. Evaluation of gas spring hysteresis losses in Stirling cryocoolers. Master's thesis, Massachusetts Institute of Technology, Cambridge, MA, 1989.

[Wes86] C. D. West. *Principles and Applications of Stirling Engines*. Van Nostrand Reinhold Company, New York, NY, 1986.

[WS90] A. C. Wang and J. L. Smith, Jr. The importance of anchoring cylinder wall temperature in Stirling cryocoolers. In P. A. Nelson, W. W. Schertz, and R. H. Till, editors, *Proceedings of the 25th Intersociety Energy Conversion Engineering Conference*, volume 5, pages 386–391, New York, NY, 1990. American Institute of Chemical Engineers.

[YS91] S. Yagyu and J. L. Smith, Jr. A study of gas spring heat transfer for non-sinusoidal piston motion (paper 91-WA-HT-6). In *ASME Winter Annual Meeting*, Atlanta, GA, 1991. ASME.

[ZL71] F. J. Zimmerman and R. C. Longsworth. Shuttle heat transfer. In K. D. Timmerhaus, editor, *Advances in Cryogenic Engineering 16*, pages 343–351, New York, NY, 1971. Plenum Press.

Appendix A

Supporting Information

A.1 Justification of ΔT Loss Heuristics

Section 2.2.3 presents two heuristics useful for estimating the magitude of the temperature mismatch loss; some mathematical justification of these is given below.

The exact solution for the dimensionless entropy generation due to the temperature mismatch loss is presented in equation (2.5) and reproduced here for convenience:

$$\frac{\dot{S}_{\text{gen}} T_{\text{load}}}{\dot{Q}_{\text{load}}} = \frac{R}{n c_P} \left(\frac{\ln(\Pi)}{1 - \Pi^{-R/(n c_P)}} \right) - 1. \tag{A.1}$$

This may be transformed into semi-log space by making the substitution $X = \ln(\Pi)$,

$$\frac{\dot{S}_{\text{gen}} T_{\text{load}}}{\dot{Q}_{\text{load}}} = \frac{R}{n c_P} \left(\frac{X}{1 - e^{-XR/(n c_P)}} \right) - 1. \tag{A.2}$$

A Taylor expansion of (A.2) around $X = 0$ now yields

$$\frac{\dot{S}_{\text{gen}} T_{\text{load}}}{\dot{Q}_{\text{load}}} = \left(\frac{R}{n c_P} \right) \frac{X}{2} + \left(\frac{R}{n c_P} \right)^2 \frac{X^2}{12} - \left(\frac{R}{n c_P} \right)^4 \frac{X^4}{720} + \left(\frac{R}{n c_P} \right)^6 \frac{X^6}{30240} + \cdots. \tag{A.3}$$

The series converges very quickly, aided by the fact that $R/(n c_P)$ is always less than one; this is consistent with the quasi-linear appearance of the function even at fairly high pressure ratios (Figure 2-3b). Now, keeping only the first term of (A.3) and replacing X with $\ln(\Pi)$,

$$\frac{\dot{S}_{\text{gen}} T_{\text{load}}}{\dot{Q}_{\text{load}}} \approx \frac{R \ln(\Pi)}{2 n c_P}. \tag{A.4}$$

Equation (A.4) already looks a lot like the heuristic presented, but uses the natural logarithm instead of the (perhaps) more intuitive base-ten logarithm. This is easily changed:

$$\frac{\dot{S}_{\text{gen}} T_{\text{load}}}{\dot{Q}_{\text{load}}} \approx \frac{R}{2 c_P \log_{10}(e)} \frac{\log_{10}(\Pi)}{n}. \tag{A.5}$$

For a monatomic ideal gas ($R/c_P = 2/5$), the constant $R/[2c_P \log_{10}(e)]$ evaluates to ~0.46. This exact value, however, is not the most desirable: while it yields the best fit to the function at $\Pi = 1$, it systematically underpredicts the function at higher pressure ratios. A value of 1/2 both fits the function better and, perhaps more importantly, is much easier to memorize. Making this replacement,

$$\frac{\dot{S}_{\text{gen}} T_{\text{load}}}{\dot{Q}_{\text{load}}} \approx \frac{1}{2} \frac{\log_{10}(\Pi)}{n}, \tag{A.6}$$

which is the heuristic given in (2.18).

Finally, equation (A.5) scales proportionally with R/c_P. To maintain consistency with the expression for monatomic gases, a leading coefficient of $\frac{5}{4}R/c_P$ may be used; this evaluates to 1/2 in the monatomic gas case. The heuristic for arbitrary ideal gases, then, is

$$\frac{\dot{S}_{\text{gen}} T_{\text{load}}}{\dot{Q}_{\text{load}}} \approx \left(\frac{5R}{4c_P}\right) \frac{\log_{10}(\Pi)}{n}. \tag{A.7}$$

A.2 Computing the Product of Real-Part Operators

The real-part of a complex number C may be written as the average of C and its complex conjugate $\overline{C}$:

$$\text{Re}\{C\} = \tfrac{1}{2}(C + \overline{C}). \tag{A.8}$$

Applying this identity to the product of two such terms (first in the direction shown above and then in reverse),

$$\begin{aligned} \text{Re}\{A\} \cdot \text{Re}\{B\} &= \tfrac{1}{4}(A + \overline{A})(B + \overline{B}) \\ &= \tfrac{1}{4}(AB + \overline{AB}) + \tfrac{1}{4}(A\overline{B} + \overline{A}B) \\ &= \tfrac{1}{2}\,\text{Re}\{AB\} + \tfrac{1}{2}\,\text{Re}\{A\overline{B}\} \\ &= \tfrac{1}{2}\,\text{Re}\left\{A(B + \overline{B})\right\}. \end{aligned} \tag{A.9}$$

This result may also be expressed as $\frac{1}{2}\,\text{Re}\left\{(A + \overline{A})B)\right\}$.

A.3 Derivation of Appendix Gap Solution

This section presents additional details of the appendix gap loss derivation (see pp. 65–71). Starting where the analysis in the main text left off, the heat equations for the piston and cylinder may be simplified to

$$\frac{\partial T_{\text{pis}}}{\partial t} = \alpha_{\text{pis}} \frac{\partial^2 T_{\text{pis}}}{\partial y_{\text{pis}}^2} \tag{A.10}$$

and

$$\frac{\partial T_{\text{cyl}}}{\partial t} = \alpha_{\text{cyl}} \frac{\partial^2 T_{\text{cyl}}}{\partial y_{\text{cyl}}^2}, \tag{A.11}$$

respectively, where y_{pis} and y_{cyl} are coordinates normal to the piston and cylinder surfaces (defined as zero at the surfaces themselves and increasing toward the center of the expander. For the fluid, applying the assumptions in the text simplifies the thermal energy equation to

$$\overline{\rho} c_P u(y) \frac{\partial T}{\partial x} = k \frac{\partial^2 T}{\partial y^2} + \frac{\partial P}{\partial t}. \tag{A.12}$$

The analysis is performed in a reference frame moving with the piston. Note that the convention for x is flipped from that in the text, which was changed for consistency with the rest of the thesis after this derivation was completed. The following candidate solutions for temperature, pressure, fluid velocity, and cylinder position are introduced to solve the above equations:

$$T = \text{Re}\left\{A(y)e^{i\omega t} + T_0 + \Gamma(x - x_0)\right\}, \tag{A.13}$$

$$P = \text{Re}\left\{P_a e^{i\omega t} e^{i\phi} + P_0\right\}, \tag{A.14}$$

$$u = \text{Re}\left\{6U \frac{y}{\delta_{\text{gap}}}\left(1 - \frac{y}{\delta_{\text{gap}}}\right) e^{i\omega t}\left(-ie^{i\phi}\right)\right\}, \tag{A.15}$$

$$x_{\text{cyl}} = -x_{\text{pis}} = \text{Re}\left\{\frac{-S}{2} e^{i\omega t}\right\}. \tag{A.16}$$

In the above equations, $A(y)$ is the complex temperature profile in either the fluid or the solids, T_0 is the local mean temperature at position x_0, Γ is the (positive) temperature gradient in the piston and cylinder, and U is the mean fluid velocity amplitude in the gap. The phase of the pressure fluctuations is included explicitly here in the factor of $e^{i\phi}$, leaving P_a as a real-valued amplitude (equivalent to $|P_1|$ in the main text of the thesis).

Substituting the candidate solutions (A.13)–(A.16) into equations (A.10)–(A.12) and dropping the real-part operators yields the following ODEs for the complex temperature in the solids,

$$i\omega A_{\text{pis}}(y_{\text{pis}}) = \alpha_{\text{pis}} A''_{\text{pis}}(y_{\text{pis}}), \tag{A.17}$$

$$i\omega A_{\text{cyl}}(y_{\text{cyl}}) = \alpha_{\text{cyl}} A''_{\text{cyl}}(y_{\text{cyl}}), \tag{A.18}$$

and in the fluid,

$$A''(y) = \frac{-ie^{i\phi}}{k}\left[\omega P_a - 6U\overline{\rho} c_P \Gamma \frac{y}{\delta_{\text{gap}}}\left(1 - \frac{y}{\delta_{\text{gap}}}\right)\right]. \tag{A.19}$$

Solving these yields

$$A_{\text{pis}}(y_{\text{pis}}) = C_1 e^{(1+i)\sqrt{\frac{\omega}{2\alpha_{\text{pis}}}}y_{\text{pis}}} + C_2 e^{-(1+i)\sqrt{\frac{\omega}{2\alpha_{\text{pis}}}}y_{\text{pis}}}, \tag{A.20}$$

$$A_{\text{cyl}}(y_{\text{cyl}}) = C_3 e^{(1+i)\sqrt{\frac{\omega}{2\alpha_{\text{cyl}}}}y_{\text{cyl}}} + C_4 e^{-(1+i)\sqrt{\frac{\omega}{2\alpha_{\text{cyl}}}}y_{\text{cyl}}}, \tag{A.21}$$

and

$$A(y) = \frac{-ie^{i\phi}}{k}\left[\omega P_a \frac{y^2}{2} - U\overline{\rho}c_P\Gamma\frac{y^3}{\delta_{\text{gap}}}\left(1 - \frac{y}{2\delta_{\text{gap}}}\right)\right] + C_5 y + C_6. \tag{A.22}$$

Six boundary conditions are needed to find the six unknowns C_1–C_6 in equations (A.20)–(A.22). The first two of these specify the complex temperature amplitudes deep within the solids:

$$A_{\text{pis}}(+\infty) = 0, \tag{A.23}$$

$$A_{\text{cyl}}(-\infty) = \frac{-\Gamma S}{2}. \tag{A.24}$$

The second two specify that each solid surface must be at the same temperature as the fluid it contacts:

$$A_{\text{pis}}(0) = A(\delta_{\text{gap}}), \tag{A.25}$$

$$A_{\text{cyl}}(0) = A(0). \tag{A.26}$$

The last two state that the heat flux must be continuous across each fluid/solid interface:

$$-k_{\text{pis}}\left.\frac{dA_{\text{pis}}}{dy_{\text{pis}}}\right|_{y_{\text{pis}}=0} = -k\left.\frac{dA}{dy}\right|_{y=\delta_{\text{gap}}}, \tag{A.27}$$

$$-k_{\text{cyl}}\left.\frac{dA_{\text{cyl}}}{dy_{\text{cyl}}}\right|_{y_{\text{cyl}}=0} = -k\left.\frac{dA}{dy}\right|_{y=0}. \tag{A.28}$$

Using these boundary conditions to solve for C_1–C_6 and back-substituting into equation (A.22) yields the following complex temperature amplitude for the fluid:

$$\begin{aligned} A(y) = {} & \frac{-ie^{i\phi}}{k}\left[\omega P_a \frac{y^2}{2} - U\overline{\rho}c_P\Gamma\frac{y^3}{\delta_{\text{gap}}}\left(1 - \frac{y}{2\delta_{\text{gap}}}\right)\right] \\ & + \frac{\theta}{\beta}\left[\frac{ie^{i\phi}\delta_{\text{gap}}^2}{2k}\left(\omega P_a - U\overline{\rho}c_P\Gamma\right)\left(i + 2b_{\text{pis}}(1+i)\right) + \frac{\Gamma S}{2}i\right]\frac{y}{\delta_{\text{gap}}} \\ & + b_{\text{cyl}}\frac{\theta}{\beta}\left[\frac{ie^{i\phi}\delta_{\text{gap}}^2}{2k}\left(\omega P_a - U\overline{\rho}c_P\Gamma\right)\left(4b_{\text{pis}} + 1 + i\right) + \frac{\Gamma S}{2}(1+i)\right] - \frac{\Gamma S}{2}, \end{aligned} \tag{A.29}$$

where β and θ are functions of the biot numbers (introduced purely for readability):

$$\beta \equiv \left(b_{\text{pis}} + b_{\text{cyl}}\right)^2 + \left(b_{\text{pis}} + b_{\text{cyl}} + 1\right)^2,$$
$$\theta \equiv \left(b_{\text{pis}} + b_{\text{cyl}}\right) - i\left(b_{\text{pis}} + b_{\text{cyl}} + 1\right).$$

To find the net energy transfer rate through the gap (not including conduction heat transfer which is computed separately), a total of three terms must be evaluated: (1) the enthalpy carried by the fluid, (2) the enthalpy carried by the moving cylinder wall, and (3) any work transferred by the cylinder wall *in excess of the PdV work on the piston.* The first of these is found by integrating $\overline{\rho} c_P T(t,y) u(t,y)$ over the cross section of the gap and then taking the cyclic average:

$$\begin{aligned}\dot{H}_{\text{fluid}} &= \frac{\omega}{2\pi}\oint\left(\int_0^{\delta_{\text{gap}}} \overline{\rho} c_P T(t,y) u(t,y) \pi D\, dy\right) dt \\ &= \frac{\omega}{2\pi}\oint\left(\overline{\rho} c_P \pi D \int_0^{\delta_{\text{gap}}} \text{Re}\left\{A(y)e^{i\omega t} + T_0 + \Gamma(x - x_0)\right\}\right. \\ &\qquad \left. \cdot\, \text{Re}\left\{6U\frac{y}{\delta_{\text{gap}}}\left(1 - \frac{y}{\delta_{\text{gap}}}\right)e^{i\omega t}\left(-ie^{i\phi}\right)\right\} dy\right) dt. \qquad \text{(A.30)}\end{aligned}$$

The enthalpy carried by the moving cylinder wall is found by multiplying the velocity of the cylinder by the thermal energy per unit length (which itself is found by integrating the surface heat flux into the cylinder and multiplying by πD) and taking the cyclic average:

$$\begin{aligned}\dot{H}_{\text{cyl}} &= \frac{\omega}{2\pi}\oint\left(\pi D \int k \left.\frac{dT}{dy}\right|_{y=0} dt\right) u_{\text{cyl}}(t)\, dt \\ &= \frac{\omega}{2\pi}\oint \text{Re}\left\{\frac{\pi D k}{i\omega} C_5 e^{i\omega t}\right\} \cdot \text{Re}\left\{\frac{-i\omega S}{2} e^{i\omega t}\right\} dt, \qquad \text{(A.31)}\end{aligned}$$

where C_5 is given by

$$C_5 = \frac{\theta}{\beta}\left[\frac{ie^{i\phi}\delta_{\text{gap}}^2}{2k}\left(\omega P_a - U\overline{\rho} c_P \Gamma\right)\left(i + 2b_{\text{pis}}(1+i)\right) + \frac{\Gamma S}{2} i\right]\frac{1}{\delta_{\text{gap}}}.$$

The cylinder work transfer term is found by first identifying the tension in the wall in excess of the force carried by the piston by means of a cold-end force balance,

$$F_{\text{cyl,excess}} = \frac{\pi}{4}\left[\left(D + 2\delta_{\text{gap}}\right)^2 - D^2\right] P(t) \approx \pi D \delta_{\text{gap}} P(t), \qquad \text{(A.32)}$$

then multiplying by the cylinder wall velocity, inverting the sign (since positive work transfer with positive wall displacement requires a compressive force, not a tensile

force) and taking the cyclic average:

$$\begin{aligned}\dot{W}_{\mathrm{cyl,excess}} &= \frac{\omega}{2\pi}\oint -piD\delta_{\mathrm{gap}}P(t)u_{\mathrm{cyl}}(t)\,dt \\ &= \frac{\omega}{2\pi}\oint -piD\delta_{\mathrm{gap}}\,\mathrm{Re}\left\{P_a e^{i\omega t}e^{i\phi}+P_0\right\}\cdot\mathrm{Re}\left\{\frac{-i\omega S}{2}e^{i\omega t}\right\}dt. \end{aligned} \tag{A.33}$$

Equations (A.30)–(A.32) may be evaluated by expanding the products of the real operators as described in Appendix A.2, noting that any $e^{(n)i\omega t}$ terms remaining after expansion do not survive the subsequent cyclic average. Following a concerning amount of algebra, this yields:

$$\begin{aligned}\overbrace{\dot{H}_{\mathrm{fluid}}+\dot{H}_{\mathrm{cyl}}+\dot{W}_{\mathrm{cyl,excess}}}^{\equiv\dot{Q}_{\mathrm{shuttle}}+\dot{H}_{\mathrm{GET}}} &= \pi D\left\{\Gamma\frac{S^2k_{\mathrm{gap}}}{8\delta_{\mathrm{gap}}}\left(\frac{b_{\mathrm{pis}}+b_{\mathrm{cyl}}+1}{\beta}\right)\right. \\ &\quad +\Gamma\frac{(\overline{\rho}c_PU)S\delta_{\mathrm{gap}}}{4}\left(\frac{(b_{\mathrm{cyl}}-b_{\mathrm{pis}})\cos\phi}{\beta}\right) \\ &\quad +\frac{\omega P_aS\delta_{\mathrm{gap}}}{8}\left(\frac{(b_{\mathrm{pis}}-b_{\mathrm{cyl}})\cos\phi+\left[4b_{\mathrm{cyl}}\left(b_{\mathrm{pis}}+b_{\mathrm{cyl}}+\frac{3}{4}\right)+b_{\mathrm{pis}}+1\right]\sin\phi}{\beta}\right) \\ &\quad +\Gamma\frac{(\overline{\rho}c_PU)^2\delta_{\mathrm{gap}}^3}{4k_{\mathrm{gap}}}\left(\frac{(b_{\mathrm{pis}}+b_{\mathrm{cyl}})\left[(2b_{\mathrm{pis}}+1)(2b_{\mathrm{cyl}}+1)+\frac{1}{2}\right]+\frac{1}{2}}{\beta}-\frac{9}{35}\right) \\ &\quad \left.-\frac{\omega P_a(\overline{\rho}c_PU)\delta_{\mathrm{gap}}^3}{4k_{\mathrm{gap}}}\left(\frac{(b_{\mathrm{pis}}+b_{\mathrm{cyl}})\left[(2b_{\mathrm{pis}}+1)(2b_{\mathrm{cyl}}+1)+\frac{1}{2}\right]+\frac{1}{2}}{\beta}-\frac{3}{10}\right)\right\}, \end{aligned} \tag{A.34}$$

which is the same as equation (3.22) in the main text except for differences in nomenclature and the use of the bulk velocity amplitude U instead of the mass flow rate amplitude $|\dot{m}_1|$.

A.4 Functions Used in Appendix Gap Model

The $f()$ and $g()$ functions in equation (3.23) on page 68 are found by splitting up the expressions for appendix gap loss (3.22) and conduction heat transfer (3.10). The $f()$ function receives the terms that are not dependent on the temperature gradient,

$$\begin{aligned}f() &= \frac{\omega|P_1|\pi DS\delta_{\mathrm{gap}}}{8}\left(\frac{(b_{\mathrm{pis}}-b_{\mathrm{cyl}})\cos\phi+\left[4b_{\mathrm{cyl}}\left(b_{\mathrm{pis}}+b_{\mathrm{cyl}}+\frac{3}{4}\right)+b_{\mathrm{pis}}+1\right]\sin\phi}{\beta}\right) \\ &\quad -\frac{\omega|P_1\dot{m}_1|c_P\delta_{\mathrm{gap}}^2}{4k_{\mathrm{gap}}}\left(\frac{(b_{\mathrm{pis}}+b_{\mathrm{cyl}})\left[(2b_{\mathrm{pis}}+1)(2b_{\mathrm{cyl}}+1)+\frac{1}{2}\right]+\frac{1}{2}}{\beta}-\frac{3}{10}\right), \end{aligned} \tag{A.35}$$

and $g()$ receives the terms that are linearly dependent on the temperature gradient (but without their dT/dx factors):

$$\begin{aligned} g() = & \frac{\pi D S^2 k_{\text{gap}}}{8\delta_{\text{gap}}} \left(\frac{b_{\text{pis}} + b_{\text{cyl}} + 1}{\beta} \right) \\ & + \frac{|\dot{m}_1| c_P S}{4} \left(\frac{(b_{\text{cyl}} - b_{\text{pis}}) \cos\phi}{\beta} \right) \\ & + \frac{(|\dot{m}_1| c_P)^2 \delta_{\text{gap}}}{4\pi D k_{\text{gap}}} \left(\frac{(b_{\text{pis}} + b_{\text{cyl}}) \left[(2b_{\text{pis}} + 1)(2b_{\text{cyl}} + 1) + \frac{1}{2} \right] + \frac{1}{2}}{\beta} - \frac{9}{35} \right) \\ & + \pi D \left(t_{\text{pis}} k_{\text{pis},x}(T) + t_{\text{cyl}} k_{\text{cyl},x}(T) \right). \end{aligned} \tag{A.36}$$

The $H_{\text{gap,out}}$ term on page 70 is found as explained there by isolating terms corresponding only to the fluid in the original analysis and integrating over one half-cycle. The result is:

$$\begin{aligned} H_{\text{gap,out}} = \frac{\pi}{\omega} \Bigg\{ & \frac{dT}{dx} \frac{|\dot{m}_1| c_P S}{4} \left(\frac{(b_{\text{cyl}} - b_{\text{pis}}) \cos\phi}{2\beta} \right. \\ & \left. + \frac{\left[(b_{\text{pis}} + b_{\text{cyl}}) \left(2b_{\text{cyl}} + \frac{1}{2} \right) + b_{\text{cyl}} + \frac{1}{2} \right] \sin\phi}{\beta} - \sin\phi \right) \\ & + \frac{dT}{dx} \frac{(|\dot{m}_1| c_P)^2 \delta_{\text{gap}}}{4\pi D k_{\text{gap}}} \left(\frac{(b_{\text{pis}} + b_{\text{cyl}}) \left[(2b_{\text{pis}} + 1)(2b_{\text{cyl}} + 1) + \frac{1}{2} \right] + \frac{1}{2}}{\beta} - \frac{9}{35} \right) \\ & - \frac{\omega |P_1 \dot{m}_1| c_P \delta_{\text{gap}}^2}{4 k_{\text{gap}}} \left(\frac{(b_{\text{pis}} + b_{\text{cyl}}) \left[(2b_{\text{pis}} + 1)(2b_{\text{cyl}} + 1) + \frac{1}{2} \right] + \frac{1}{2}}{\beta} - \frac{3}{10} \right) \Bigg\}. \end{aligned} \tag{A.37}$$

Appendix B

Code Listings

For convenience, the original PDF copy of this document contains an attachment with the files below. On some PDF viewers, this may be accessed by right-clicking the following filename and choosing to save it (consult your viewer's help menu if not): **segado2014_fpe.zip**

B.1 Main expander model (fpe_model.m)

```
function [const, Pvec, Vvec, Tvec, svec, Qwvec, Hgvec, Q_shco, H_pump, Tw, ...
    delTout, eta, Qcool, exhdir, Psol, Vsol, Tsol, ssol, Qwsol, Hgsol] = ...
    fpe_model(freq, Tvars, Pvars, geom, SD_, matls, varargin)

%FPE_MODEL Simulates a floating piston expander (FPE) as in Segado, 2014
%   M. A. Segado. Analysis and Mitigation of Key Losses in a Multi-Stage
%   25-100 K Cryocooler. Master's thesis, Massachusetts Institute of
%   Technology, Cambridge, MA, 2014.
%
%   CONST = FPE_MODEL(FREQ,T,P,GEOM,LEX,MATLS,FLUID,CORR) returns an output
%   with a vector CONST of 5 constraints that must equal zero for the solution
%   to be valid. For additional outputs, see the reference above.
%
%   CORR is an optional input; omitting it causes FPE_MODEL to self-solve
%   by calling fsolve internally.
%
%   The input parameters are listed below; a trailing underscore (_)
%   indicates a dimensionless variable.
%
%    freq : Operating frequency in cycles per second [1/s]
%
%    Tvar = [Twarm : Average temperature of warm end in [K]
%            Tin]  : Inlet temperature (usually ~load temperature) in [K]
%
%    Pvar = [Pin     : Inlet pressure in [Pa]
%            Pratio_ : Ratio of inlet pressure to outlet pressure
%            fbi_    : Ratio of blow-in Delta-P to expander Delta-P
%            fbo_]   : Ratio of blow-out Delta-P to expander Delta-P
```

```
%
%    geom = [D     : Piston/cylinder diameter in [m]
%            Lp_   : Ratio of piston length to diameter
%            tgap_ : Ratio of appendix gap width to diameter
%            tpis_ : Ratio of piston wall thickness to diameter
%            tcyl_ : Ratio of cylinder wall thickness to diameter
%            tcw_  : Ratio of equivalent warm clearance length to diameter
%            tcc_] : Ratio of equivalent cold clearance length to diameter
%
%    SD_ : Ratio of stroke length to diameter
%
%    matl = [matpis  : Piston material; 10 = G10, 304 = 304 Stainless steel
%            matcyl] : Cylinder mat'l;  10 = G10, 304 = 304 Stainless steel
%
%    corr = [m_in_corr : Factor used to meet constraints (intake mass)
%            Trc_corr  : Factor used to meet constraints (recomp. temp.)
%            Tw_corr   : Factor used to meet constraints (wall temperature)
%            Edot_corr : Factor used to meet constraints (gap energy flow)
%            m1_corr]  : Factor used to meet constraints (gap mass flow)
%
%   Example 1 (using external correction variables):
%       [const, Pvec, Vvec, Tvec, svec, Qwvec, Hgvec, ...
%       Q_shco, H_pump, Tw, delTout, eta, Qcool, exhdir ...
%       Psol, Vsol, Tsol, ssol, Qwsol, Hgsol] = ...
%           fpe_model(1, [300, 25], [1e6, 10, 0.05, 0.05], ...
%           [3.5*.0254, 8, 0.0005, 0.03, 0.01, 0.01, 0.01], 0.5, ...
%           [10,304], [1,1,1,1,1]);
%
%   Example 2 (using internal solver):
%       [const, Pvec, Vvec, Tvec, svec, Qwvec, Hgvec, ...
%       Q_shco, H_pump, Tw, delTout, eta, Qcool, exhdir ...
%       Psol, Vsol, Tsol, ssol, Qwsol, Hgsol] = ...
%           fpe_model(1, [300, 25], [1e6, 10, 0.05, 0.05], ...
%           [3.5*.0254, 8, 0.0005, 0.03, 0.01, 0.01, 0.01], 0.5, ...
%           [10,304]);


%%%%%%%%%%%%%%%%%%%%%%%%%%%%%%%%%%%%%%%%%%%%%%%%%%%%%%%%%%%%%%%%%%%%%%%%%%%%%%%
%% Define any fixed constants

%-----------------------------------------------------------------%
% REMINDER: *helium* properties are hard-coded into 'fpe_gap.m'! %
%-----------------------------------------------------------------%

% Helium working fluid ideal gas & transport property coefficients:
R = 2078;
g = 5/3;
cp = g/(g-1)*R;


%%%%%%%%%%%%%%%%%%%%%%%%%%%%%%%%%%%%%%%%%%%%%%%%%%%%%%%%%%%%%%%%%%%%%%%%%%%%%%%
%% Process inputs and guesses (and invoke self-solve if needed)

% Simple function to make code cleaner (deals elements to variables):
function [varargout] = deal_vector(x)
    for z=1:length(x), varargout{z} = x(z); end
end

% Check to see if varargin contains correction factors; self-solve if not:
```

```
if length(varargin) >= 1
    corr = varargin{1};
else
    % Set corr based on fsolve solution:
    corr = fsolve(@(x) fpe_model(freq, Tvars, Pvars, geom, ...
        SD_, matls, x), [1,1,1,1,1], optimset('Display', 'iter'));
end

% Separate vector-based input variables:
[Twarm, Tin]                        = deal_vector(Tvars);
[Pin,Pratio_,fbi_,fbo_]             = deal_vector(Pvars);
[D,Lp_,tgap_,tpis_,tcyl_,tcw_,tcc_] = deal_vector(geom);
[matpis, matcyl]                    = deal_vector(matls);
[m_in_corr, Trc_corr, Tw_corr, ...
               Edot_corr, m1_corr] = deal_vector(corr);

% Set up key variables and guesses based on correction variables:
fhigh_ = 1 - fbi_*(1 - 1/Pratio_);  % Ratio of blowin to intake pressure
flow_  = 1 + fbo_*(Pratio_ - 1);    % Ratio of blowout to exhaust pressure

Pout   = Pin / Pratio_;             % Dimensional output pressure
Vs     = (pi/4)*D^3 * SD_;          % Swept volume
Vcw    = (pi/4)*D^3 * tcw_;         % Warm clearance vol
Vcc    = (pi/4)*D^3 * tcc_;         % Cold clearance vol

Trc    = Tin * Trc_corr;            % Post-recompression temperature
Tw     = Tin * Tw_corr;             % Cold-end wall temperature

w      = 2*pi*freq;                 % Angular frequency "omega" (rad/s)
S      = D * SD_;                   % Stroke length

dtdP_abs = 1 / (2*freq*(Pin-Pout));       % Estimated magnitude of dtdP
dtdV_abs = 1 / (2*freq*Vs);               % Estimated magnitude of dtdV

Tout_isen = Tin*(Pout/Pin)^((g-1)/g);     % Isentropic output temperature
m_in = m_in_corr * Pout*Vs/(R*Tout_isen); % Intake mass


%%%%%%%%%%%%%%%%%%%%%%%%%%%%%%%%%%%%%%%%%%%%%%%%%%%%%%%%%%%%%%%%%%%%%%%%%%%%%%%
%% Compute losses and loss coefficients

%-----------------------------------------------------------------%
% REMINDER: *helium* properties are hard-coded into 'fpe_gap.m'! %
%-----------------------------------------------------------------%

% Shuttle, conduction, and pumping (gas enthalpy transfer):
Pbar = sqrt(Pin*Pout); % the pressure used to estimate density in gap
[Lp, tgap, tpis, tcyl] = deal_vector(D * [Lp_,tgap_,tpis_,tcyl_]);

phi = -pi/4; % Pressure lags gas-spring behavior by ~45 degrees

[const_gap, Qdotp, Hdotp, dmpdP, delTout] = ...
    fpe_gap(Tw, Twarm, w, Pbar, Pin-Pout, phi, ...
    tgap, S, Lp, tpis, tcyl, matpis, matcyl, ...
    [Edot_corr, m1_corr]);

Q_shco = Qdotp * pi*D / freq; % Shuttle/cond. HT per cycle (+ is cold-TO-warm)
H_pump = Hdotp * pi*D / freq; % Enthapy into gap per cycle (+ is cold-TO-warm)
dmdP_gap  = dmpdP * pi*D;
```

```
Tg = delTout + Tw;

% Cyclic heat transfer:
P0 = (Pin + Pout) / 2;
V0 = Vs/2 + Vcc;
A0 = 2*(pi/4)*D^2 + pi*D*(S/2 + D*tcc_);
Dh = 4*V0 / A0;

T0   = Tin; % Approx. temperature used to find mean cold-fluid properties
k0   = 10.^polyval([0.0665,0.3896,-2.1794], log10(T0));
rho0 = P0 / (R*T0);
a0   = k0 / (rho0 * cp); % Mean thermal diffusivity of cold fluid

Pe   = w*Dh^2/(4*a0);
Nu_k = 0.56*Pe.^0.69;                    % Kornhauser's high-Pe correlation...
Nu_r = (12.^2+Nu_k.^2).^(1/2);           % ...with low-Pe real asymptote
Nu_i = ((0.2*Pe).^-7+Nu_k.^-7).^(-1/7); % ...with low-Pe imag. asymptote

Cr = (-k0*A0/Dh) * Nu_r   * Tin/(w*Pin*Vs);
Ci = (-k0*A0/Dh) * Nu_i/w * Tin/(Pin*Vs);


%%%%%%%%%%%%%%%%%%%%%%%%%%%%%%%%%%%%%%%%%%%%%%%%%%%%%%%%%%%%%%%%%%%%%%%%%%%%%%%
%% Nondimensionalize variables

m_in = m_in * (R*Tin/(Pin*Vs));
Trc  = Trc  / Tin;
Tw   = Tw   / Tin;
dtdP_abs = dtdP_abs * (w*Pin);
dtdV_abs = dtdV_abs * (w*Vs);

Q_shco = Q_shco / (Pin*Vs);
H_pump = H_pump / (Pin*Vs);
Cg = dmdP_gap * (R*Tin/Vs);
Tg = Tg / Tin;

Pout_ = Pout/Pin;
Vcw_  = Vcw/Vs;
Vcc_  = Vcc/Vs;


%%%%%%%%%%%%%%%%%%%%%%%%%%%%%%%%%%%%%%%%%%%%%%%%%%%%%%%%%%%%%%%%%%%%%%%%%%%%%%%
%% Set up cycle ODEs and state vectors

%-------------------------------------------------------%
% NOTE: variables in this section are dimensionless! %
%-------------------------------------------------------%

% Process naming convention:
% bi  : blowin
% int : intake
% exp : expansion
% bo  : blowout
% exh : exhaust
% rc  : recompression

% Define blowin/blowout ODE:
function [dYdP] = bi_bo_ode(P,Y)
    T = Y(1);
```

```
    Tp = T*(is_bi) + Tg*(1-is_bi); % (depends on process)
    Tio = 1*(is_bi) + T*(1-is_bi); % (depends on process)
    dtdP = dtdP_abs * (2*is_bi-1); % (sign depends on process)
    V = V1 + Vw1*(1 - (P/P1).^(-1/g));
    dVdP = Vw1/(g*P1) * (P/P1).^(-1/g - 1);

    dTdP = ( (g-1)/g*Cr*(T-Tw)*dtdP + (Tio./T - 1).*P.*dVdP + ...
                (Tio./T - 1/g).*V + (Tio-Tp)*Cg  ) ...
        ./ (  Tio./T*(P.*V./T) - (g-1)/g*Ci  );

    dQwdP = -Cr*(T-Tw)*dtdP - Ci*dTdP; % HT into wall
    dHgdP = g*(Tp-Tw)*Cg;              % Enthalpy transfer into gap

    dYdP = [dTdP; dQwdP; dHgdP];
end

% Define intake/exhaust ODE:
function [dYdm] = int_exh_ode(m,Y)
    V = Y(1);
    Tio = 1*(is_int) + (P1*V./m)*(1-is_int); % (depends on process)
    dtdV = dtdV_abs * (2*is_int-1);          % (sign depends on process)

    dVdm = ( (g-1)/g*Ci*(P1*V./m.^2) - Tio  ) ...
        ./ ( (g-1)/g*Cr*(P1*V./m-Tw)*dtdV + (g-1)/g*Ci*P1./m - P1  );

    dQwdm = -Cr*(P1*V./m-Tw)*dtdV.*dVdm - (Ci*P1./m)*(dVdm - V./m);
    dHgdm = 0; % No gap flow during intake/exhaust, so no Hg

    dYdm = [dVdm; dQwdm; dHgdm];
end

% Define expansion/recompression ODE:
function [dYdP] = exp_rc_ode(P,Y)
    T = Y(1);
    Tp = Tg*(is_exp) + T*(1-is_exp); % (depends on process)
    dtdP = -dtdP_abs*(2*is_exp-1);   % (sign depends on process)
    m = m1 - Cg*(P-P1);

    dTdP = ( (g-1)/g*Cr*(T-Tw)*dtdP + (g-1)/g*m.*T./P + Cg*(T-Tp)  )...
        ./ (  m - (g-1)/g*Ci  );

    dQwdP = -Cr*(T-Tw)*dtdP - Ci*dTdP;
    dHgdP = g*(Tp-Tw)*Cg;

    dYdP = [dTdP; dQwdP; dHgdP];
end

% Set up state vectors and populate with known values (NaN for all else):
Pvec = [fhigh_, 1  , 1  , Pout_*flow_, Pout_, Pout_, fhigh_];
Vvec = [Vcc_  , NaN, NaN, NaN        , NaN  , NaN  , NaN   ];
Tvec = [Trc   , NaN, NaN, NaN        , NaN  , NaN  , NaN   ];
mvec = Pvec.*Vvec./Tvec;

% Set up vectors to collect Qw and Hg (set both to 0 in state 1):
Qwvec = [0, NaN, NaN, NaN, NaN, NaN, NaN];
Hgvec = [0, NaN, NaN, NaN, NaN, NaN, NaN];


%%%%%%%%%%%%%%%%%%%%%%%%%%%%%%%%%%%%%%%%%%%%%%%%%%%%%%%%%%%%%%%%%%%%%%%%%%%%%%%
```

```
%% Solve process ODEs and enforce constraints

%-------------------------------------------------------%
% NOTE: variables in this section are dimensionless! %
%-------------------------------------------------------%

% Set up integrator parameters and define which to use:
options = odeset();
ode_integrator = @(ode, tspan, y0) ode15s(ode, tspan, y0, options);

% 1-2: Blowin:
is_bi = 1;
P1    = Pvec(1);
V1    = Vvec(1);
Vw1   = (1+Vcc_+Vcw_) - V1; % Based on initial estimate of Vs & Vtot

[Psol,Ysol] = ode_integrator( ...
    @bi_bo_ode, [Pvec(1),Pvec(2)], [Tvec(1),Qwvec(1),Hgvec(1)]);

Psol_bi  = Psol;
Tsol_bi  = Ysol(:,1);                                Tvec(2) =  Tsol_bi(end);
Qwsol_bi = Ysol(:,2);                               Qwvec(2) = Qwsol_bi(end);
Hgsol_bi = Ysol(:,3);                               Hgvec(2) = Hgsol_bi(end);
Vsol_bi  = V1 + Vw1*(1 - (Psol_bi/P1).^(-1/g));      Vvec(2) =  Vsol_bi(end);
msol_bi  = Psol_bi.*Vsol_bi./Tsol_bi;                mvec(2) =  msol_bi(end);

% 2-3: Intake:
is_int  = 1;
P1      = Pvec(2);
mvec(3) = mvec(2) + m_in;

[msol,Ysol] = ode_integrator( ...
    @int_exh_ode, [mvec(2),mvec(3)], [Vvec(2),Qwvec(2),Hgvec(2)]);

msol_int  = msol;
Vsol_int  = Ysol(:,1);                               Vvec(3) =  Vsol_int(end);
Qwsol_int = Ysol(:,2);                              Qwvec(3) = Qwsol_int(end);
Hgsol_int = Ysol(:,3);                              Hgvec(3) = Hgsol_int(end);
Psol_int  = P1 * ones(size(msol_int));
Tsol_int  = Psol_int.*Vsol_int./msol_int;            Tvec(3) =  Tsol_int(end);

% 3-4: Expansion:
is_exp = 1;
P1     = Pvec(3);
m1     = mvec(3);

[Psol,Ysol] = ode_integrator( ...
    @exp_rc_ode, [Pvec(3),Pvec(4)], [Tvec(3),Qwvec(3),Hgvec(3)]);

Psol_exp  = Psol;
Tsol_exp  = Ysol(:,1);                               Tvec(4) =  Tsol_exp(end);
Qwsol_exp = Ysol(:,2);                              Qwvec(4) = Qwsol_exp(end);
Hgsol_exp = Ysol(:,3);                              Hgvec(4) = Hgsol_exp(end);
msol_exp  = m1 - Cg*(Psol_exp-P1);                   mvec(4) =  msol_exp(end);
Vsol_exp  = msol_exp.*Tsol_exp./Psol_exp;            Vvec(4) =  Vsol_exp(end);

% 4-5: Blowout:
is_bi = 0;
P1    = Pvec(4);
```

```
V1    = Vvec(4);
Vw1   = Vcw_; % Effectively redefines Vs and total volume

[Psol,Ysol] = ode_integrator( ...
    @bi_bo_ode, [Pvec(4),Pvec(5)], [Tvec(4),Qwvec(4),Hgvec(4)]);

Psol_bo  = Psol;
Tsol_bo  = Ysol(:,1);                              Tvec(5) =  Tsol_bo(end);
Qwsol_bo = Ysol(:,2);                             Qwvec(5) = Qwsol_bo(end);
Hgsol_bo = Ysol(:,3);                             Hgvec(5) = Hgsol_bo(end);
Vsol_bo  = V1 + Vw1*(1-(Psol_bo/P1).^(-1/g));      Vvec(5) =  Vsol_bo(end);
msol_bo  = Psol_bo.*Vsol_bo./Tsol_bo;              mvec(5) =  msol_bo(end);

% 5-6: Exhaust:
is_int  = 0;
P1      = Pvec(5);
mvec(6) = mvec(1) + Cg*(Pvec(7)-Pvec(6)); % (so final mass will = m(1))

[msol,Ysol] = ode_integrator( ...
    @int_exh_ode, [mvec(5),mvec(6)], [Vvec(5),Qwvec(5),Hgvec(5)]);

msol_exh  = msol;
Vsol_exh  = Ysol(:,1);                             Vvec(6) =  Vsol_exh(end);
Qwsol_exh = Ysol(:,2);                            Qwvec(6) = Qwsol_exh(end);
Hgsol_exh = Ysol(:,3);                            Hgvec(6) = Hgsol_exh(end);
Psol_exh  = P1 * ones(size(msol_exh));
Tsol_exh  = Psol_exh.*Vsol_exh./msol_exh;          Tvec(6) =  Tsol_exh(end);

% 6-7: Recompression:
is_exp = 0;
P1     = Pvec(6);
m1     = mvec(6);

[Psol,Ysol] = ode_integrator( ...
    @exp_rc_ode, [Pvec(6),Pvec(7)], [Tvec(6),Qwvec(6),Hgvec(6)]);

Psol_rc  = Psol;
Tsol_rc  = Ysol(:,1);                              Tvec(7) =  Tsol_rc(end);
Qwsol_rc = Ysol(:,2);                             Qwvec(7) = Qwsol_rc(end);
Hgsol_rc = Ysol(:,3);                             Hgvec(7) = Hgsol_rc(end);
msol_rc  = m1 - Cg*(Psol_rc-P1);                   mvec(7) =  msol_rc(end);
Vsol_rc  = msol_rc.*Tsol_rc./Psol_rc;              Vvec(7) =  Vsol_rc(end);

% Enforce constraints (normalized):
const = [ ...
    (Vvec(4)-Vcc_)/1 - 1, ...  % Computed stroke vol. must match guess
    Vvec(7)/Vvec(1) - 1, ...   % Final volume must match initial volume
    Qwvec(7)-Qwvec(1) + Hgvec(7)-Hgvec(1) ...
       - (Q_shco+H_pump), ...  % Cold wall/gap First Law (norm. by Pin*Vs)
    const_gap];                % Gap sol. constraints (x2) must be satisfied


%%%%%%%%%%%%%%%%%%%%%%%%%%%%%%%%%%%%%%%%%%%%%%%%%%%%%%%%%%%%%%%%%%%%%%%%%%%%%%%
%% Organize and redimensionalize outputs

% Check to make sure expansion was in correct direction:
exhdir = Vsol_exh(end) - Vsol_exh(1); % (should be negative)

% Dimensionless:
```

```
delta_m    = [msol_bo' msol_exh'] - msol_bo(1);
delta_mgap = Cg * ([Psol_bo' Psol_exh'] - Psol_bo(1));

% Dimensional:
mout   = -(delta_m + delta_mgap) * Pin*Vs/(R*Tin);
Tfluid = [Tsol_bo' Tsol_exh'] * Tin;
Toutav = trapz(mout, Tfluid) / (mout(end)-mout(1));
eta    = (Tin - Toutav) / (Tin - Tout_isen);
Qcool  = freq * (mout(end)-mout(1)) * cp * (Tin-Toutav);

% Redimensionalize variable vectors and compute entropy:
Pvec  = Pvec * Pin;
Vvec  = Vvec * Vs;
Tvec  = Tvec * Tin;
svec  = cp*log(Tvec/Tin) - R*log(Pvec/Pin); % Use Tin, Pin as reference state
Qwvec = Qwvec * (Pin*Vs);
Hgvec = Hgvec * (Pin*Vs);

% Redimensionalize gap losses:
Q_shco = Q_shco * (Pin*Vs);
H_pump = H_pump * (Pin*Vs);

% Also assemble longer solutions for plotting:
Psol  = [Psol_bi' Psol_int' Psol_exp' Psol_bo' Psol_exh' Psol_rc'] * Pin;
Vsol  = [Vsol_bi' Vsol_int' Vsol_exp' Vsol_bo' Vsol_exh' Vsol_rc'] * Vs;
Tsol  = [Tsol_bi' Tsol_int' Tsol_exp' Tsol_bo' Tsol_exh' Tsol_rc'] * Tin;
ssol  = cp*log(Tsol/Tin) - R*log(Psol/Pin);
Qwsol = [Qwsol_bi' Qwsol_int' Qwsol_exp' Qwsol_bo' Qwsol_exh' Qwsol_rc']...
    * (Pin*Vs);
Hgsol = [Hgsol_bi' Hgsol_int' Hgsol_exp' Hgsol_bo' Hgsol_exh' Hgsol_rc']...
    * (Pin*Vs);

% Performance metrics:
Tw = Tw * Tin;
Tg = Tg * Tin;

end
```

B.2 Appendix gap model (fpe_gap.m)

```
function [const, Qdotp, Hdotp, dmpdP, delTout] = fpe_gap(Tw, Twarm, w, Pbar, ...
    DeltaP, phi, tgap, S, L, tpis, tcyl, matpis, matcyl, varargin)

% Check to see if varargin contains correction factors; self-solve if not:
if length(varargin) >= 1
    corr = varargin{1};
    doplot = 0;
else
    % Set corr based on fsolve solution:
    corr = fsolve(@(x) fpe_gap(Tw, Twarm, w, Pbar, DeltaP, phi, tgap, ...
        S, L, tpis, tcyl, matpis, matcyl, x), [1,1]);
    doplot = 1;
end
```

```
Edot_corr = corr(1);
mdot_corr = corr(2);


%%%%%%%%%%%%%%%%%%%%%%%%%%%%%%%%%%%%%%%%%%%%%%%%%%%%%%%%%%%%%%%%%%%%%%%%%%%%%%%
%% Define properties

% Helium (hard-coded) ideal gas & transport property coefficients:
R = 2078;
g = 5/3;
cp = g/(g-1)*R;
k_he = [0.0665,0.3896,-2.1794];
mu_he = [0.0507,0.4257,-6.0654];

% G10 properties/coefficients:
kn_g10 = [0,0.0397,-0.6905,4.4954,-14.663,26.272,-26.068,13.788,-4.1236];
kw_g10 = [-0.11701,1.48806,-7.95635,23.1778,-39.8754,41.1625,-24.8998, ...
    8.80228,-2.64827];
c_g10 = [0,0.015236,-0.24396,1.4294,-4.2386,7.3301,-8.2982,7.6006,-2.4083];
rho_g10 = 1800;

% 304 Stainless Steel properties/coefficients:
k_304ss = [-0.0199,0.165,-0.4658,0.4256,0.2334,-0.626,0.2543,1.3982, ...
    -1.4087];
c_304ss = [0,-2.239153,24.7593,-112.9212,274.0328,-381.0098,303.647, ...
    -127.5528,22.0061];
rho_304ss = 8000;

% Set properties according to material/fluid:
kgap  = k_he;  % Helium is hard-coded at the moment
mugap = mu_he; % Helium is hard-coded at the moment

switch matpis
    case 10
        knpis  = kn_g10; % (normal direction)
        kwpis  = kw_g10; % (warp direction)
        cpis   = c_g10;
        rhopis = rho_g10;
    case 304
        knpis  = k_304ss;
        kwpis  = k_304ss;
        cpis   = c_304ss;
        rhopis = rho_304ss;
end

switch matcyl
    case 10
        kncyl  = kn_g10; % (normal direction)
        kwcyl  = kw_g10; % (warp direction)
        ccyl   = c_g10;
        rhocyl = rho_g10;
    case 304
        kncyl  = k_304ss;
        kwcyl  = k_304ss;
        ccyl   = c_304ss;
        rhocyl = rho_304ss;
end
```

```
%%%%%%%%%%%%%%%%%%%%%%%%%%%%%%%%%%%%%%%%%%%%%%%%%%%%%%%%%%%%%%%%%%%%%%%%%%%%%%%
%% Solve temperature, pressure, and average velocity profiles

% Guess cold-end mass flow rate (per unit circumference):
Tlm      = (Twarm-Tw)/log(Twarm/Tw);
k        = 10.^polyval(kgap, log10(Tlm));
m1_guess = mdot_corr * w*DeltaP*L*tgap/(2*R*Tlm);

% Guess Edot (per unit circumference):
% (This is essentially a copy-paste of code further down; suboptimal, I know.)
    DP = DeltaP;
    m1 = m1_guess/2;
    T  = Tlm;

    rho = Pbar/(R*T);
    mu  = 10.^polyval(mugap, log10(T));
    k   = 10.^polyval(kgap, log10(T));

    U = (m1)/(rho*tgap);

    % Wall biot numbers (using normal direction conductivity):
    c = (k/tgap) / sqrt( 2*w * rhocyl * ...
        10.^polyval(kncyl,log10(T)) * 10.^polyval(ccyl,log10(T)) );
    d = (k/tgap) / sqrt( 2*w * rhopis * ...
        10.^polyval(knpis,log10(T)) * 10.^polyval(cpis,log10(T)) );

    % Gap heat transfer solution:
    B = (c+d)^2 + (c+d+1)^2; % Common denominator

    F = tcyl*10.^polyval(kwcyl,log10(T)) ...     % Cylinder conduction
      + tpis*10.^polyval(kwpis,log10(T)) ...     % Piston conduction
      + k*S^2/(8*tgap) * (c+d+1)/B ...           % dx-shuttle (Chang & Baik '96)
      + S*tgap*rho*cp*U/4 * (c-d)*cos(phi)/B ... % U-shuttle + dx-pump.
      + tgap^3*(rho*cp*U)^2/(4*k) ...            % U-pumping
            * ( ((c+d)*((2*c+1)*(2*d+1)+1/2) + 1/2)/B - 9/35 );

    G = S*tgap*w*DP/(16*B) ...                   % DP-shuttle + Wcyl
            * ((d-c)*cos(phi) + (4*c*(c+d+3/4)+d+1)*sin(phi)) ...
      - tgap^3*(rho*cp*U)*w*DP/(8*k) ...         % DP-pumping
            * ( ((c+d)*((2*c+1)*(2*d+1)+1/2) + 1/2)/B - 3/10 );

    dTdx  = (Twarm-Tw)/L;              % Assume linear profile for initial guess
    Edotp = -(dTdx*F + G) * Edot_corr; % Inital Edot guess

% Define the system of ODEs:
function [dYdx, Hdotp] = gap_ode(~,Y)
    DP = Y(1);
    m1 = Y(2);
    T  = Y(3);

    % Fluid properties:
    rho = Pbar/(R*T);
    mu  = 10.^polyval(mugap, log10(T));
    k   = 10.^polyval(kgap, log10(T));

    % Fluid motion
    dm1dx = -w*tgap/(2*R*T) * DP; % (...omits 'i' as explained in Segado, 2014)
    dDPdx = -24*R*T*mu/(tgap^3*Pbar) * m1;
```

```
    % Discard phase information, find average velocity:
    DP = (DP);            % (...omits 'i' as explained in Segado, 2014)
    U  = (m1)/(rho*tgap); % (...omits 'i' as explained in Segado, 2014)

    % Wall biot numbers (using normal direction conductivity):
    c = (k/tgap) / sqrt( 2*w * rhocyl * ...
        10.^polyval(kncyl,log10(T)) * 10.^polyval(ccyl,log10(T)) );
    d = (k/tgap) / sqrt( 2*w * rhopis * ...
        10.^polyval(knpis,log10(T)) * 10.^polyval(cpis,log10(T)) );

    % Gap heat transfer solution:
    B = (c+d)^2 + (c+d+1)^2; % Common denominator

    F = tcyl*10.^polyval(kwcyl,log10(T)) ...     % Cyl. conduction
      + tpis*10.^polyval(kwpis,log10(T)) ...     % Pis. conduction
      + k*S^2/(8*tgap) * (c+d+1)/B ...           % dx-shuttle (Chang & Baik '96)
      + S*tgap*rho*cp*U/4 * (c-d)*cos(phi)/B ... % U-shuttle + dx-pump.
      + tgap^3*(rho*cp*U)^2/(4*k) ...            % U-pumping
            * ( ((c+d)*((2*c+1)*(2*d+1)+1/2) + 1/2)/B - 9/35 );

    G = S*tgap*w*DP/(16*B) ...                   % DP-shuttle + Wcyl
            * ((d-c)*cos(phi) + (4*c*(c+d+3/4)+d+1)*sin(phi)) ...
      - tgap^3*(rho*cp*U)*w*DP/(8*k) ...         % DP-pumping
            * ( ((c+d)*((2*c+1)*(2*d+1)+1/2) + 1/2)/B - 3/10 );

    dTdx = (-Edotp - G) / F;

    % Collect and return derivatives:
    dYdx = [dDPdx; dm1dx; dTdx];

    % Find/return only enthalpy flows (not needed by ode45 but used later):
    Hdotp = -dTdx * S*tgap*rho*cp*U/8 ...        % dx-pumping
            * ( ((c-d)*cos(phi)+((c+d)*(4*c+1)+2*c+1)*sin(phi))/B ...
                - 2*sin(phi) ) ...
          - dTdx * tgap^3*(rho*cp*U)^2/(4*k) ... % U-pumping
            * ( ((c+d)*((2*c+1)*(2*d+1)+1/2) + 1/2)/B - 9/35 ) ...
          + tgap^3*(rho*cp*U)*w*DP/(8*k) ...     % DP-pumping
            * ( ((c+d)*((2*c+1)*(2*d+1)+1/2) + 1/2)/B - 3/10 );
end

% Do the integration:
[X,Y] = ode45(@gap_ode, [0, L], [DeltaP, m1_guess, Tw]);

% Plot if appropriate:
if doplot == 1
    figure(2);
    plot(X,Y(:,2));
    title('Mass flow rate');

    figure(3);
    plot(X,Y(:,1));
    title('Pressure');

    % Now, compute only enthalpy flows and equivalent input/output temperature
    Hdotp = NaN * Y(:,1);
    for z = 1:length(Hdotp)
        [~, Hdotp(z)] = gap_ode(X,Y(z,:));
    end
```

```
    figure(5);
    plot(X, Hdotp, 'r-', X, Edotp-Hdotp, 'b-');

    miobar = (2/pi) * Y(:,2);
    delTout = Hdotp ./ (miobar * cp);

    figure(1);
    plot(X, Y(:,3), 'b-', X, Y(:,3)+delTout, 'r:', X, Y(:,3)-delTout, 'r:');
    title('Temperature');
end


%%%%%%%%%%%%%%%%%%%%%%%%%%%%%%%%%%%%%%%%%%%%%%%%%%%%%%%%%%%%%%%%%%%%%%%%%%%%%%%
%% Assemble outputs

% Enforce constraints (normalized):
const = [ ...
    Y(end,2)/m1_guess, ... % Mass flow rate must be zero at x=L
    Y(end,3)/Twarm - 1];   % Temperature must be Twarm at x=L

% Compute non-pumping losses and estimate dmdP & output temperature:
[~, Hdotp] = gap_ode(X,Y(1,:));
miobar     = (2/pi) * Y(1,2);
Qdotp      = Edotp - Hdotp;
delTout    = -Hdotp ./ (miobar * cp);
dmpdP      = 2*m1_guess / (w*DeltaP);

end
```

B.3 Test controller (fpe_exploration_NASA5.m)

```
function fpe_exploration_NASA5()

%%%%%%%%%%%%%%%%%%%%%%%%%%%%%%%%%%%%%%%%%%%%%%%%%%%%%%%%%%%%%%%%%%%%%%%%%%%%%%%
%% Set up variable ranges

% Continuous ranges for design variables:
ranges = [
    0.25    4.0    % 1 - freq [1/s]
    0.005   0.25   % 2 - fbi_ & fbo_
    NaN     NaN    % 3 - D [m] (Set by solver to meet Qload)
    0.25    2.0    % 4 - Lp [m]
    1e-5    0.001  % 5 - tgap [m]
    0.005   0.1    % 6 - tcw_ & tcc_
    0.05    2      % 7 - SD_
];

% Textual variable names:
names = {
    'freq [1/s]'
    'fbi & fbo []'
    'D [m]'
    'Lp [m]'
    'tgap [m]'
```

```
    'tcw/D & tcc/D []'
    'S/D []'
};

% Discrete choices for design variables:
discretes = {
    [       0.3     1       3           ]  % 1 - freq [1/s]
    [       0.01    0.05    0.2         ]  % 2 - fbi_ & fbo_
    [               NaN                 ]  % 3 - D [m] (Set by solver)
    [0.25   0.5     1       2           ]  % 4 - Lp [m]
    [1e-5   3e-5    1e-4    3e-4    0.001]  % 5 - tgap [m]
    [       0.005   0.02    0.1         ]  % 6 - tcw_ & tcc_
    [0.1    0.2     0.5     1           ]  % 7 - SD_
};

% Constants:
Twarm   = 300;
tpis_   = 0.03;
tcyl_   = 0.01;
matl    = [10, 304];


%%%%%%%%%%%%%%%%%%%%%%%%%%%%%%%%%%%%%%%%%%%%%%%%%%%%%%%%%%%%%%%%%%%%%%%%%%%%%%%
%% Run main loop

% Set random number generator seed:
reset(RandStream.getDefaultStream,sum(100*clock));


nfiles = 500; % Total # of files to save (500 = 5 days at 1 save every 20 min)
nbatch = 204; % Total # of batches per file (divisible by # of cases below)

Dguess = 0.1; % Initial guess of diamater

    % Constraint function for solver:
    function c = FUN(X)
        v(3) = X(1)*Dguess;
        corrvals = X(2:6);

        [const, ~, Vvec, Tvec, ~,~,~, Q_shco, H_pump, Tw, delTout, ...
            etaeta, Qcool, exhaustdir, ~, Vsol, Tsol, ~,~,~] = ...
        fpe_model(v(1),[Twarm, TinTin],[PinPin,Pratio_,v(2),v(2)], ...
        [v(3),v(4)/v(3),v(5)/v(3),tpis_,tcyl_,v(6),v(6)], ...
        v(7),matl,corrvals);

        c = [const, Qcool/QloadQload-1];

        if ~isempty(lastwarn)
            error(lastwarn);
        end
    end

for filenum = 1:nfiles

    % Preallocate (or reset) arrays
    [eta, Qload, Tin, Pin] = deal(NaN * (1:nbatch));
    vars  = NaN * ranges(:,1) * (1:nbatch);
    corrs = NaN * [1;1;1;1;1] * (1:nbatch);
    QsHpTwdT = NaN * [1;1;1;1] * (1:nbatch);
```

```
goodbad = zeros(1,nbatch);
negvol = zeros(1,nbatch);

for batchnum = 1:nbatch
    lastwarn(''); % Clear any warnings

    % Try a few times before giving up:
    numtries = 2;
    while numtries > 0

        % Alternate between six different expander configurations:
        switch mod(batchnum,6)

            case 0 % 25 K, hp-LPR
                QloadQload = 20/2;
                TinTin     = 25 * 0.95;
                PinPin     = 1e6;
                Pratio_ = sqrt(10);

            case 1 % 100 K, hp-LPR
                QloadQload = 100/2;
                TinTin     = 100 * 0.95;
                PinPin     = 1e6;
                Pratio_ = sqrt(10);

            case 2 % 25 K, lp-LPR
                QloadQload = 20/2;
                TinTin     = 25 * 0.95;
                PinPin     = 1e6/sqrt(10);
                Pratio_ = sqrt(10);

            case 3 % 100 K, lp-LPR
                QloadQload = 100/2;
                TinTin     = 100 * 0.95;
                PinPin     = 1e6/sqrt(10);
                Pratio_ = sqrt(10);

            case 4 % 25 K, HPR
                QloadQload = 20;
                TinTin     = 25 * 0.95;
                PinPin     = 1e6;
                Pratio_ = 10;

            case 5 % 100 K, HPR
                QloadQload = 100;
                TinTin     = 100 * 0.95;
                PinPin     = 1e6;
                Pratio_ = 10;
        end

        try
            % Randomize inputs:
            v = ranges(:,1) ...
                .* (ranges(:,2)./ranges(:,1)) .^ rand(size(ranges(:,1)));

            contindex = ceil(rand(1)*6);
            if contindex >= 3
                contindex = contindex + 1;
```

```
    end

    for disc = 1:length(discretes);
        thedisc = discretes{disc};
        numd = length(thedisc);
        seldi = ceil(rand(1)*numd);
        if disc ~= contindex
            v(disc) = thedisc(seldi);
        end
    end

    % Run solver:
    s = fsolve(@FUN, [1,1,1,1,1,1], optimset('Display', 'iter'));
    CCCC = FUN(s);

    disp([num2str(QloadQload), 'W / ', num2str(TinTin), ...
        'K / ', num2str(PinPin/1e6), ...
        'MPa - Efficiency: ', num2str(etaeta)]);
    disp(['Left in batch: ', num2str(nbatch - batchnum)]);

    if (exhaustdir <= 0) && (max(abs(CCCC)) < 1e-6)
        disp('==================================================');
        disp('=================== Success! ====================');
        disp('==================================================');
        vars(:,batchnum) = v;
        corrs(:,batchnum) = corrvals';
        eta(batchnum) = etaeta;
        Qload(batchnum) = Qcool;
        Tin(batchnum) = TinTin;
        QsHpTwdT(:,batchnum) = [Q_shco; H_pump; Tw; delTout];

        Pin(batchnum) = PinPin;
        negvol(batchnum) = min(Vvec)<0;

        plotline = 'k-';
        goodbad(batchnum) = 1;

        numtries = 0;
    else
        disp('##################################################');
        disp('############### Solution Not Valid ###############');
        disp('##################################################');
        plotline = 'r-';

        numtries = numtries - 1;
        disp(['Retries Left: ', num2str(numtries)]);
    end

    drawnow;

catch me
        disp('// // // // // // // // // // // // // // // // // //');
        disp('// // // // // // //  Error;  // // // // // // //');
        disp('// // // // // // // // // // // // // // // // // //');
        disp(['An error occurred while solving: ', me.message]);

        numtries = numtries - 1;
        disp(['Retries Left: ', num2str(numtries)]);
end
```

```
        end % (tries)
    end % (batches)

    try
        % Eliminate bad points:
        goodbad = logical(goodbad);
        vars     = vars(:,goodbad);
        corrs    = corrs(:,goodbad);
        eta      = eta(goodbad);
        Qload    = Qload(goodbad);
        Tin      = Tin(goodbad);
        QsHpTwdT = QsHpTwdT(:,goodbad);
        Pin      = Pin(goodbad);
        negvol   = negvol(goodbad);

        % Save file to disk:
        name = [ ...
            'NASA5_', ...
            datestr(now, 'ddmmmyyyy_HHMMSS'), '_', ...
            getenv('username'), '_', ...
            num2str(floor(rand(1)*90000+10000)) ];

        save(name,'vars','corrs','eta','Qload','Tin','QsHpTwdT','negvol', ...
            'names','ranges','discretes','Twarm','Pin','Pratio_','tpis_', ...
            'tcyl_','matl');

        disp('&&&&&&&&&&&&&&&&&&&&&&&& Saving File! &&&&&&&&&&&&&&&&&&&&&&&&');
        disp([num2str(nfiles - filenum), ' files left.']);

    catch me
        disp(['An error occurred while saving file: ', me.message]);
    end
end % (files)

end
```

Appendix C

Sample Simulation Data

Pin	Tin	Qc	f	fbio	D	Lp	tgap	tcl/D	S/D	eta
1.00E+06	23.75	10	3.0000	0.2000	0.0211	1.0000	0.0300	0.0433	1.0000	0.8405
1.00E+06	23.75	10	1.0000	0.0500	0.0608	0.5000	0.0300	0.0200	0.1665	0.8252
1.00E+06	23.75	10	0.3000	0.0500	0.1814	2.0000	1.0000	0.0053	0.2000	0.5106
1.00E+06	95	100	0.3000	0.1518	0.1065	1.0000	0.1000	0.0200	1.0000	0.6730
1.00E+06	95	50	0.3000	0.2000	0.1731	0.5000	0.0100	0.0084	0.1000	0.7499
1.00E+06	95	50	3.0000	0.0182	0.1083	2.0000	0.1000	0.0200	0.1000	0.9050
1.00E+06	95	100	3.0000	0.2000	0.1052	0.2684	0.1000	0.0200	0.1000	0.7330
1.00E+06	23.75	20	1.5873	0.0100	0.0512	0.5000	0.0100	0.0050	0.5000	0.7357
3.16E+05	95	50	1.0000	0.0500	0.3297	0.5000	0.1000	0.0765	0.1000	0.4436
3.16E+05	95	50	1.0000	0.0500	0.1564	0.5000	1.0000	0.0100	0.2000	0.8311
1.00E+06	23.75	10	1.0000	0.0500	0.1024	2.0000	0.1864	0.0050	0.1000	0.8191
3.16E+05	23.75	10	0.3780	0.0100	0.1505	2.0000	0.1000	0.0050	0.1000	0.8078
3.16E+05	23.75	10	3.0000	0.2000	0.0424	0.5934	0.0300	0.1000	1.0000	0.3743
1.00E+06	23.75	10	3.0000	0.0100	0.0277	2.0000	0.1000	0.1000	0.9176	0.8947
1.00E+06	95	50	1.0000	0.1267	0.0817	0.2500	0.0300	0.1000	1.0000	0.2820
1.00E+06	23.75	10	0.3000	0.0100	0.0637	2.0000	0.0300	0.0448	0.5000	0.8317
1.00E+06	95	100	0.3000	0.2000	0.1027	2.0000	0.1325	0.1000	1.0000	0.7192
3.16E+05	95	50	0.3000	0.0500	0.2195	1.0000	0.0300	0.0265	0.5000	0.3313
3.16E+05	23.75	10	3.0000	0.0100	0.0397	0.3755	0.3000	0.1000	1.0000	0.6419
1.00E+06	23.75	10	1.0000	0.0500	0.0560	0.4629	0.1000	0.0050	0.2000	0.8407
1.00E+06	95	100	1.6697	0.2000	0.0579	1.0000	0.3000	0.0050	1.0000	0.7726
1.00E+06	95	100	3.0000	0.0322	0.0659	1.0000	0.3000	0.0050	1.0000	0.8572
1.00E+06	23.75	20	1.0000	0.0100	0.3996	0.5000	1.0000	0.0534	0.2000	0.1216
1.00E+06	95	100	1.0000	0.0100	0.2417	0.5000	1.0000	0.0050	0.1568	0.7330
1.00E+06	23.75	20	0.5949	0.2000	0.0608	0.5000	0.0300	0.1000	1.0000	0.3945
1.00E+06	95	100	1.0000	0.0100	0.2471	2.0000	0.1777	0.0050	0.1000	0.8075
1.00E+06	95	100	1.0000	0.0100	0.2260	0.7427	0.3000	0.0050	0.1000	0.7997
3.16E+05	23.75	10	0.4267	0.2000	0.1695	1.0000	1.0000	0.0200	0.1000	0.5926
1.00E+06	95	50	3.0000	0.0100	0.0514	1.0000	0.0223	0.1000	0.5000	0.8851
3.16E+05	95	50	3.0000	0.2000	0.1210	1.0000	0.1363	0.0200	0.1000	0.8357
1.00E+06	23.75	20	0.3000	0.2000	0.1128	0.2500	0.7191	0.0200	0.2000	0.6065
1.00E+06	95	50	0.3000	0.0062	0.1872	2.0000	0.0300	0.1000	0.2000	0.7999
1.00E+06	23.75	20	1.0000	0.2000	0.0533	1.0000	0.0300	0.1000	0.4576	0.7208
1.00E+06	23.75	20	3.0000	0.2000	0.0336	0.2500	0.0504	0.0200	0.5000	0.7367
1.00E+06	23.75	10	2.5540	0.0100	0.0392	1.0000	0.0100	0.0050	0.2000	0.9290
1.00E+06	23.75	10	1.0000	0.2000	0.0705	1.0000	0.1000	0.0200	0.0972	0.8307
3.16E+05	23.75	10	0.3000	0.0500	0.1153	1.0000	0.3000	0.0077	1.0000	0.2321
1.00E+06	23.75	10	3.0000	0.2000	0.0624	0.5000	0.3000	0.0200	0.1137	0.6268
3.16E+05	95	50	1.7277	0.2000	0.0797	2.0000	0.0300	0.0200	0.5000	0.8324
1.00E+06	95	100	1.0091	0.0100	0.1025	0.5000	1.0000	0.0200	1.0000	0.7959
1.00E+06	23.75	10	1.0000	0.0512	0.1347	2.0000	0.3000	0.0050	0.1000	0.6692
1.00E+06	23.75	20	1.0000	0.0100	0.0574	0.2500	0.4720	0.0200	1.0000	0.6004
3.16E+05	95	50	3.0000	0.0500	0.1956	1.0000	1.0000	0.0050	0.1222	0.7746
3.16E+05	95	50	0.3059	0.0100	0.2481	0.2500	1.0000	0.1000	0.5000	0.2983
3.16E+05	95	50	0.3000	0.2000	0.3585	1.0000	0.0100	0.0050	1.7403	0.0188
3.16E+05	95	50	3.0000	0.2000	0.0739	0.5000	0.9322	0.0050	0.5000	0.8360
1.00E+06	23.75	20	0.3176	0.0100	0.0879	2.0000	0.0300	0.0200	0.5000	0.8038
1.00E+06	23.75	10	0.3000	0.0498	0.2573	2.0000	1.0000	0.0050	0.1000	0.4125
3.16E+05	95	50	0.3095	0.0100	0.3775	0.2500	1.0000	0.0200	0.1000	0.4332
1.00E+06	23.75	20	0.3000	0.0500	0.1225	1.5410	1.0000	0.1000	1.0000	0.5126